Addressing the challenges of silicon waveguides with subwavelength nanostructures

Przemek John Bock
B. Eng. (Carleton), M. Eng. (McGill)

June 20, 2011

Thesis submitted to the
Faculty of Graduate and Postdoctoral Studies
In partial fulfillment of the requirements
For the PhD degree in Electrical Engineering

Faculty of Engineering
School of Information Technology and Engineering
University of Ottawa

To mom and dad, you guys are awesome parents!

Acknowledgements

I would first like to thank Dr. Pavel Cheben, my mentor and friend. His guidance has shaped me into the person that I am today. Aside from the writing, technical, composition, drafting, engineering skills etc. I have learned from him, he showed me how I can make a livelihood for myself in science. Thank you. The ideas for this thesis were a collaboration with Dr. Pavel Cheben, who originally proposed the concept of SWG waveguides for the silicon-on-insulator material platform.

I would like to thank Prof. Trevor J. Hall for providing me the freedom to pursue my own research interests, for financially supporting me for 4 years, and for his insight into how I should organize and present my thesis work. I would like to thank the whole Optoelectronics Group at NRC - IMS. In particular, Dr. Siegfried Janz for helpful discussions, insight into my papers, encouragement and for allowing me to participate in this world class research group. The concept of the sidewall grating spectrometer was originally proposed by Dr. Siegfried Janz and Dr. Pavel Cheben (NRC notes 2004). Dr. André Delâge for teaching me so much, for many helpful discussions and insight into optics. Dr. André Delâge originally derived the diffraction integral to model the sidewall spectrometer (NRC notes 2006) and helped with the French version of the abstract. Dr. Jens H. Schmid and Dr. Jean Lapointe for fabricating the devices and taking the SEM images. Dr. Goef Aers who created the interface for the MIT Photonic Band Solver and Dr. Jens Schmid, who kindly used it to generate the data for figure 2.3. I would also like to thank Dr. Jacques Albert and Dr. Henry Schriemer who agreed to participate in my doctoral committee and my external examiners Dr. Maksim Skorobogatiy and Dr. Karin

Hinzer. The design, modeling, analysis, mask design and experimental characterization presented in this thesis were done by the author.

I would like to thank my family for their support, they are simply the best! In particular I would like to thank Heather for all her support and encouragement. She has been my partner, who stood by me throughout this whole process. Thanks!

Abstract

Planar waveguide devices have been made progressively smaller, resulting in higher integration density, more functions on a single chip, greater yields and lower cost. In particular, the high refractive index contrast ($\Delta n \sim 2$) of the silicon-on-insulator (SOI) material platform permits waveguide bend radii as small as a few micrometers, thereby markedly reducing device size. However, high field intensity at the waveguide core-cladding boundary increases scattering loss from fabrication imperfections on the waveguide sidewall. For dispersive devices based on array waveguide gratings, this high field intensity at the waveguide core-cladding boundary results in phase error accumulation in the waveguide array ultimately limiting crosstalk performance. As devices become more complex, waveguide crossings are increasingly important to facilitate connectivity and minimize device footprint. However, due to the large numerical aperture of SOI waveguides the insertion loss and crosstalk to the intersecting waveguide is large. The high-refractive index contrast also results in inefficient coupling between waveguides of different geometries, which is a problem for array waveguide gratings and echelle gratings.

The goal of this thesis is to address these challenges by using periodic dielectric nanostructures at a subwavelength scale to create an effective homogeneous medium. This solution is innovative because it is based on geometric properties requiring no added fabrication complexity, process refinement or new materials. In fact, the new materials created are composite nanostructures made by interlacing silicon segments with SU-8 polymer at varying pitch, width and duty cycle on a silica substrate. What has been achieved is the first experimental demonstration that these subwavelength gratings are

efficient waveguides, can cross each other with minimal loss and crosstalk can facilitate mode coupling between different waveguide geometries. Experimental demonstration of a new dispersive device based on blazed waveguide sidewall gratings indicates superior performance to array waveguide gratings and echelle gratings (on SOI), and is only possible by utilizing subwavelength gratings as efficient mode transformers. This work is relevant because of the interest in leveraging the vast silicon microelectronics fabrication infrastructure. Here, subwavelength gratings provide a means to implement different refractive index materials without changing the microelectronics fabrication process.

Résumé

La possibilité de fabriquer des dispositifs à guides d'ondes de plus en plus petits a résulté en une plus grande densité d'intégration, une augmentation du nombre de fonctions par puce et un meilleur rendement tout en réduisant les coûts. En particulier, le saut d'indice élevé ($\Delta n \approx 2$) du matériau silicium-sur-isolant (SOI) permet de réaliser des guides d'ondes courbes ayant des rayons courbures aussi petits que quelques micromètres, réduisant de façon remarquable la taille des dispositifs. Cependant la grande intensité du champ électrique à la frontière cœur-gaine augmente considérablement l'atténuation due aux imperfections des parois du guide d'ondes. Dans le cas des éléments dispersifs basés sur des réseaux de guides d'ondes phasés (AWG), cette interaction du champ avec l'interface résulte en une accumulation d'erreurs de phase dans le réseau de guides qui en dégrade les performances en augmentant la diaphonie. À mesure que les dispositifs augmentent en complexité, le croisement des guides devient une solution de plus en plus importante pour simplifier la connectivité et minimiser la taille des dispositifs. Cependant, en raison de la grande ouverture numérique des guides en SOI, la perte d'insertion et le couplage avec le guide d'ondes de l'intersection sont grands. Le grand saut d'indice a aussi pour conséquence un couplage inefficace entre les guides de différentes géométries, ce qui constitue un problème sérieux pour les réseaux de guides d'ondes phasés et les réseaux échelles.

Le but de cette thèse est de relever ces défis en employant des nanostructures périodiques de diélectriques en régime sub-longueur d'onde pour créer un milieu homogène effectif. Cette solution est novatrice parce qu'elle est basée uniquement sur des propriétés géométriques qui ne requièrent aucune complexité supplémentaire de

fabrication, ni raffinement de procédés, ni de nouveaux matériaux. En fait, les nouveaux matériaux ainsi formés sont des nanostructures composites fabriquées en alternant, sur un substrat de verre, des segments de silicium et de polymère SU-8 de pas, d'épaisseur et de cycle utile variables. Nous avons établi, pour la première fois, la preuve expérimentale que ces réseaux sub-longueur d'ondes sont des guides d'ondes efficaces, qu'ils peuvent s'entrecroiser avec un minimum de pertes et d'interférence et qu'ils peuvent faciliter le couplage de modes entre des guides d'ondes de géométries différentes. La démonstration expérimentale d'un nouvel élément dispersif constitué d'un réseau blazé sur la paroi d'un guide d'ondes indique des performances supérieures à celles des réseaux de guides d'ondes phasés et des réseaux échelles sur SOI; ce nouveau dispositif n'est réalisable qu'en utilisant un réseau sub-longueur d'ondes comme transformateur de modes efficace. Ce travail est important puisqu'il permet d'utiliser la vaste infrastructure de fabrication microélectronique au profit de composants optiques. De plus, les réseaux sub-longueur d'ondes permettent de réaliser des matériaux de différents indices de réfraction sans changer le processus de fabrication de la microélectronique.

Table of Contents

List of Figures

1. Introduction

1.1 Motivation

High refractive index contrast planar waveguides are of interest because the tight confinement of the mode results in a minimum bend radius of only a few microns, permitting higher integration density, more functions on a single chip, greater yields and ultimately lower cost. Interferometric devices are scaled down by a factor of $1/n$ since the wavelength in the medium scales by wavelength/n. Spatial dispersion devices like array waveguide gratings gain resolution because achievable mode and spot size are proportional to wavelength. Waveguide sensors benefit from high refractive index contrast as the light intensity at the core-cladding boundary is high. Of particular interest is the silicon-on-insulator (SOI) material platform due to the compatibility with the microelectronic fabrication infrastructure. Silicon-on-insulator waveguides used in this thesis have a silicon core (n_{Si} = 3.476 at λ = 1550 nm) on a silica substrate (n_{SiO2} = 1.444 at λ = 1550 nm), with SU-8 polymer ($n_{SU\text{-}8}$ = 1.577 at λ = 1550 nm) as cladding, resulting in a refractive index contrast of $\Delta n \sim 2$.

Limitations of this material platform include efficient scattering at the core-cladding boundary imperfections, refractive indices restricted to silica and silicon and the effective index of a waveguide determined by width alone (since the Si wafer thickness is fixed).

Subwavelength gratings (SWGs) can address all of these limitations by engineering an effective medium (see Appendix B for a detailed description of the effective medium principle) by varying the pitch, width and duty cycle of periodic Si segments. In such a waveguide, the mode is delocalized reducing the scattering efficiency at the core-cladding boundary imperfections. The subwavelength waveguide solution has a number of advantages over delocalizing the waveguide mode in a conventional waveguide by simply reducing its width. To achieve an equivalent delocalization of a subwavelength grating waveguide, a conventional waveguide requires a considerably narrower width. For example, the mode of a subwavelength grating waveguide with 300 nm wide segments is approximately equivalent to a 150 nm wide conventional waveguide (Chapter 2). Such a narrow conventional waveguide is near the fundamental mode cut-off condition; consequently, a small fabrication bias of 50 nm would result in the waveguide no longer supporting a guided mode. A subwavelength grating waveguide fabricated with such a bias would still support a mode because its dimensions are away from cut-off condition demonstrating that a subwavelength grating solution to mode delocalization is more tolerant to fabrication imperfections. A long narrow conventional waveguide is also highly susceptible to discontinuities in the fabrication process and is the main reason why long narrow conventional waveguides are avoided. Narrow conventional waveguides are also very polarization sensitive, whereas a subwavelength grating delocalization can be accomplished by not only varying the width (as in a conventional waveguide), but the pitch and duty cycle allowing for the tailoring of the polarization dependence.

As previously indicated, a key advantage of the silicon-on-insulator material platform is the high index contrast allowing for very compact devices. Delocalizing the mode has the opposite effect as the minimum bend radius of the waveguide is increased; therefore, increasing device footprint. How then do subwavelength gratings, as a refractive index engineering technique, facilitate compact devices? Subwavelength gratings as waveguides can be used to implement straight unbalanced Mach-Zehnder interferometers (MZIs), which can be stacked into compact arrays. Such waveguides are demonstrated in Chapter 2. As waveguide crossings, subwavelength gratings provide interconnection to minimize device footprint as demonstrated in Chapter 3. Subwavelength gratings can be used as effective mode transformers, also shown in Chapter 3. As another example, in Chapter 4 such a subwavelength grating mode transformer at the slab-array boundary creates a smooth refractive index transition without increasing device size. In Chapter 5, a very compact wavelength demultiplexer is presented. Such a small device would be difficult to fabricate without subwavelength gratings, which provide both an anti-reflection boundary and mode confinement.

Subwavelength gratings not only address the challenges of the silicon-on-insulator material platform, but open up new opportunities for innovation. Such periodic waveguides can have tailored dispersion, thermal and nonlinear properties. Subwavelength gratings can also be used as anti-reflection or high-reflection structures, by simply changing their geometry. All of these benefits complement the silicon-on-insulator material platform by providing efficient solutions to the problems discussed in this thesis.

1.2 History

Light can be confined in a dielectric waveguide by index-guiding or by exciting defect states in a periodic lattice. A conventional planar waveguide confines the light in a core, which has a higher refractive index than the surrounding cladding material. However, the high refractive index contrast of silicon waveguides results in efficient scattering at the core-cladding boundary imperfections [1]. High refractive index contrast ridge waveguides minimize this effect with a larger core size at the expense of minimum bend radii of several hundred micrometers [2]. For channel waveguides, scattering efficiency can be reduced by using waveguides with a core area that is small enough to delocalize the waveguide mode, such that the field intensity at the core-cladding boundary is diminished [3] or by making use of an inherent interference effect of the scattered radiation [4,5]. Large dependence of propagation loss on waveguide geometry [6], wavelength and polarization [7] has been reported for silicon wire waveguides. Such dramatic changes of loss in silicon wire waveguides are a significant obstacle in building practical microphotonic circuits. Low loss of -1 dB/cm [8] to -1.7 dB/cm [9] has been achieved for transverse electric (TE) polarization. However, square core cross-sections are intentionally avoided to reduce the vertical sidewall height, resulting in optimal TE performance at typical waveguides dimensions of 500 nm × 200 nm. The penalty for this optimized waveguide TE performance is that a confined transverse magnetic (TM) mode may no longer be supported by the waveguide (depending on the cladding material used) [5]. Since sidewall imperfections originate from the etching process, propagation loss can be reduced by using an etchless process based on selective oxidation [10], although such waveguides support only TE polarization and insertion loss is significant.

Periodic photonic lattices have also been investigated for waveguiding, but the efforts have almost exclusively focused on photonic crystals with $d \sim \lambda/2n_{\mathrm{eff}}$ that have a band gap at the operational frequency range. In such structures, a waveguide is created by introducing a line-defect in the periodic lattice that creates defect states localized within the lattice's photonic band gap. Propagation losses for line-defect waveguides in 2D periodic lattices range from -8.0 dB/cm [11] to -4.1 dB/cm [12]. However, such waveguides exhibit large wavelength and polarization dependent loss.

Extensive research into designing and fabricating complex waveguide devices for telecommunication applications [13-15] is now facilitating promising new applications in various areas, including sensing [16], spectroscopy [17,18] and interconnects [19-21]. Such devices benefit from the advantages of the silicon-on-insulator (SOI) material platform including compatibility with microelectronic fabrication and large scale integration. To fully exploit the potential of the SOI platform, these planar lightwave circuits (PLCs) require efficient waveguide crossings to facilitate connectivity and minimize device footprint.

Efficient waveguide crossings have been demonstrated in low index contrast glass waveguides ($\Delta n \sim 2\%$), for example by using the overlay between two multimode interference (MMIs) couplers [22]. Various waveguide crossings have also been proposed for high index contrast SOI waveguides. For example, photonic crystal waveguide crossings were originally proposed in [23], and have been optimized [24] and fabricated [25]. These structures exploit photonic crystal cavities to enhance coupling through the intersecting waveguide but suffer from high propagation loss and crosstalk. The resonant nature of these structures imposes stringent periodicity and small feature size requirements; consequently, the performance of these crossings is largely susceptible to fabrication imperfections. Waveguide crossovers have also been proposed and fabricated using the overlap of parabolic MMIs [26]. Here, the combination of a shallow etch crossing region with deep etch tapered waveguides minimizes both loss and crosstalk, at the expense of added fabrication complexity. Using the principle of a nonadiabatic taper

[27], a genetic algorithm was used to optimize a variable transverse width of a parabolic MMI, which can be fabricated with a single etch step [28]. Multiple waveguide crossings have also been theoretically investigated exploiting a narrow multimodal transverse field pattern with Bloch mode excitation from periodically spaced intersecting waveguides [29]. However challenges remain as previous designs [27-29] are optimized for only transverse electric (TE) polarization and transverse magnetic (TM) performance is poor.

Complex devices may require not only waveguide crossings, but may require a change in waveguide geometries. However, the coupling loss between waveguides of different geometries is increased due to greater mode mismatch for high-refractive index contrast waveguides. For example, polarization independence of array waveguide gratings (AWGs) and echelle gratings can be achieved using etched polarization compensation regions [30] resulting in a mode mismatch at the compensator interface. The mode mismatch loss can be reduced using a polarization compensator with a buried oxide layer [31], but this requires deposition of additional optical layers, thus adding to fabrication complexity. In another example, the main intrinsic source of loss in an AWG is coupling from the slab waveguide to the waveguide array. This loss is a consequence of different field distributions of the slab waveguide and the arrayed waveguides. As the continuous field in the slab waveguide propagates across the slab-array boundary, it couples to the discretized field of the array of waveguides. Here loss is particularly significant in high-refractive index contrast waveguides as the strong confinement results in increased reflection and mode mismatch. This effect can be reduced by optimizing the slab-array interface; for example, loss < 0.4 dB has been reported by employing a double-etch process [32]. Deep etched waveguides in the array are adiabatically tapered to shallow etched regions near the slab to create a gradual index transition; however, this implies increased fabrication complexity. Selective ultraviolet (UV) exposure can also be used to minimize the effective index mismatch between the slab waveguide and waveguide array, again at the cost of fabrication complexity [33]. Mode transformers have also been proposed to solve this problem for the low index contrast silica-on-silicon waveguide platform using a long period grating (LPG) [34]. Application of LPGs to a high contrast waveguide platform such as SOI is limited due to the prohibitive losses incurred at the interfaces between different LPG segments.

Presently, two types of planar waveguide (de)multiplexer technologies are used in wavelength division multiplexed communication, with emerging applications in interconnects and spectroscopy, namely array waveguide gratings and echelle gratings. Although remarkable progress has been achieved in arrayed waveguide gratings [13-15], this has been mostly in conventional glass waveguide technology. While performance is unrivalled in glass, these array waveguide gratings are several orders of magnitude larger than demultiplexers based on silicon nanophotonic waveguides. With advanced silicon components emerging including buffers [35], memory [36] and sources [37], small footprint demultiplexing technologies are a key component in the industrial realization of silicon photonics. Recently several very compact AWGs have been reported using silicon waveguides [38-45]. However using high refractive index contrast waveguides, the light intensity at the core-cladding boundary is large resulting in phase error accumulation (in the waveguide array) from fabrication induced sidewall roughness, ultimately limiting crosstalk performance.

Multiplexers based on planar waveguide echelle gratings avoid some of these problems, since the phase delays occur in the slab waveguide rather than in a waveguide array. Several demultiplexer devices based on waveguide echelle gratings have also recently been fabricated, both in glass (silica-on-silicon [46,47]) and in SOI waveguides [48-50]. The main challenges in fabricating echelle-grating demultiplexers are to fabricate smooth vertical grating facets, to control the polarization dependent wavelength shift, and to reduce the polarization dependent loss [13]. These issues have been successfully overcome in echelle grating devices based on glass waveguides [46,47], but are not completely resolved in the SOI based devices.

Little research has been done in developing new (de)multiplexer technologies due to the success of the glass based AWG. However, with the many advantages afforded to silicon photonics including low cost fabrication, compatibility with the CMOS infrastructure, high integration potential and high yield, there is a need for demultiplexers optimized for such a high refractive index contrast material platform. Cascaded ring resonator filters [51] or cascaded Mach-Zehnder interferometers [52] have been proposed; however, both require exact optical path lengths implying increased fabrication tolerance. An alternative is waveguide gratings, which were first implemented in straight waveguides with UV induced gratings as the dispersive element while tilting and chirping the grating provided the focusing element [53]. Using the curvature of the waveguide itself to focus the light was conceived in [54].

1.3 Aim

The challenges of the high refractive index contrast SOI waveguide platform can be addressed using subwavelength gratings:

Objective 1: To create efficient waveguides.

Objective 2: To create efficient waveguide crossings.

Objective 3: To create efficient waveguide mode transformers.

Objective 4: To create a (de)multiplexer design for high refractive index contrast waveguides.

Subwavelength periodic structures were first used in the late 19th century by Hertz, when studying the properties of the newly discovered radio waves with a fine grid of parallel metal wires used as a polarizer. It was not until the 1940s when electromagnetic wave propagation in a medium structured at the subwavelength scale was first studied, for alternate layers of a dielectric and a metal [55]. Although the subwavelength phenomenon has been known and exploited for many years in free-space optics [56,57] and recently also in plasmonics [58-61], little has been reported on using subwavelength structures in dielectric optical waveguides [62,63,64].

Several other types of segmented waveguides have been previously studied numerically [65,66] and also experimentally [67,68]. The latter have been proposed as long-period-grating tapers with a segmentation pitch of $\Lambda \gg \lambda/(2n_{\mathrm{eff}})$ for mode size transformation in low-index-contrast waveguides such as those made in a silica-on-silicon material platform, however their application in high-index-contrast waveguides is hindered by the reflection and the diffraction losses incurred at the boundaries of the different segments. As these long-period segmented waveguides do not support a (theoretically) lossless mode, the light coupling to radiation modes limits applications of such structures to short propagation lengths and small index discontinuities. Subwavelength gratings are unique in that the grating supports a true lossless mode.

Originally implemented in planar dielectric waveguides as mirrors [69], subwavelength gratings have seen applications as efficient fibre-chip couplers [70], off-plane fibre couplers [71,72], antireflective gradient index structures and interference mirrors [73,74]. Subwavelength gratings were originally proposed as silicon waveguides in [70] and later as a composite waveguide cladding in [75]. Subwavelength gratings can create artificial media engineered using microscopic inhomogeneities to enact effective macroscopic behaviour (Appendix B). For the silicon-on-insulator (SOI) material platform, a subwavelength grating can be created by the combination of single crystal silicon and silica (SiO_2) or other low index materials such as SU-8 polymer. These periodic structures frustrate diffraction provided they operate outside the Bragg condition and behave like a homogeneous medium [76,77], where the light excites the Bloch mode of the grating resulting in efficient propagation of the electromagnetic field.

By modifying the pitch, width and duty cycle of the subwavelength segments, the effective index of the medium can be engineered locally. This technique provides a means to tailor the effective index, mode profile and dispersion of the subwavelength grating waveguide, without additional fabrication steps. In this thesis, silicon segments with SU-8 cladding material were used; however any materials can be interlaced for specific applications. For example, athermal waveguides can be designed by interlacing materials with opposite polarity thermo-optic coefficients [78], while waveguide modulators may be implemented by interlacing waveguide core segments with a nonlinear electro-optic material. Such freedom in waveguide design suggests that subwavelength grating waveguides can be used in a broad range of applications.

1.4 Thesis structure

Organization is based on a addressing each of the four thesis objectives. Chapter 2 discusses subwavelength grating waveguides, where group index, propagation loss, polarization dependent loss (PDL) and wavelength dependence are experimentally measured. Chapter 3 builds on this foundation by numerical modeling and experimental demonstration of efficient waveguide crossings and wire waveguide to SWG waveguide mode converters. Chapter 4 develops this work further by presenting the numerical simulation of several SWG mode converters for waveguides of different geometries. Chapter 5 presents a new planar waveguide demultiplexer design as an alternative to AWGs and echelle gratings. Interestingly, this device would not be possible without the subwavelength grating mode converters demonstrated in Chapter 4. Finally, Chapter 6 presents the experimental demonstration of the sidewall grating spectrometer design in Chapter 5, with implemented subwavelength grating structures from Chapter 4.

1.5 Summary of achievements

Objective 1: To create efficient waveguides.

Design and experimental demonstration of a new waveguide principle is achieved using subwavelength gratings. Unlike other periodic waveguides such as line-defects in a 2D photonic crystal lattice, a subwavelength grating waveguide confines the light like a conventional index-guided structure and does not exhibit optically resonant behaviour. Subwavelength grating waveguides in silicon-on-insulator were fabricated with a single etch step and allowed for flexible control of the effective refractive index of the waveguide core simply by lithographic patterning. Experimental measurements indicate a low propagation loss of -2.6 dB/cm for subwavelength grating waveguides with a cross section of 250×260 nm^2 with negligible polarization and wavelength dependent loss, which compares favourably to conventional microphotonic silicon waveguides (-3.1 dB/cm for TE and -3.2 dB/cm for TM polarizations for a 400×260 nm^2 wire waveguide in section 3.4). The measured group index is nearly constant $n_g \sim 1.5$ over a wavelength range exceeding the telecom C-band.

Objective 2: To create efficient waveguide crossings.

Design and experimental demonstration of a new type of waveguide crossing is achieved based on subwavelength gratings in silicon waveguides. Three dimensional finite-difference time-domain simulations were used to minimize loss, crosstalk and polarization dependence. Measurement of fabricated devices showed the waveguide crossings have a loss as low as -0.023 dB/crossing, polarization dependent loss of < 0.02 dB and crosstalk <-40 dB.

Objective 3: To create efficient waveguide mode transformers.

Several new types of SWG GRID structures for efficient mode coupling in high index contrast slab waveguides are presented. Using a SWG, an adiabatic transition is achieved at the interface between silicon-on-insulator waveguides of different geometries.

The SWG transition region minimized both fundamental mode mismatch loss and coupling to higher order modes. By creating the gradient effective index region in the direction of propagation, efficient vertical mode transformation can be attained between slab waveguides of different core thickness. Using 3D finite-difference time-domain simulations loss, polarization dependence and higher order mode excitation were studied for two types (triangular and triangular-transverse) of SWG structures. Theoretical demonstration of two solutions to reduce the polarization dependent loss of these structures was presented. Finally, SWG structures were implemented to reduce loss and higher order mode excitation between the slab waveguide and the array waveguide of an AWG. Compared to a conventional AWG, the loss was reduced from −1.4 dB to < −0.2 dB at the slab-array interface. The structures which were proposed can be fabricated by a single etch step.

Objective 4: To create a (de)multiplexer design for high refractive index contrast waveguides.

Design and experimental demonstration of an original diffraction grating demultiplexer device is achieved with a very small footprint, for the silicon-on-insulator waveguide platform. The wavelength dispersive properties are provided by a second-order diffraction grating designed to be lithographically defined and etched in the sidewall of a curved Si waveguide. The grating is blazed to maximize the -1st order diffraction efficiency. This device wound be impossible without SWGs, as the diffracted light is coupled into the silicon slab waveguide via an impedance matching SWG GRIN antireflective interface as discussed in **Objective 3**. The waveguide is curved in order to focus the light onto the Rowland [79] circle, where different wavelengths are intercepted by different receiver waveguides. The phase errors were substantially reduced using an apodized design with a chirped grating, which assured a constant effective index along the grating length.

Experimental demonstration of this demultiplexer device is achieved having the widest operational wavelength range yet reported of 300 nm and a crosstalk of nearly -20 dB, superior to similar devices. The footprint of the demultiplexer is only 100 × 160 μm^2, making it the smallest in the world compared to devices of similar performance.

Journal publications resulting from this thesis

1) **P. J. Bock**, P. Cheben, J. H. Schmid, J. Lapointe, A. Delâge, S. Janz, G. Aers, D.-X. Xu, A. Densmore and T. J. Hall, "Subwavelength grating periodic structures in silicon-on-insulator: A new type of microphotonic waveguide," Opt. Express 18, pp. 20251-20262 (2010). **[Chapter 2]**
2) **P. J. Bock**, P. Cheben, J. H. Schmid, J. Lapointe, A. Delâge, D.-X. Xu, S. Janz, A. Densmore and T. J. Hall, "Subwavelength grating crossings for silicon wire waveguides," Opt. Express 18, 15, pp. 16146-16155 (2010). **[Chapter 3]**
3) **P. J. Bock**, P. Cheben, J. H. Schmid, A. Delâge, D.-X. Xu, S. Janz and T. J. Hall "Sub-wavelength grating mode transformers in silicon slab waveguides," Opt. Express 17, 20, pp. 18947-18960 (2009). **[Chapter 4]**
4) **P. J. Bock**, P. Cheben, A. Delâge, J. H. Schmid, D.-X. Xu, S. Janz and T. J. Hall, "Demultiplexer with blazed waveguide sidewall grating and subwavelength grating structure," Opt. Express 16, 22, pp. 17616-17625 (2008). **[Chapter 5]**
5) **P. J. Bock**, P. Cheben, D.-X. Xu, S. Janz and T. J. Hall, "Mirror cavity MMI coupled photonic wire resonator in SOI," Opt. Express 15, 21, pp. 13907-13912 (2007). **[Appendix E]**

2. Subwavelength Grating Waveguides

2.1 Subwavelength grating principle and simulation

Subwavelength gratings can create artificial media engineered using microscopic inhomogeneities to enact effective macroscopic behaviour. For the silicon-on-insulator (SOI) material platform, a subwavelength grating can be created by the combination of single crystal silicon and amorphous silica (or other low index materials such as SU-8 polymer). These periodic structures frustrate diffraction provided they operate outside the Bragg condition and behave like a homogeneous medium [76,77] as described in more detail in Appendix B. In a subwavelength grating waveguide with a core consisting of a periodic arrangement of silicon and silica segments, light excites a Bloch mode, which can theoretically propagate through the segmented waveguide without any losses caused by diffraction into radiative or cladding modes. A detailed description for the Bloch mode is presented in Appendix A. A schematic of a subwavelength gratings (SWG) waveguide is shown in Fig. 2.1(a), including an equivalent wire waveguide with an engineered core refractive index (Fig. 2.1(b)).

This chapter demonstrates a solution to **Objective 2: Efficient waveguides** for high index contrast waveguides. The solution is based on SWG and is innovative because it requires no added fabrication complexity, process refinement or new materials. In fact, new materials are created as composite nanostructures made by interlacing silicon segments with SU-8 polymer at varying pitch, width and duty cycle on a silica substrate.

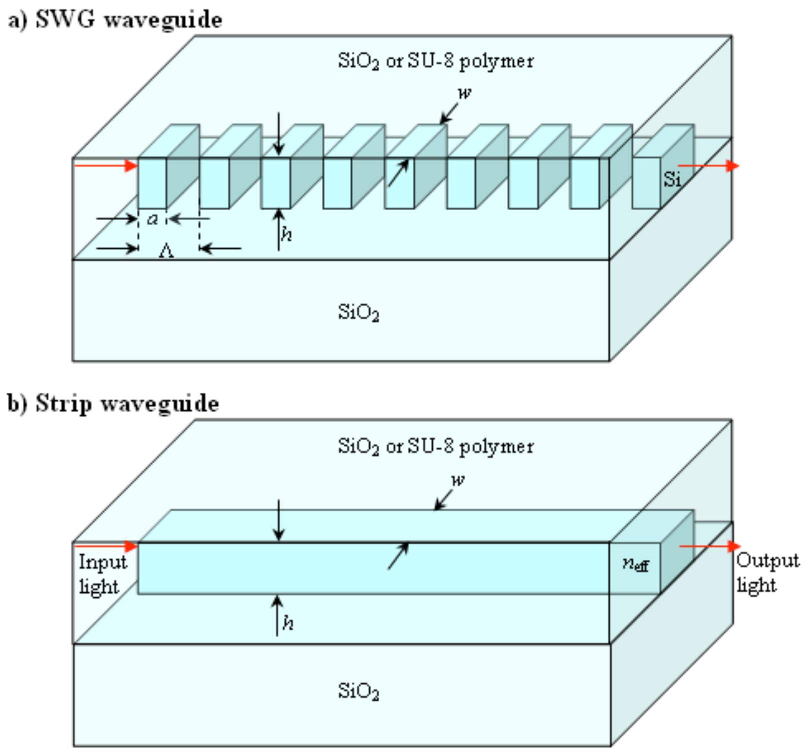

Fig. 2.1. Schematic of a) an SWG waveguide and b) an equivalent strip waveguide. An effective material refractive index n_{eff} of the equivalent wire waveguide is determined by spatial averaging of refractive indexes of the waveguide core (Si) and the cladding (e.g., SiO_2, SU-8, air, etc.) materials at a subwavelength scale. The resulting effective index can be controlled by lithography (changing grating duty ratio a/Λ, width w, etc.).

In the nominal SWG waveguide, the grating period, duty cycle and segment dimensions are chosen to avoid the formation of standing waves due to Bragg scattering and the opening of a band gap near λ = 1550 nm wavelength. According to this criteria and using finite-difference time-domain and MIT photonic bands (frequency domain) calculations, the following structural parameters were chosen: grating pitch Λ = 300 nm, segment width w = 300 nm and segment length a = 150 nm. Note that the grating pitch is less than a half of the effective wavelength of the waveguide mode $\lambda_{eff} = \lambda/2n_{eff}$. For these parameters, the mode delocalization from the core yields a reduced field intensity at the core-cladding boundary, thereby reducing scattering loss by the sidewall imperfections.

Like a conventional waveguide mode, a guided periodic mode is lossless. The loss mechanism arises from the fabrication imperfections, resulting in the segments not being perfectly periodic, as well as introducing new periodicities of the roughness itself. From conventional waveguide loss theory, in order to minimize loss one must reduce the scattering efficiency of the imperfections by reducing the field intensity at the rough boundary. Therefore, the SWG width and duty cycle were chosen to maximize delocalization (minimize loss) and yet minimize light leakage to the substrate (buried oxide thickness was 2 μm), which created an upper limit to the degree of delocalization. The mode field diameter for the delocalized mode was 2.5 μm. The pitch of 300 nm and 400 nm was chosen to minimize the fusing of segments and keep the dimensions far away from a minimum feature size of 50 nm. The dispersion diagram of Fig. 2.3 shows that the periodic waveguide does indeed support a guided mode. From previous 2D FDTD studies on SWG couplers [70], only a 0.03 dB difference in coupling efficiency was calculated between 200 nm and 300 nm grating pitch. Subwavelength grating couplers having a 300 nm and a 400 nm grating pitch had the best experimental results; therefore it was logical to use those parameters for designing SWG waveguides. The best SWG couplers were a good indicator of grating parameters because the structure comprised of a 50 um coupler and a 150 um SWG waveguide with constant grating parameters. This was done to provide a dicing and polishing tolerance.

To study the full design space of a SWG, a model of the effect of roughness on a periodic mode would need to be created. This could not be done in FDTD due to the minimum mesh size of 10 nm for reasonable simulation durations. This was a proof of principle study, not an exhaustive optimization. Since these devices are new and never before tried an exhaustive study of the design space, without proof that these devices actually work, would be high risk. Instead, a proof of concept study was done based on the simulation tools available; and built on previous experimental results, to demonstrate experimentally that these structures guide light.

The mode delocalization is also evident in Fig. 2.2, showing an increased effective mode size for the SWG waveguide compared to a conventional wire waveguide of the same width. The chosen grating parameters minimize wavelength resonances due to diffraction effects, as it is evident in the calculated dispersion diagram (Fig. 2.3). Notice that the subwavelength grating waveguide at λ = 1550 nm is far outside the photonic bandgap region.

It is known that waveguide scattering loss is determined by the amplitude of the current source (the defect volume element interacting with the local electric field [80]) as well as the cumulative/interference effect of the spatial distribution of the scattering sources. A subwavelength grating waveguide effectively minimizes the source amplitude by delocalizing the mode, thereby decreasing electric field interaction with the volume defect. Furthermore, the gaps in-between the high-index segments shorten the interaction length. The reduction in interaction length is the result of half (assuming duty cycle of 50 %) the roughness experienced by the mode as half the sidewalls are gaps.

Three-dimensional (3D) finite-difference time-domain (FDTD) simulation (Appendix C contains a description of this numerical method) is used to estimate the mode profile of a SWG waveguide and how it compares to the mode profile of a wire waveguide. All simulations are done on a layout size of $x \times y \times z = 3 \times 3.26 \times 10\ \mu m^3$ having a mesh resolution of $\Delta x \times \Delta y \times \Delta z = 10 \times 10 \times 10\ nm^3$. Material refractive indices used are n_{Si} = 3.476 for the waveguide core, n_{SiO2} = 1.444 for the waveguide lower cladding (bottom oxide, BOX), and n_{SiO2} = 1.444 or n_{SU8} = 1.577 for the waveguide upper cladding, as either SiO_2 or SU-8 upper cladding is used in simulations. The silicon wafer thickness is 260 nm. The simulation time step is 1.67×10^{-17} s according to the Courant criterion $\Delta t \leq 1/(c(1/(\Delta x)^2 + 1/(\Delta y)^2 + 1/(\Delta z)^2)^{½})$, where c is the speed of light in vacuum. The simulated structure consists of a 10 μm long SWG straight waveguide with Λ = 300 nm, w = 300 nm and a = 150 nm. The mode of a continuous conventional waveguide (width 300 nm) is used to excite the SWG waveguide Bloch mode at λ = 1550 nm for TE polarization (E_x field component). The power was allowed to dissipate naturally as the light coupled from the conventional waveguide mode to the periodic Bloch mode. The mode profile of the SWG is recorded at the center x-y plane every 4th grating segment (0.9 μm spacing). To estimate the steady-state mode profile of the SWG waveguide (in the center of a grating segment), the overlap integral of each recorded mode profile is calculated with the mode profile 4 grating segments back. Steady-state behaviour is assumed when this mode overlap integral is constant and approaches unity.

Figure 2.2(a) shows the calculated mode overlap integral as a function of mode profile position (z-coordinate), and indicates > 99 % overlap at steady-state, for two different upper cladding materials, namely SiO_2 and SU-8. Using this SWG mode profile, the overlap integral with a wire waveguide of varying widths (160 nm – 300 nm) is calculated. Figure 2.2(b) indicates that the SWG mode profile (w = 300 nm, SiO_2 upper cladding) has only a 56 % overlap with an equivalent 300 nm wide wire waveguide.

However, this SWG waveguide mode profile has a ~90 % overlap with a 160 nm wide wire waveguide, indicating that the SWG mode is significantly delocalized. Mode profiles for a 300 nm wide wire waveguide and SWG waveguide are shown in Figs. 2.2(c) and 2.2(d) respectively, while the propagating field along the grating is shown in Fig. 2.2(e), for a SWG waveguide with SiO_2 upper cladding. Using the approximation of mode size from earlier work in long-period waveguide gratings [81], the refractive index contrast of a periodic waveguide Δn_{eff} is equivalent to an effective refractive index contrast of a uniform waveguide by $\Delta n_{\mathrm{eff}} \sim \eta \Delta n_{uniform}$, where η is the duty cycle (50 % in the nominal design). Assuming silicon segments and silica upper cladding, $\Delta n_{\mathrm{eff}} = \eta \Delta n_{uniform} = 0.5(3.476 - 1.444) \sim 1$ resulting in a 300 nm wide waveguide with $n_{\mathrm{clad}} = 1.444$ and $n_{\mathrm{core}} = 2.46$ (for SU-8 upper cladding, $n_{\mathrm{clad}} = 1.577$, $n_{\mathrm{core}} = 2.52$).

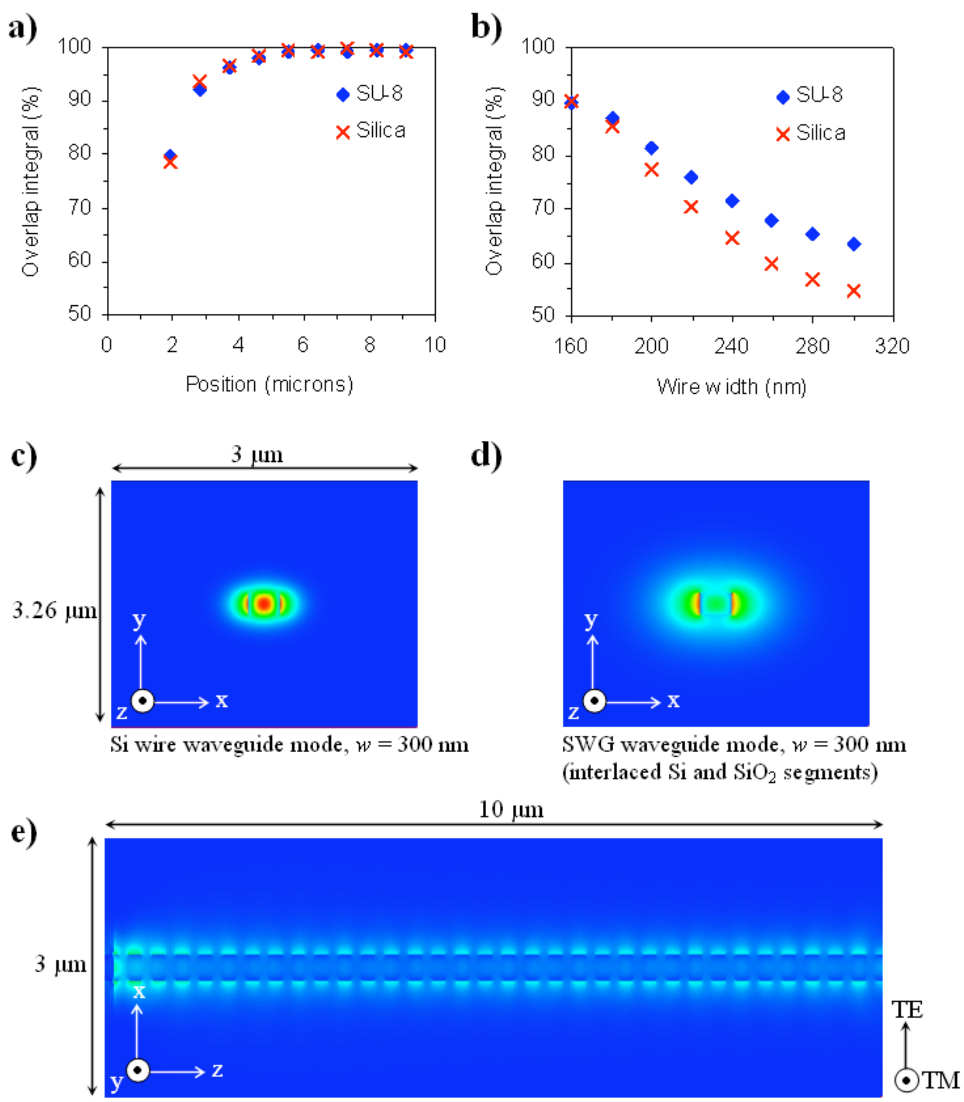

Fig. 2.2. a) Calculated mode overlap integral as a function of mode profile position (z-coordinate). b) Overlap integral of the steady-state SWG mode profile with a wire waveguide of varying widths (160 nm – 300 nm). c) Mode profile of a wire waveguide (w = 300 nm, SiO_2 upper cladding). d) Mode profile of a SWG waveguide (w = 300 nm, SiO_2 upper cladding) at the center x-y plane of a segment. e) Propagating field along the subwavelength grating, excited by the wire waveguide mode at λ = 1550 nm for TE polarization (E_x field component).

For both cases, such an effective uniform waveguide has a 96 % overlap with the steady-state SWG mode profile, indicating good agreement with this approximation. The results are nearly identical for SiO_2 and SU-8 upper cladding materials. These results also suggest that because the mode is delocalized from the core, the scattering loss due to sidewall fabrication imperfections can be reduced using the SWG waveguide.

The SWG waveguide mode is also calculated using the MIT photonic bands (MPB) frequency-domain software [82], yielding good agreement with the FDTD simulations above. Furthermore, the group index of the nominal SWG waveguide (SU-8 upper cladding) is calculated using MPB with a layout size of $x \times y \times z = 2 \times 2 \times 0.3\ \mu m^3$ having a mesh resolution of $\Delta x \times \Delta y \times \Delta z = 20 \times 20 \times 20\ nm^3$. The SU-8 upper cladding is chosen as it is the material used to fabricate the structures (section 2.3). In Fig. 2.3 the dispersion relation for the TE and TM modes of the SWG waveguide is shown, which exhibits the expected behaviour for a periodic waveguide, namely a flattening of the dispersion with increasing wavenumber β as the Bragg condition is approached. Due to the subwavelength nature of the grating, the operating frequency is well below this flat dispersion region, as indicated in the Fig. 2.3. The group velocity of the propagating Bloch mode is given by the slope of the dispersion curve. The group index n_g of the TE and TM modes of the SWG waveguide is shown in the inset of Fig. 2.3 as a function of wavelength. The group index varies in the range 2.2 – 2.0 for the TE and 2.0 – 1.8 for the TM modes over the wavelength range of λ = 1480 nm – 1580 nm. The calculated group index is almost identical to the calculated effective index of the waveguide mode [99], confirming the absence of slow-light or resonant effects of the grating on the light propagation.

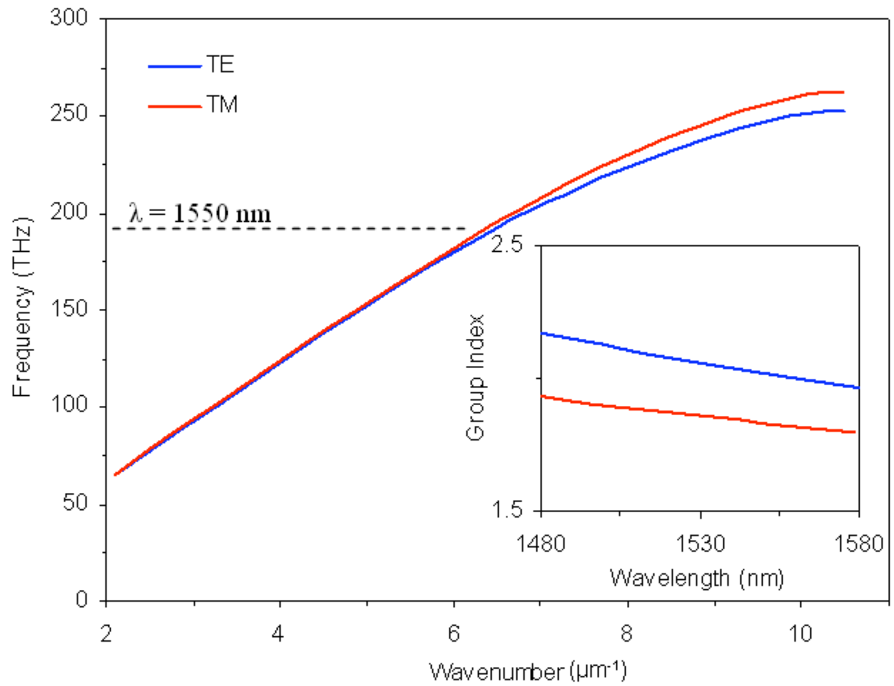

Fig. 2.3. a) Calculated dispersion diagram of a SWG waveguide consisting of 150 nm long Si segments separated by 150 nm long gaps filled with SU-8 polymer ($n_{SU\text{-}8}$ =1.577). Lower cladding is silicon dioxide (n_{SiO2} = 1.444) and upper cladding is SU-8. Inset shows the group index of the TE and TM modes for a wavelength range of λ = 1480 nm – 1580 nm.

2.2 Design and fabrication

Subwavelength grating straight waveguides are fabricated with a length of 0.61 cm (equal to the chip length) as shown in Fig. 2.4(a). To estimate propagation loss, test structures are also fabricated with SWG straight waveguide sections of 0.5 cm, 1.5 cm and 3.0 cm in length (Fig. 2.4(b)). In these test structures, silicon wire waveguides (450 × 260 nm^2) are coupled to SWG straight waveguides using the 50 μm long adiabatic transformer shown in Fig. 2.4(c) (further discussed in Section 3.4). The subsequent SWG section is 0.5 cm long with a constant pitch (Λ = 300 nm), width (w = 300 nm) and duty cycle

(50%). An identical adiabatic transformer section is used for the transition back to a wire waveguide. Wire waveguide U-bends of 20 μm radius are used in the test structure to fit multiple 0.5 cm long SWG straight waveguides on the chip, as indicated in Fig. 2.4(b), which shows an example of three 0.5 cm straight SWG sections. Test structures having varying SWG straight waveguide length all have identical wire lengths, number of bends, adiabatic transformers and fiber-chip couplers. Therefore the cumulative loss due to these elements is identical for each test structure, and will not affect the SWG loss measurement.

To estimate the group index of a SWG straight waveguide a Mach-Zehnder interferometer (MZI) is fabricated, where the reference arm is comprised of a wire waveguide (450×260 nm^2), while the signal arm is comprised of a 50 μm SWG taper followed by a SWG (Λ = 300 nm, w = 300 nm, duty cycle 50%) with length L = 1000 μm, and an identical SWG taper to transition back to wire waveguide (Fig. 2.4(c) and Fig. 2.5(d)). The MZI uses a 50:50 y-splitter implemented with two 150-μm-long and 25-μm-wide s-bends.

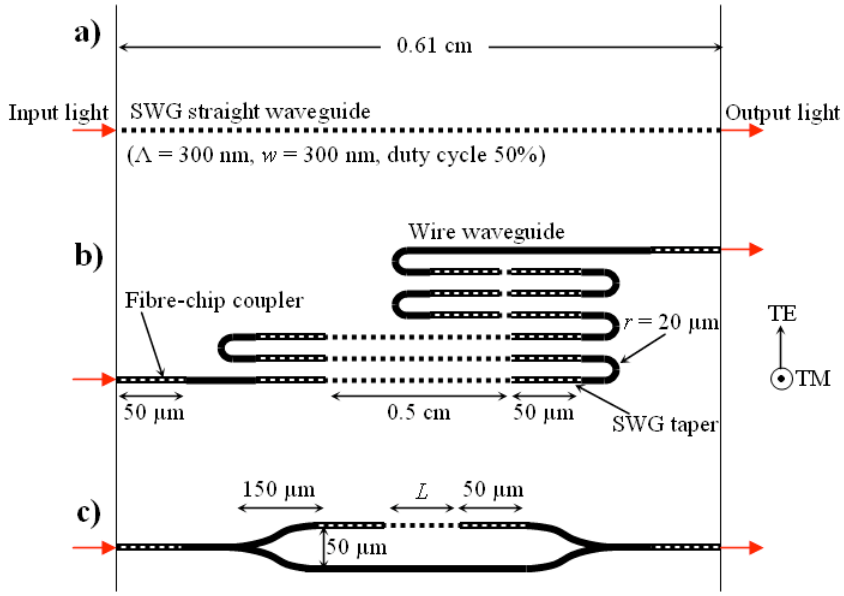

Fig. 2.4. a) Schematic of the test structure implemented for measuring the spectral response of a SWG straight waveguide with a length of 0.61 cm (equal to the chip length). b) Schematic of the test structure implemented for measuring propagation loss of a SWG straight waveguide. Wire waveguides (450×260 nm^2) are transformed to the SWG straight waveguide using a 50 µm long taper with bridging segments, followed by a 0.5 cm long SWG with a constant pitch (Λ = 300 nm), width (w = 300 nm) and duty cycle (50%). An identical taper is used for the transition back to a wire waveguide and a 180º wire waveguide bend (radius of 20 µm) is used in the test structure to fit multiple 0.5 cm long SWG straight waveguides on the chip. The specific schematic shown in (b) has three SWG sections with a total length of 1.5 cm. c) Schematic of the Mach-Zehnder interferometer (MZI) used to estimate the group index of a SWG straight waveguide. Mach-Zehnder interferometer reference arm is a wire waveguide (450×260 nm^2), while the signal arm is comprised of a 50 µm SWG taper followed by a SWG waveguide (Λ = 300 nm, w = 300 nm, duty cycle 50%, length L = 1000 µm) and a SWG taper to transition back to wire waveguide.

Structures were fabricated using commercially available SOI substrates with a 0.26 μm thick silicon layer and 2 μm thick buried oxide (BOX). Electron beam lithography was used to define the waveguide layout in high contrast hydrogen silsesquioxane resist, which formed SiO_2 upon electron beam exposure. Inductively coupled plasma reactive ion etching (ICP-RIE) was used to transfer the waveguide pattern onto the silicon layer. Samples were coated with a 2 μm thick polymer (SU-8, $n \sim 1.577$ at $\lambda = 1.55$ μm), then cleaved into separate chips and facets polished.

Figure 2.5 shows scanning electron microscope (SEM) images of fabricated structures including a SWG straight waveguide (Fig. 2.5(a)), detail of the grating segments (Fig. 2.5(b)), the first 15 μm of the 50 μm long SWG taper (Fig. 2.5(c)) and an optical microscope image of a MZI with SEM image detail of the signal arm (SWG straight waveguide) and reference arm (wire waveguide). From the SEM images it was determined that a fabrication bias of 50 nm was present. Therefore the actual dimensions of the SWG are $\Lambda = 300$ nm and $w = 250$ nm with a duty cycle of 33%. Actual wire waveguide width is 400 nm.

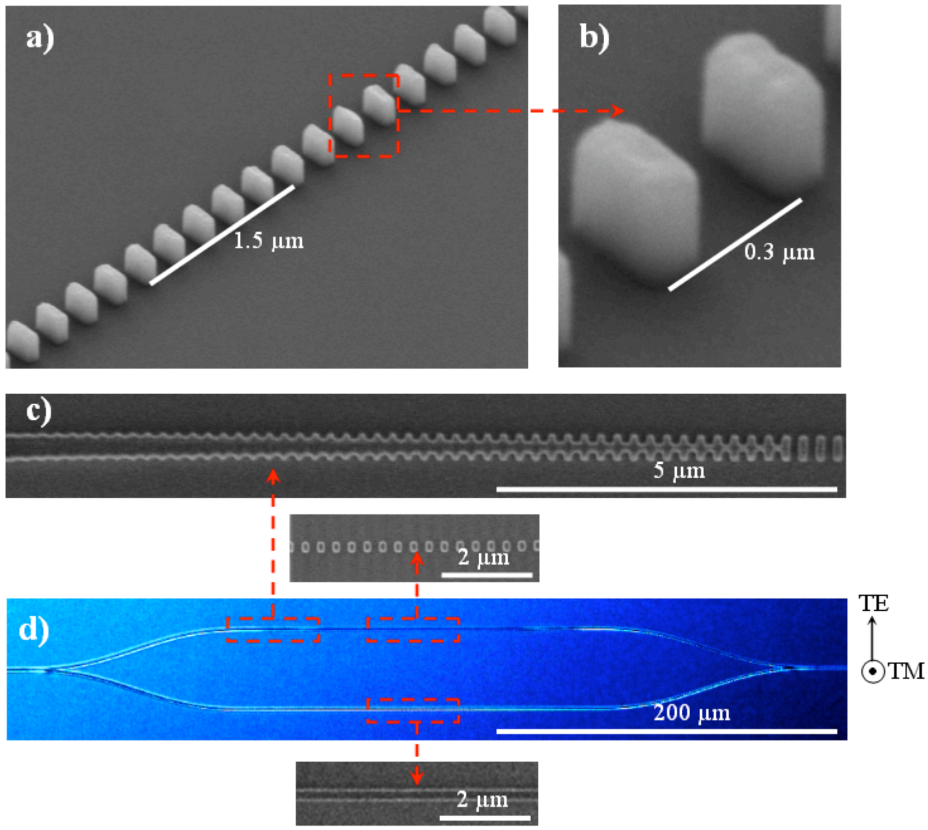

Fig. 2.5. Scanning electron microscope (SEM) images of fabricated structures including: a) SWG straight waveguide with Λ = 300 nm, w = 250 nm and a duty cycle of 33%. b) Detail of two SWG segments. c) The first 15 µm of the 50 µm long SWG taper. d) Optical microscope image of a MZI (L = 100 µm) with SEM image detail of the SWG arm and the reference arm (wire waveguide). Interferometric measurements (Fig. 2.7) were done with a MZI with a 1000 µm long SWG waveguide.

2.3 Experimental results

A tuneable external cavity semiconductor laser was used to measure the straight SWG waveguide (Fig. 2.4(a)) transmission spectra over a wavelength range λ = 1480 nm – 1580 nm. To measure the propagation loss, a broadband (3 dB bandwidth of λ = 1530 nm - 1560 nm) amplified spontaneous emission (ASE) source is used, to minimize Fabry-

Pérot cavity effects from the chip facets. To couple the light into the chip, a lensed fibre resulting in a Gaussian beam waist of ~2 μm (at the chip facet) is used with a SWG fibre-chip coupler [70]. Light is coupled out of the chip using another SWG coupler and subsequently focused by a microscope objective lens onto an InGaAs photodetector.

Figure 2.6(a) shows the insertion loss of a structure comprising of a 50 μm long, 150 nm wide (dimensions taken from SEM images) inverse taper fibre-to-chip coupler followed by a 5 mm conventional waveguide, followed by an identical inverse taper. Figure 2.6(b) shows the insertion loss of a structure comprising of a 50 μm long SWG fibre-to-chip coupler with bridging structures (Chapter 3, Fig. 3.3) having 300 nm wide segments followed by a 5 mm conventional waveguide, followed by an identical SWG coupler. The three measurements in Figs. 2.6(a) and 2.6(b) are three copies of the same structure. Using a SWG fibre-to-chip coupler, insertion loss is reduced by 3 dB for TE and 1 dB for TM polarizations at λ = 1550 nm. The key advantage of using SWG couplers over inverse tapers is the improved performance for both polarizations, while having a width twice that of the inverse taper (300 nm instead of 150 nm for the inverse taper). The improved performance is a result of the wider SWG coupler better matching the mode of the lensed fibre at the chip facet. Reducing the SWG segment width by 50 nm (from 300 nm to 250 nm) resulted in a negligible change in the insertion loss (0.3 dB improvement for TE and 0.4 dB reduction for TM polarizations). This demonstrates how SWGs are able to withstand a fabrication bias. Unlike a conventional waveguide, a SWG does not require very narrow widths (near minimum feature size tolerances) to delocalize the mode.

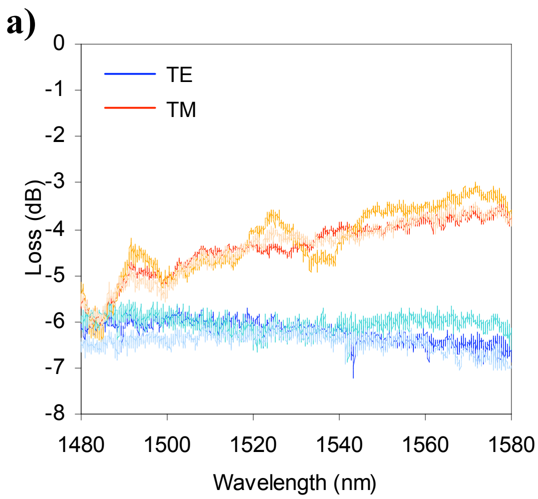

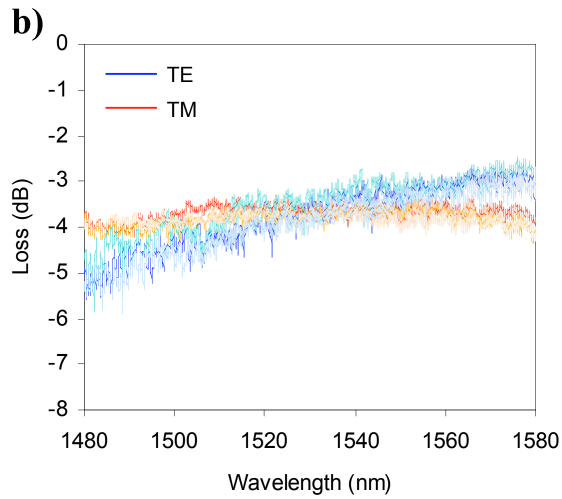

Fig. 2.6. Insertion loss for a 5 mm conventional waveguide for TE and TM polarizations for λ = 1480 nm – 1580 nm. a) 50 μm long, 150 nm wide inverse taper fibre-to-chip couplers. b) 50 μm long, SWG fibre-to-chip couplers having a segment width of 300 nm. The three measurements are three copies of the same structure.

Propagation loss for SWG waveguides is estimated by measuring the transmitted power through the loss test structures of Fig. 2.4(b), with multiple repeats of SWG straight waveguides of lengths 0.5 cm, 1.5 cm and 3.0 cm. Loss is determined from the slope of a linear fit of transmitted power vs. SWG waveguide length. The transmission spectrum of the SWG straight waveguide is normalized to these measurements. Figure 2.7(a) shows the measured wavelength dependent propagation loss, while Fig. 2.7(b) indicates the measured loss using the ASE source. For the best SWG waveguides, the propagation loss is 2.1 dB/cm for TE polarization, whereas typical SWG waveguide loss measured on different test structures is 2.6 dB/cm. The PDL is less than 0.5 dB for the wavelength range shown. It is remarkable that such low loss is achieved for light propagating over a 1 cm distance through more than 33,000 boundaries between high- and low-refractive-index segments having an index contrast of $\Delta n \sim 1.9$. While this finding is consistent with Bloch mode theory, it is also believed that this low loss is a direct consequence of the mode delocalization from the composite core with a corresponding decrease in light scattering at fabrication sidewalls imperfections, as found with the FDTD simulation mode profiles. In conventional waveguides, if the field intensity at the imperfection boundary is reduced so is scattering efficiency. Even though the FDTD simulation is done with an ideal waveguide (no roughness), is does not invalidate the fact that the field intensity is reduced at the core-cladding boundary. It is this boundary, the waveguide sidewall, which contains the fabrication imperfections.

To confirm the loss measurements obtained with the ASE source, the same measurements were repeated on the loss test structures using the tuneable external cavity semiconductor laser. The loss values obtained using the single wavelength source fluctuated randomly from one wavelength to another, due to Fabry-Pérot cavity effects arising from the different elements of the test structure (wires, bends, taper and couplers). However, the worst case propagation loss estimate in the C-band (λ = 1530 -1560 nm) of -3.0 dB/cm is consistent with the wavelength average value of -2.6 dB/cm obtained using the ASE source.

The efficiency of the adiabatic transformer is approximately 0.5 dB (Chaper 3, Section 3.4). Low overall transmission of loss test structures is the result of a rather complex layout (Fig. 2.4(b)), namely multiple wire-to-SWG mode transformers, Si wire waveguide segments, fibre-to-chip and chip-to-lens coupling interfaces, multiple U-bends, comparatively low input power level of the ASE source and the SWG waveguide loss itself. This layout was chosen to make certain that each test structure with different

SWG waveguide length is continued with an identical wire waveguide length and contains the same number of bends and SWG couplers, since changing those parameters for SWG waveguides of different lengths could be misinterpreted as SWG loss, as discussed in Section 2.2.

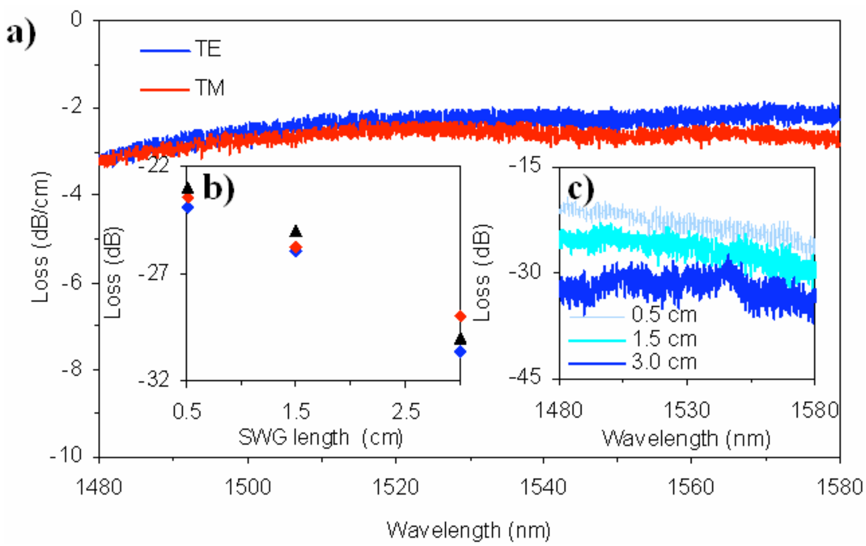

Fig. 2.7. a) Transmission spectra of a 0.61 cm long SWG straight waveguide measured for TE (blue) and TM (red) polarizations. b) Loss for meander test structures (Fig. 2.4(b)) with 0.5 cm, 1.5 cm and 3.0 cm long SWG waveguides, measured using an ASE broadband source. c) Transmission spectra for the same test structures as in (b), for TE polarization.

The group index of a SWG straight waveguide is measured interferometrically for a wavelength range of λ = 1480 nm – 1580 nm using a tuneable external cavity semiconductor laser. Group index is calculated using $n_g^{SWG} = \lambda_{min}\lambda_{max}/[2L(\lambda_{min} - \lambda_{max})] + n_g^{wire}$, [83] where λ_{min} and λ_{max} are the wavelengths at the minimum and maximum intensities of the interference fringes, L = 1000 μm is the length of the SWG straight waveguide and n_g^{wire} is the group index of the reference wire waveguide. Reference wire waveguide group index is estimated using a mode solver (Optiwave Corp.) to calculate the effective index of a 400 × 260 nm^2 waveguide with silicon core and SU-8 cladding on a silica substrate for λ = 1480 nm – 1580 nm. The group index was estimated using the derivative of a second order polynomial fit to the effective index wavelength dependence for TE (Fig. 2.8(a)) and TM (Fig. 2.8(b)) polarizations.

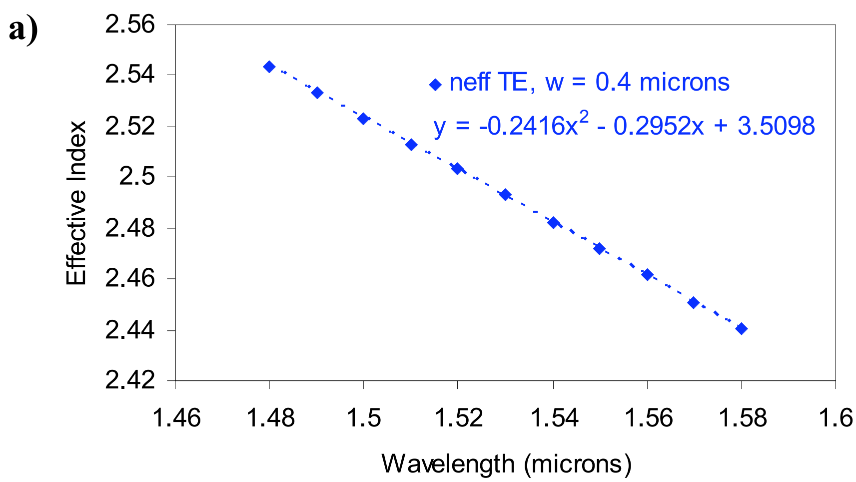

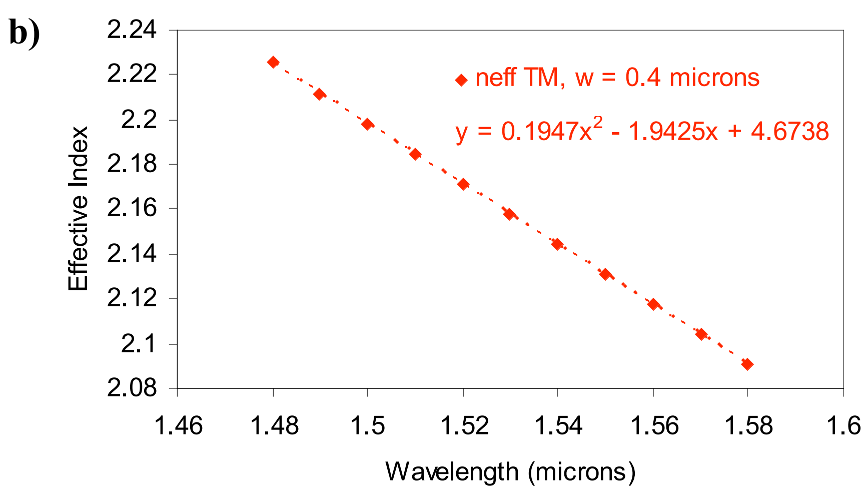

Fig. 2.8. Reference wire waveguide group index is estimated using a mode solver (Optiwave Corp.) to calculate the effective index of a 400 × 260 nm^2 waveguide with silicon core and SU-8 cladding on a silica substrate for λ = 1480 nm – 1580 nm.

The wire waveguide group index is found to be nearly constant across the wavelength range considered, with values of $n_g^{TE} \sim 4.1$ and $n_g^{TM} \sim 4.2$. Figure 2.9 shows the MZI spectral transmittance for λ = 1550 nm – 1560 nm for TE and TM polarizations. Based on these measurements the calculated group index of a SWG waveguide is presented in Fig. 2.10 and is compared to the theoretically calculated (MPB, [82]) group index for a periodic waveguide with the dimensions as measured by SEM. The agreement between experiment and theory is excellent, indicating a low and almost constant group index of $n_g \sim 1.5$ over the measured wavelength range. Nearly constant group index indicates that SWG waveguides are potentially useful for high bit-rate processing as well as nonlinear applications.

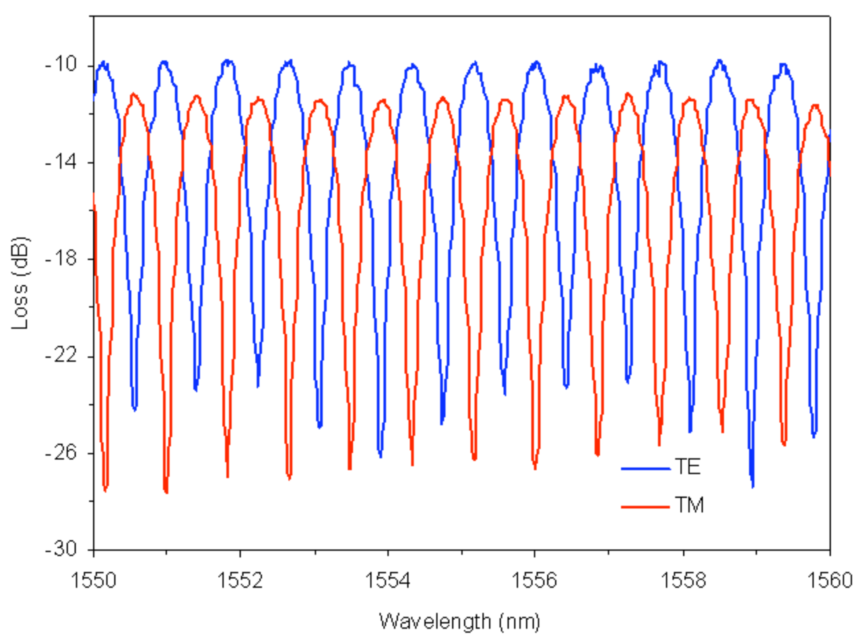

Fig. 2.9. MZI spectral transmittance. MZI with a Si wire waveguide reference arm and a 1000 μm long SWG waveguide signal arm, TE (blue) and TM (red) polarizations.

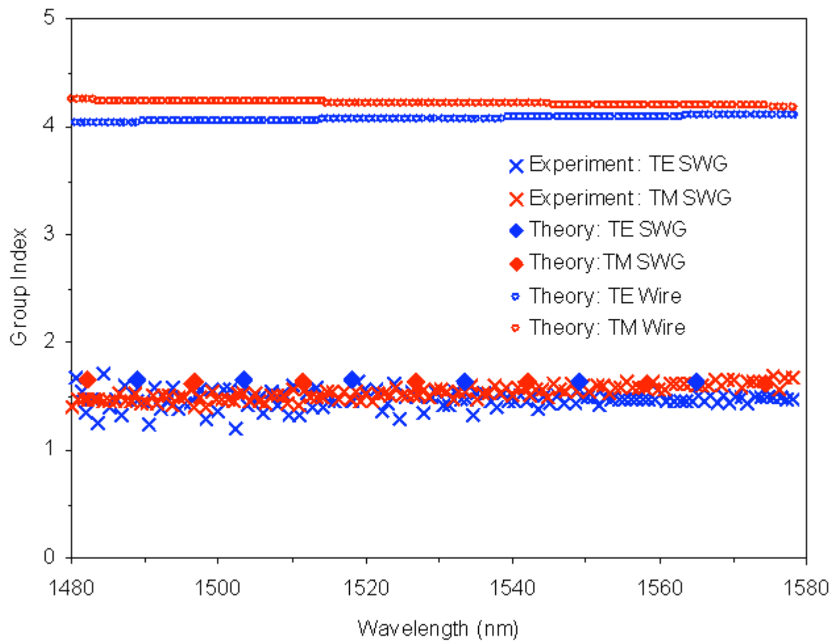

Fig. 2.10. The measured group index for a SWG waveguide. The group index of the reference wire waveguide for TE (blue circle) and TM (red circle) polarizations is estimated with a mode solver (Optiwave Corp.) by calculating the effective index of a 400 × 260 nm^2 waveguide with silicon core, SU-8 upper cladding and SiO_2 bottom cladding. The calculated group indexes for both the SWG waveguide and a photonic wire channel waveguide are shown for comparison.

2.4 Summary

Achieved is the first experimental demonstration of a subwavelength grating microphotonic waveguide to solve **Objective 1: Efficient waveguides**. Measured propagation loss for a subwavelength grating waveguide is remarkably low at -2.6 dB/cm, considering the light propagates through 33,000 segments with a refractive index contrast of $\Delta n \sim 2$. Polarization dependent loss is negligible (for the high index contrast silicon-on-insulator material platform) at 0.5 dB/cm, which compares favorably with other microphotonic waveguides. An FDTD analysis confirms that a SWG waveguide mode is delocalized compared to an equivalent wire waveguide width. If both polarizations are considered, the average loss for TE and TM of the SWG waveguide is one of the lowest yet reported for microphotonic waveguides. Measured group index of the SWG waveguide is in good agreement with the calculated values. An important advantage of SWG waveguides is that they allow for flexible control of the optical properties of the composite waveguide core, including its refractive index, mode size and dispersion by combining the constituent materials at a subwavelength scale, simply by lithographic patterning. Unlike conventional waveguides, SWG waveguides do not require very narrow widths to delocalize the mode. Even with a 50 nm fabrication bias, the SWG structures performed remarkable well. These results suggest that SWG waveguides can be important building blocks in future photonic devices. The next chapter demonstrates that these waveguides can cross each other with minimal loss and crosstalk.

3. Subwavelength Grating Crossings

3.1 Principle

Waveguide crossings are important to facilitate planar connectivity and minimize device footprint. A waveguide intersecting another waveguide creates a region with no lateral mode confinement. Light propagating through the waveguide intersection diffracts, which causes loss due to excitation of radiation modes and crosstalk by coupling to the guided modes of the intersecting waveguide. These losses are increased due to the large numerical aperture of an SOI wire waveguide. This chapter demonstrates a solution to **Objective 2: Efficient waveguide crossings** for high index contrast waveguides. The solution is based on subwavelength gratings (SWG) and is innovative because it requires no added fabrication complexity, process refinement or new materials. Experimental measurements from the previous chapter indicate SWG structures can be used as efficient waveguides, which is the foundation for this chapter.

The SWG design exploits the effective medium principle, which states that different optical materials, within subwavelength scales, can be combined approximately as an effective homogeneous material. Within this approximation, an effective medium can be characterized by an effective refractive index defined by a power series in the homogenization parameter $\chi = \Lambda/\lambda$, where Λ is the grating pitch and λ is the wavelength of light. Provided that the pitch Λ is less than the 1st order Bragg period $\Lambda_{Bragg} = \lambda/(2n_{eff})$, the grating is subwavelength and diffraction effects are frustrated. A more detailed description of effective medium principle is described in Appending B. For the SOI waveguide platform, the two natural choices for the high and low index materials to create the effective medium are silicon (waveguide core) and silica (cladding) respectively. A gradual change in the ratio of Si to SiO_2 along the light propagation direction (Fig. 3.1(a), z-axis) results in a corresponding effective refractive index change of the composite medium of the waveguide core.

The effective medium principle is used to design a SWG mode converter for efficient waveguide (Appendix B) crossings. This is done by gradually changing the effective index of the SWG waveguide through chirping the pitch and tapering the width of the grating segments (Fig. 3.1(a)). Reducing the segment width as the mode propagates along the crossing expands the mode near the crossover point. Since the SWG waveguide intersecting this expanded mode is also subwavelength, diffraction is frustrated resulting in minimal loss. At the same time coupling to the intersecting waveguide is reduced. An important practical advantage is that this crossover structure can be fabricated in a single etch step.

3.2 Subwavelength crossing simulation

3D FDTD simulation with a mesh size of $\Delta x \times \Delta y \times \Delta z = 10 \times 20 \times 10$ nm^3 is used to ensure finer resolution for the taper (x-coordinate, Fig. 3.1(a)) and chirp (z-coordinate, Fig. 3.1(a)). This increased numerical accuracy is at the expense of layout size, which is $x \times y \times z = 3 \times 3 \times 10$ μm^3 to maintain reasonable simulation time. Material refractive indices used are $n_{\mathrm{Si}} = 3.476$ and $n_{\mathrm{SiO2}} = 1.444$ and the simulation time step is 1.67×10^{-17} s according to the Courant criterion $\Delta t \leq 1/(c(1/(\Delta x)^2 + 1/(\Delta y)^2 + 1/(\Delta z)^2)^{½})$, where c is the speed of light in vacuum.

It should be noted the following limitation of this simulation procedure. From previous theoretical and experimental results on SWG couplers [70] an optimal coupler length of 50 μm was identified. Thereby, an optimal crossing geometry would require a total length of 100 μm (two 50 μm couplers). However, it is not possible to simulate a structure of this size using Optiwave's 3D FDTD tool. To circumvent this limitation, both the spatial resolution and the layout size were significantly reduced, which also implied an increased numerical loss. Thereby, the numerical simulations should not be regarded as a rigorous procedure to obtain a fully optimized structure, but rather as a way to assess the relative influence of several structural parameters. The increased length of the fabricated SWG couplers, compared to the simulated structures, is expected to improve the taper loss, as it is demonstrated in section 3.3. For a subwavelength taper, the average index change will be much greater for a short taper than the average index change of a long taper. Effective medium theory was not used to model the SWG taper because of the varying width and pitch, which would result in a volume grating. Modeling in FDTD preserves the grating features that are actually fabricated. To conservatively estimate the loss of the SWG taper, the actual geometry was used, rather than an effective medium homogenization.

The simulation layout for a Si wire waveguide with a SWG crossing is shown in Fig. 3.1(a), where Λ_i and Λ_f are the initial and final grating pitches, w_i and w_f are the initial and final segment widths, a = 150 nm is the segment length and h = 260 nm is the Si thickness in the SOI wafer. This layout was used to calculate loss, whereas the layout inset in Fig. 3.1(a) was used to calculate crosstalk. A continuous wave (CW) fundamental mode of a 450 nm × 260 nm wire waveguide at λ = 1.55 μm is used as the input field and optimization is performed for TE polarization. Mode mismatch loss is calculated as the power coupled to the fundamental mode of the output wire waveguide, whereas crosstalk is calculated as the power coupled to the fundamental mode of the intersecting waveguide.

To reduce the mode mismatch loss from a wire waveguide to SWG in Fig. 3.1(a), an adiabatic transition is ensured by a linear chirp (from Λ_i = 200 nm to Λ_f = 300) and taper (from w_i = 450 nm to w_f in the range of 200 nm – 350 nm) over 12 grating segments. The taper section is followed by 8 SWG segments with a constant pitch of 300 nm and a width of 300 nm (with a = 150 nm, i.e., a constant duty cycle of 50 %). The intersecting SWG structure has the same grating parameters, while the center segment is square to ensure an identical geometry for both waveguides. For each w_f, the center segment dimensions are set to match the area of the adjacent SWG grating segment ($w_f \times a$) ensuring a constant effective index for these adjacent segments. After the crossing point, an identical geometry is used for transition back to a wire waveguide (Fig. 3.1(a)).

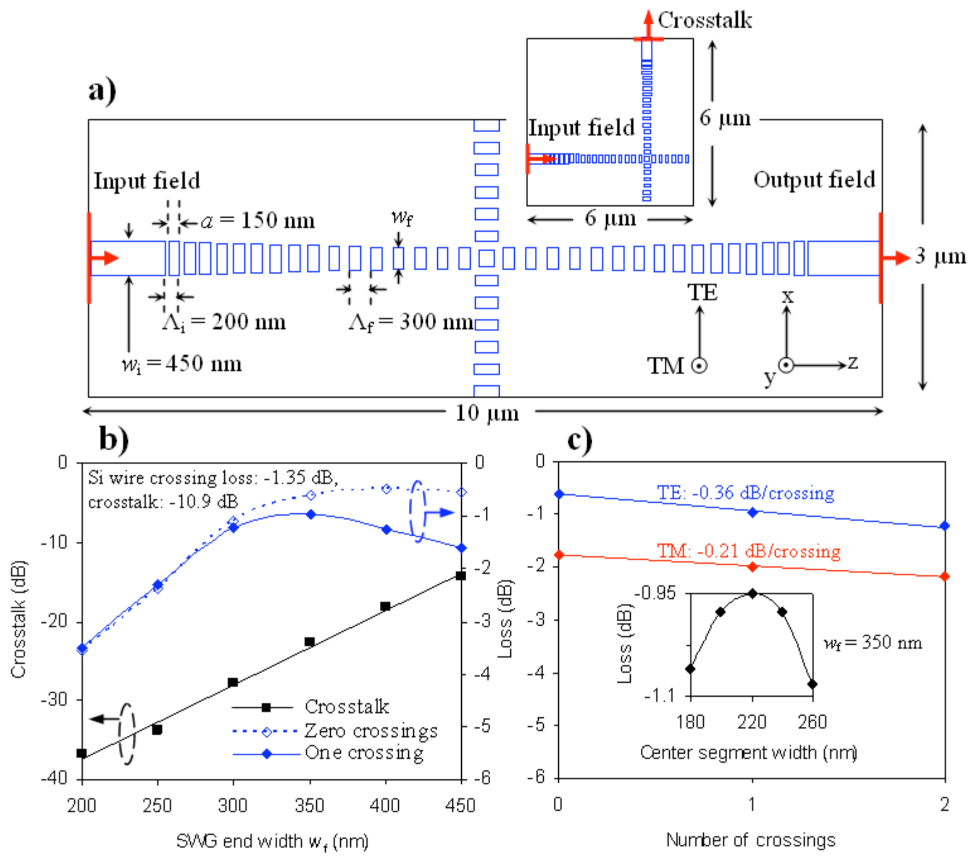

Fig. 3.1. a) Top view of the 3D FDTD simulation layout for a Si wire waveguide with a SWG crossing, where Λ_i and Λ_f are the initial and final grating pitches, w_i and w_f are the initial and final segment widths and a = 150 nm is the segment length. Inset in (a) shows the layout for estimating crosstalk. b) Loss for zero SWG crossings (open diamond symbols), loss for one SWG crossing (full diamond) and crosstalk (square) for w_f in the range of 200 nm to 350 nm for TE polarization at λ = 1.55 μm. Si wire crossing loss (-1.35 dB) and crosstalk (-10.9 dB) are indicated for reference. c) SWG loss per crossing for TE (blue) and TM (red) polarizations for w_f = 350 nm. Inset in (c) shows loss for one SWG crossing with varying center square segment width w.

Figure 3.1(b) shows zero SWG crossings loss (SWG structure with no intersecting waveguide), and one SWG crossing loss and crosstalk calculated for various taper widths w_f. As reference, calculated Si wire (width of 450 nm) crossing loss is -1.35 dB, while crosstalk is -10.9 dB. Insertion loss for a SWG structure without an intersecting waveguide increases with narrower taper widths as the transition becomes less adiabatic. For a SWG structure with one intersecting waveguide, loss first decreases with narrower tapers (until w_f = 350 nm) due to reduced crosstalk, then loss increases as the non-adiabatic taper loss dominates. Insertion loss is ultimately limited by a comparatively short 3 μm taper (12 SWG segments), which was chosen as a tradeoff with simulation time (20 hours). The loss penalty for adding a single crossing decreases significantly with narrower taper widths, and is as small as of -0.13 dB at a taper width of w_f = 300 nm. For narrower taper widths, loss penalty is dominated by the large width change (w_i to w_f) over the 3 μm long taper. For a single crossing, crosstalk performance of -37 dB is calculated for a taper width of 200 nm, which is nearly a 30 dB improvement compared to a direct crossing of Si wires. At wider taper widths, coupling is increased to the intersecting waveguide mode, which deteriorates crosstalk as it is shown in Fig. 3.1(b).

To determine loss per SWG crossing, w_f = 350 nm is used to minimize taper insertion loss (Fig. 3.1(b)). Loss per crossing is calculated as the slope of the linear fit to the insertion loss from three structures, comprising 0, 1 and 2 crossings. For two crossings to fit in the layout (Fig. 3.1(a)), the spacing between them was 4 grating segments. Identical taper geometries were used for these three structures. Using this approach, the taper loss is factored out from the calculated loss per single crossing. Figure 3.1(c) shows that for TE polarization the loss is -0.31 dB/crossing, while for TM polarization the loss is -0.21

dB/crossing. This is a 1 dB loss decrease compared to the direct wire crossing loss of -1.35 dB for TE polarization (Fig. 3.1(b)).

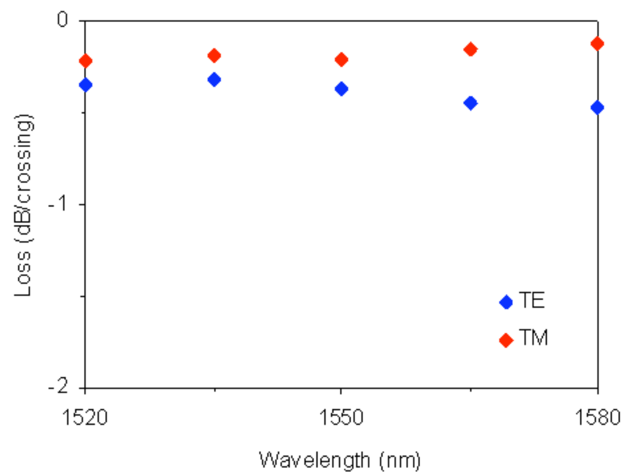

Fig. 3.2. Spectral dependence of simulated loss for a crossing structure with w_f = 350 nm for TE (blue) and TM (red) polarizations for a wavelength range of 1520 nm – 1580 nm.

Wavelength dependence of the crossing structure was also calculated. Figure 3.2 shows the spectral dependence of simulated loss for a crossing structure with 350 nm tip width, with a loss variation of < 0.1 dB for TE and TM polarizations for a wavelength range of 1520 nm – 1580 nm.

The inset in Fig. 3.1(c) shows one SWG crossing loss (w_f = 350 nm) for different widths of the center square segment indicating optimal performance at w = 220 nm. Such a square segment has the same area as the adjacent segments with dimensions $a \times w = 150 \times 350$ nm^2, which is consistent with effective medium theory, i.e. no change in the effective medium for these SWG segments). Simulations predict a minimal (-0.05 dB) loss penalty for a center square segment of w = 220 nm in a SWG waveguide with nominal segment dimensions $a \times w = 150 \times 350$ nm^2.

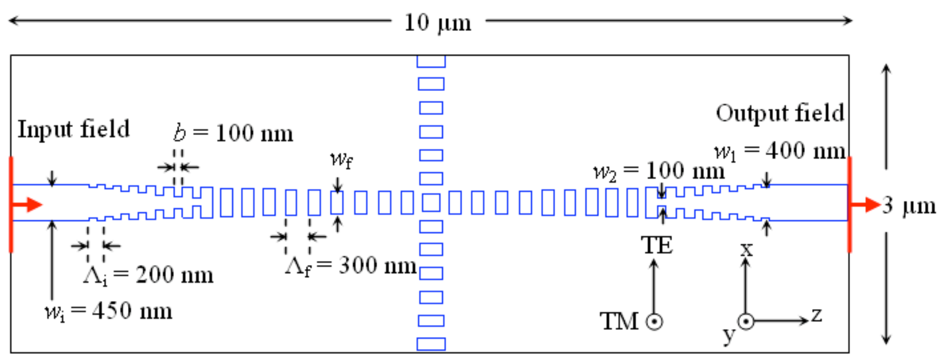

Fig. 3.3. Top view of the 3D FDTD simulation layout for a Si wire waveguide with a SWG crossing using bridging segments to reduce taper loss, where b = 100 is the bridging segment length and w_1 = 400, w_2 = 100 nm are the start and the end widths of the bridging segments.

To further refine the taper design and reduce insertion loss, bridging segments are implemented, as shown in Fig. 3.3. The bridging segments have constant length of b = 100 nm and their width varies from w_1 = 400 to w_2 = 100 nm. Using this technique, FDTD predicts taper back-to-back insertion loss is reduced from -0.61 dB (Fig. 3.1(b)) to -0.46 dB at w_f = 350 nm for TE polarization at λ = 1.55 μm. Figure 3.1(b) indicates a compromise between optimizing SWG crossing loss and crosstalk, since the short non-adiabatic tapers dominate loss. To minimize loss due to non-adiabatic tapers, for fabrication the design used 50 μm long tapers with bridging segments as discussed in the next section. An important added advantage of using the bridging segments is the increased minimum gap size from 50 nm (Fig. 3.1(a)) to 100 nm (Fig. 3.3). While electron beam lithography is used to fabricate the structures, a minimum feature size of 100 nm is compatible with CMOS 193 nm optical lithography process. The minimum feature size is what dictated the bridging segment geometry. The idea here is to have a constant SU-8 gap size of 100 nm until the linearly chirped pitch surpasses that value. The reason for the bridging segments is that the largest scattering source is the first wire waveguide to SWG segment transition.

Simulations were also carried out for a crossing implemented with conventional 3 μm long tapers having w_f = 150 nm, which match the mode delocalization of a SWG waveguide w_f = 300 nm (Chapter 2, Fig 2.2). Figure 3.4 shows the loss per crossing for a conventional w_f = 150 nm taper crossing.

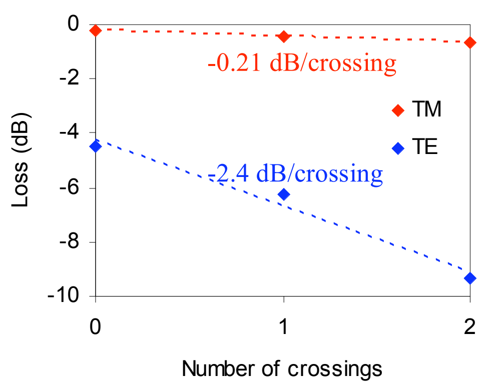

Fig. 3.4. Loss per crossing for a conventional taper crossing with w_f = 150 nm for TE (blue) and TM (red) polarizations at λ = 1.55 μm.

Loss for TE polarization was -2.4 dB/crossing with a crosstalk of 13 dB. The higher loss, compared to a conventional straight waveguide crossing (w_f = 450 nm, Fig. 3.1(b)), is due to the intersecting waveguide acting as a diffraction slit on the delocalized TE mode. Insertion loss was -4.3 dB due to an aggressive taper (450 nm to 150 nm) compared to the equivalent SWG (450 nm to 300 nm). For TM polarization, loss was -0.21 dB/crossing, which is comparable to the SWG crossing (Fig. 3.1(c)). The extreme polarization dependence of this taper crossing is a direct result of the different intensity distribution for the TE and TM modes, where the TM mode's evanescent tails do not propagate through the intersection, but above and below it reducing loss. Insertion loss for TM polarization was -0.22 dB. This taper crossing illustrates the advantage of using SWG segmentation, including low polarization dependent loss by suppressing diffraction from the intersecting waveguide and a wide 300 nm segment to delocalizing the mode to an equivalent narrow 150 nm conventional taper. The 150 nm wide conventional taper was used as it has the same mode delocalization as the SWG waveguide, and mode delocalization across the crossing point was the concept behind the design. Therefore, two different waveguides, each having the same mode delocalization, are compared. This clearly shows the advantage of the SWG, as there was no diffraction slit effect as observed in the conventional 150 nm wide taper crossing.

3.3 Design and fabrication

Subwavelength grating crossing structures were implemented in a 6.1 mm long test chip. In the optimized design, silicon wire waveguides (w = 450 nm) were transformed to the SWG straight waveguide using 50 µm long taper with bridging segments (Fig. 3.3) followed by a 350 µm long SWG section with constant pitch, width and duty cycle. An identical taper was used for the transition back to a wire waveguide. To determine loss per crossing, crossing structures were implemented with 0, 1, 5, 10, 20, 40 and 80 crossings for two different SWG parameters sets **A**: Λ_i = 200 nm, Λ_f = 400 nm, w_i = 450 nm, w_f = 300 nm, a_i = 150 nm, a_f = 200 nm and **B**: Λ_i = 200 nm, Λ_f = 300 nm w_i = 450 nm, w_f = 300 nm and a_i = a_f = 150 nm. To estimate the SWG taper loss 20, 40 and 60 tapers were concatenated with parameters from design **A**. A set of Si wire waveguides was fabricated with 0, 5, 20 and 40 crossings for a reference measurement.

Commercially available SOI substrates was used with 0.26 μm thick silicon and 2 μm thick buried oxide (BOX) layers. Electron beam lithography was used to define the waveguide layout in high contrast hydrogen silsesquioxane resist, which formed SiO_2 upon electron beam exposure. Inductively coupled plasma reactive ion etching (ICP-RIE) was used to transfer the waveguide layout onto the silicon layer. Samples were coated with a 2 μm thick polymer (SU-8, $n \sim 1.577$ at $\lambda = 1.55$ μm), then cleaved into separate chips and facets polished.

Figure 3.5 shows scanning electron microscope (SEM) images of fabricated SWG crossings including multiple SWG crossings (Fig. 3.5(a)), one SWG crossing (Fig. 3.5(b)), detail of the crossing region (Fig. 3.5(c)) and SWG straight waveguide (Fig. 3.5(d)) prior to SU-8 coating. From the SEM images it was determined that a fabrication bias of 50 nm was present. Therefore the actual dimensions of the SWG are $\Lambda = 300$ nm and $w = 250$ nm with a duty cycle of 33%. Actual wire waveguide width is 400 nm.

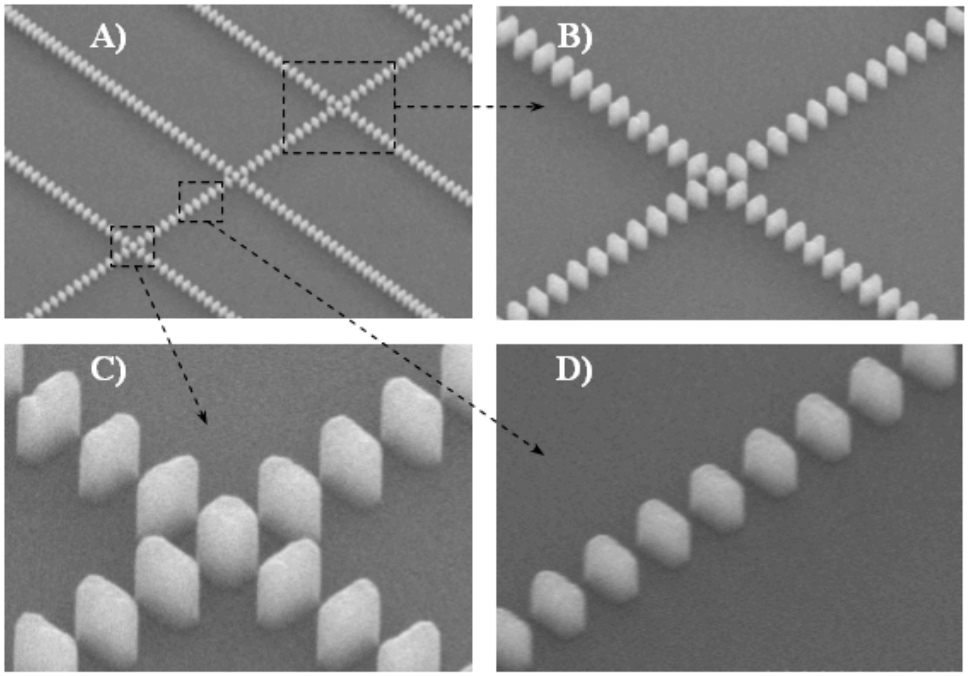

Fig. 3.5. Scanning electron microscope images of SWG crossings: a) multiple SWG crossings, b) one SWG crossing, c) detail of the crossing region with square center segment (220 nm × 220 nm) and d) SWG straight waveguide.

3.4 *Experimental results*

A polarization controller with a broadband (3 dB bandwidth of λ = 1.53 μm - 1.56 μm) amplified spontaneous emission (ASE) source was used to minimize Fabry-Pérot (FP) cavity effects from the chip facets. Since the ASE source in incoherent, the reflections from the chip facets result in reduced FP fringe contrast vs. a coherent source.

To couple the light into the chip, a lensed fibre was used resulting in a Gaussian beam waist of ~2 μm and a SWG fibre-chip coupler as described in [70]. Light is coupled out of the chip using another SWG coupler and subsequently focused by a microscope objective lens onto an InGaAs photodetector.

Crossing loss was estimated by measuring SWG structures with 0, 1, 5, 10, 20, 40 and 80 crossings, where loss per crossing is determined as the slope of a linear fit of these measurements. Structures with varying number of waveguide crossings all have identical wire waveguide length, which eliminated the wire propagation loss from the loss-per-crossing measurement. Wire waveguide propagation loss was -3.1 dB/cm for TE and -3.2 dB/cm for TM polarizations for $\lambda = 1.55$ μm, as measured on independent waveguide loss test structures. These wire waveguides dimensions were based on previous experimental results for high confinement and low loss for both polarizations. Figure 3.6 shows loss for SWG crossings ($\Lambda_f = 400$ nm and $\Lambda_f = 300$ nm) compared to direct wire waveguide crossings. For direct wire crossings, loss is -0.975 dB/crossing for TE and -0.763 dB/crossing for TM polarization. Using a SWG crossing with $\Lambda_f = 400$ nm, TE loss is reduced to -0.070 dB/crossing and TM loss to -0.067 dB/crossing, indicating a PDL of < 0.005 dB/crossing. Optimal performance was achieved for a SWG with $\Lambda_f = 300$ nm, where TE loss is -0.023 dB/crossing and TM loss is -0.037 dB/crossing (PDL ~ 0.01 dB/crossing). This is 30 times loss reduction compared to direct wire crossing. An obvious improvement compared to FDTD simulation predictions can be attributed to using longer tapers (50 μm instead of 3 μm) and the constrained layout size and resolution of the FDTD simulations.

The PDL at zero SWG crossings (TE = -6.9 dB, TM = -9.7 dB) compared to zero wire crossing (TE = -5 dB, TM = -7 dB) is attributed to the PDL of the fibre-chip coupler and the wire waveguide itself. The increased PDL for zero SWG crossings (0.8 dB) in Fig. 3.5(d) is the result of the PDL of the two extra SWG tapers used. Subwavelength grating taper loss was estimated by measuring structures with 20, 40 and 60 concatenated 50 μm long SWG tapers with the ASE source, where the taper loss is the slope of a linear fit of these measurements. The SWG taper had a measured TE loss of -0.296 dB and TM loss of -0.485 dB as shown in Fig. 3.7.

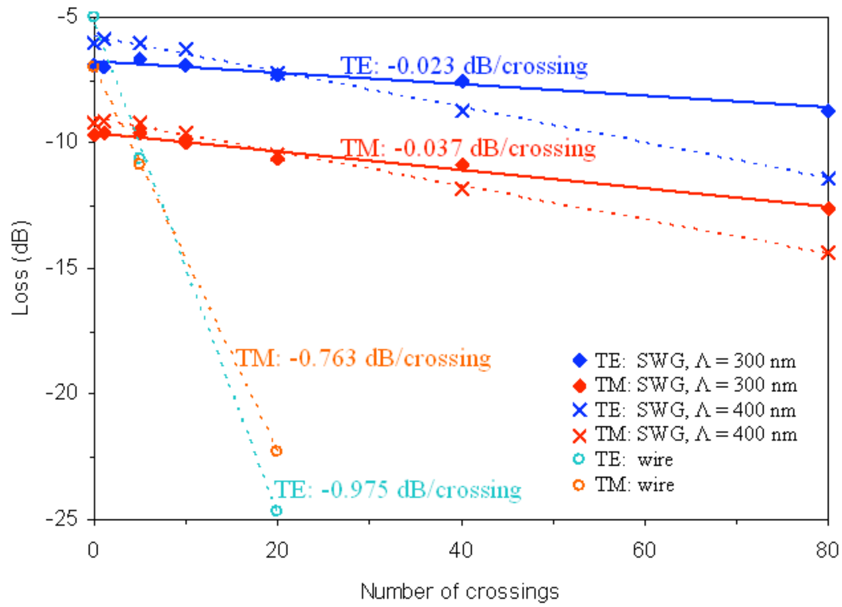

Fig. 3.6. Measured loss for SWG crossings with Λ = 300 nm for TE (blue diamond) and TM (red diamond) polarization and Λ = 400 nm for TE (blue cross) and TM (red cross) polarization using a broadband ASE source. Loss for direct wire crossings is shown for comparison for TE (green circle) and TM (cyan circle).

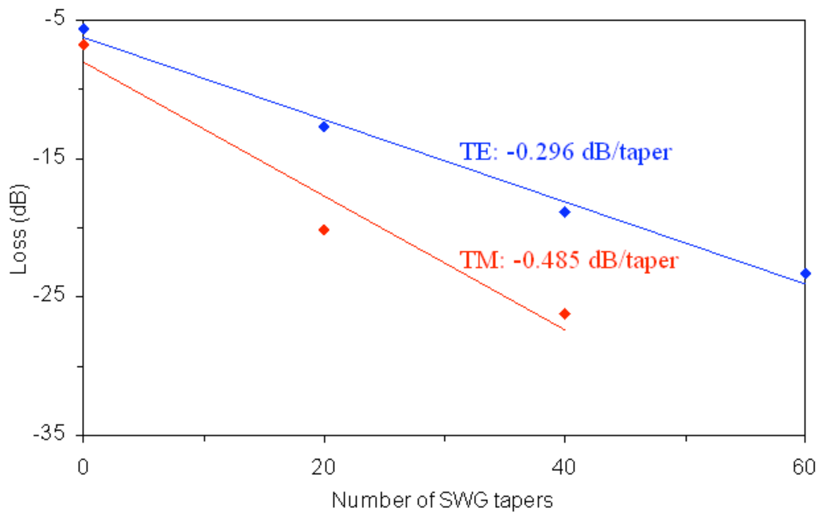

Fig. 3.7. Measured loss for a 50 µm long SWG taper with Λ_f = 400 nm and w_f = 300 nm for TE (blue) and TM (red) polarization using a broadband ASE source.

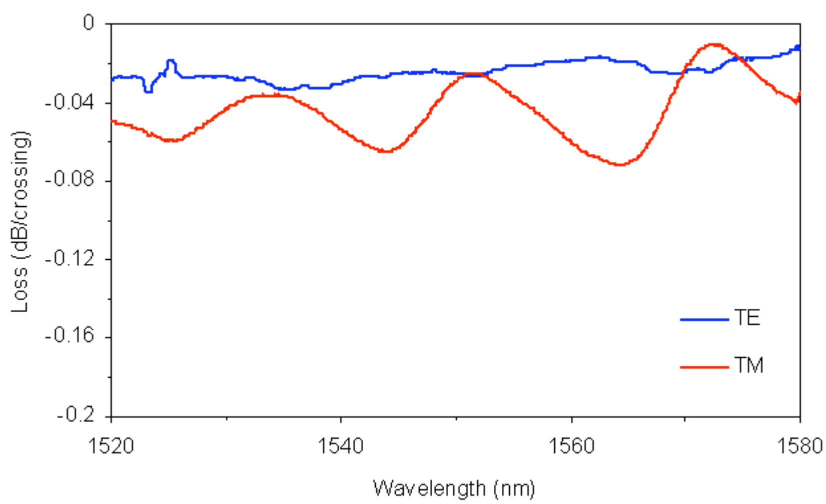

Fig. 3.8. Measured loss per crossing for a SWG crossings with Λ = 300 nm for TE (blue) and TM (red) polarizations using a tunable external cavity semiconductor laser.

Using a tunable external cavity semiconductor laser, the loss was measured for 10, 20, 40 and 80 crossings. Loss per crossing was estimated as the slope of the linear fit to these measurements for λ = 1520 nm – 1580 nm. Figure 3.8 shows the measured wavelength dependence of loss per crossing. The TE loss is -0.025 dB/crossing and TM loss is -0.045

dB/crossing at λ = 1545 nm, in accordance with the ASE measurements (ASE center wavelength of 1545 nm). Some ripple (~0.06 dB/crossing) in the TM loss per crossing is due to the increased TM reflection of the SWG couplers, which also results in an increased taper loss for TM polarization (Fig. 3.7), yielding a Fabry-Pérot cavity effect. The measured loss variation with wavelength is minimal, i.e. below 0.02 dB for TE and 0.06 dB for TM polarizations, in a wavelength range of 1520 nm – 1580 nm.

Crosstalk was estimated by coupling the light into a waveguide with a single SWG crossing and measuring the power from the output aperture of the intersecting waveguide. Crosstalk for both SWG crossings (Λ_f = 400 nm and Λ_f = 300 nm) was better than -40 dB, which is approximately a 25 dB improvement compared to crosstalk measured for direct crossings of Si wire waveguides. Indeed, with narrower taper widths the mode delocalizes further and the crosstalk is expected to improve, as predicted by FDTD simulations in Fig. 3.1(b). However, there is a limit to expanding the mode size beyond the BOX thickness, which is 2 μm in SOI wafers used, since this would result in a loss penalty due to light leakage to the substrate.

In terms of fabrication tolerances, the subwavelength nature of these structures results in a spatial refractive index averaging, such that the effects of fabrication imperfections are expected to be alleviated compared to resonant photonic structures such as photonic crystals. As pointed out in the previous section, from the SEM images it was determined that a fabrication bias of 50 nm was present, yielding a deviations of 17 % and 33 % compared to designed values of segment width and length respectively. Notwithstanding this fabrication error, the structure still performs remarkably well, both in terms of crosstalk and loss (Fig. 3.6).

3.5 Summary

Achieved is a new waveguide crossing principle based on subwavelength grating waveguides, including the simulation, design and experimental demonstration of a solution to **Objective 2: Efficient waveguide crossing** for high index contrast (SOI) waveguides. The measured loss of the fabricated structures is as low as -0.023 dB/crossing, polarization dependent loss is minimal (0.02 dB/crossing) and crosstalk is <-40 dB. An important advantage of these subwavelength structures is that they can be fabricated with a single etch step. Subwavelength grating crossings have the potential to facilitate massive interconnectivity and minimize the device footprint for future complex planar waveguide circuits. Subwavelength grating crossings are particularly promising for all SWG circuits where the low loss per crossing can be fully exploited. This chapter also demonstrates SWG mode converters for the transition between a wire waveguide and a SWG waveguide. The next chapter builds on those results with a theoretical analysis of SWGs as mode converters for slab waveguides of different geometries.

4. Subwavelength Grating Mode Converters

4.1 Principle

Mode converters are important to minimize the loss between waveguides of different geometries. The previous chapter developed mode converters between a wire waveguide and a SWG waveguide. This chapter presents a solution to **Objective 3: Efficient mode converters** for slab waveguides of different geometries. Slab waveguide mode converters are explored because of the practical applications to array waveguide gratings (AWGs) and echelle grating. Etched polarization compensators in both AWGs and echelle gratings result in a mode mismatch between the compensator slab and the combiner slab. Also, the main source of intrinsic loss in an AWG is the mode mismatch between the slab waveguide and the waveguide array. The solution proposed uses a subwavelength grating (SWG) transition region to minimize both fundamental mode mismatch loss and coupling to higher order modes. By creating a gradient effective index region in the direction of propagation, efficient vertical mode transformation can be achieved between slab waveguides of different core thickness. The solutions is innovative because the structures that are propose can be fabricated by a single etch step, yet provide flexible control of the refractive index.

According to effective medium theory, different optical materials within a sub-wavelength scale can be combined, approximately as an effective homogeneous material. For the SOI waveguide platform, the two obvious choices for the high and low index materials to create the effective medium are silicon (waveguide core) and silica (cladding). A gradual change in the ratio of Si & SiO_2 materials along the light propagation direction (Fig. 4.1, z-axis) results in a corresponding effective index change of the composite medium. This principle is used to create a transition region (*T*, Figs. 4.1(b) and 4.1(c)) between two slab waveguides (*A* and *B*, Figs. 4.1(b) and 4.1(c)) of different thicknesses or a slab waveguide and a waveguide array (Fig. 4.1(d)). In the following analysis these structures are studied using 3D FDTD simulations. In particular, the focus is on reducing loss, higher order mode excitation and the PDL of these structures.

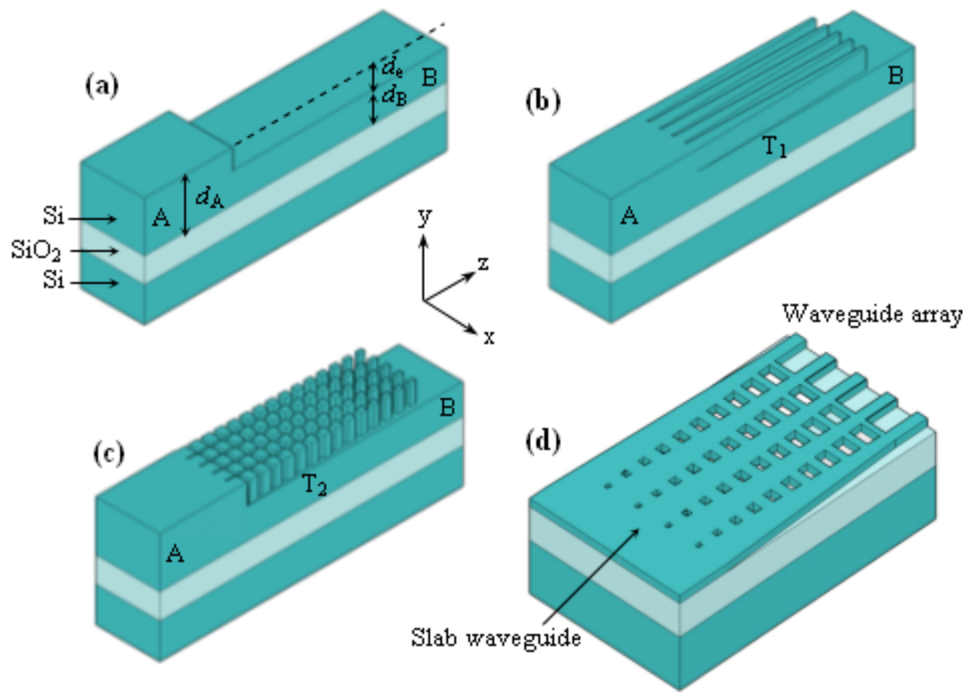

Fig. 4.1. 3D schematics of junctions between two waveguides of different geometries, with: a) conventional single step interface, b) 1D grating, triangular SWG transition region, and c) 2D grating, triangular-transverse SWG transition region. d) SWG structure at the boundary between slab waveguide and a waveguide array.

4.2 Design and Simulation

4.2.1 SWG transition between slab waveguides of different core thicknesses

Three geometries of mode transformers are compared between slab waveguides of different core thicknesses: the conventional single-step (Fig. 4.1(a)), the triangular SWG transition region (T_1, Fig. 4.1(b)) and the triangular-transverse transition region (T_2, Fig. 4.1(c)). For the conventional single-step, the simulation was performed for an initial slab of thickness d_A and length 2 μm, followed by a 20 μm long thinner slab waveguide *B*. This conventional structure (an abrupt effective index mismatch) is a benchmark design for assessing the SWG designs. The first SWG mode transformer design employs triangular SWG structures (Fig. 4.2(a)) with length 20 μm and pitch 0.3 μm, to create a gradient index (GRIN) effect similar to the anti-reflective structure reported in [73]. The structure length was chosen as a compromise between simulation time demands and ensuring an adiabatic mode transition between the different slab waveguide thicknesses. The second design, a SWG triangular-transverse mode transformer (Fig. 4.2(b)) has the triangular structures identical to the first structure, but with a transverse SWG added. The geometrical parameters of these transverse gratings are Λ_i = 180 nm, Λ_f = 220 nm, a_i = 130 nm and a_f = 50 nm, where Λ_i and Λ_f are the initial and final grating pitch and a_i and a_f are the initial and final Si segment lengths (Fig. 4.2(b)). These grating parameters ensure suppressed diffraction (periodicity of the grating is even smaller than the SWG waveguide – see dispersion diagram of Fig. 2.3) and a gradual transition from the initial slab waveguide to the thinner slab waveguide. These parameters also ensured that the minimum gap size and the minimum feature size of the grating is 50 nm. Here the subwavelength transverse grating duty ratio $r(z) = a(z)/\Lambda(z)$ decreases along the light propagation direction, as proposed in [70] to ease the transition.

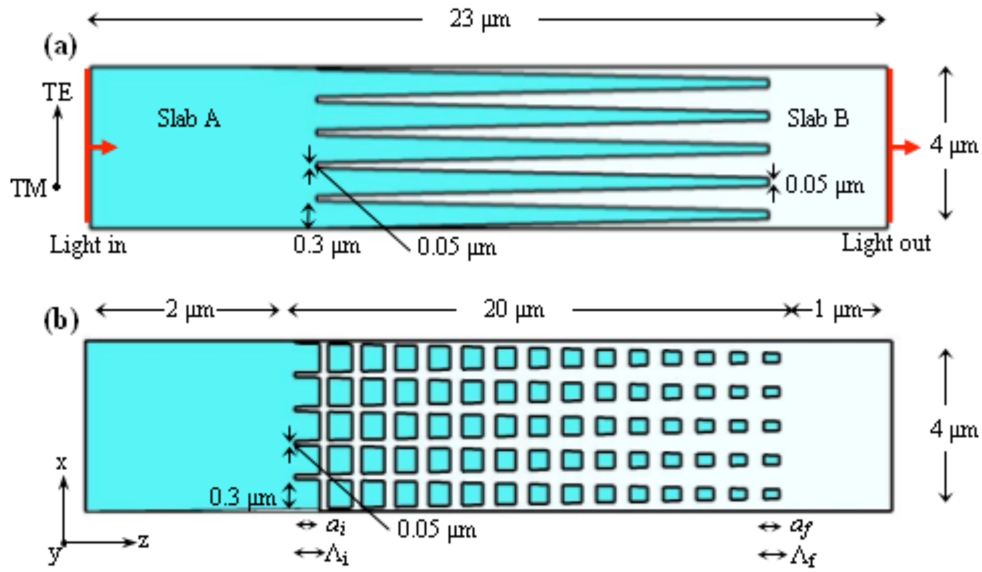

Fig. 4.2. Top view of mode transformer. a) Triangular SWG structure; b) Triangular-transverse SWG structure. 3D FDTD simulations were performed for both structures for three different thicknesses of slab waveguide A: d_A = 0.5 μm, 1.0 μm and 1.5 μm, with variable etch depth (d_A-d_B).

3D FDTD simulations were performed for a layout size of $x \times y \times z = 4 \times 4 \times 24\ \mu m^3$ on the SOI waveguide platform with material refractive indexes $n_{Si} = 3.476$ and $n_{SiO2} = 1.444$ (SiO_2 cladding). The mesh size used for the simulations was $\Delta x \times \Delta y \times \Delta z = 20 \times 20 \times 20\ nm^3$, while the time step $\Delta t = 3.3 \times 10^{-17}$ s was set according to the Courant limit. For each design (conventional single-step, triangular SWG and triangular-transverse SWG), three initial slab waveguide (A) thicknesses of d_A = 0.5 μm, 1.0 μm and 1.5 μm were evaluated. For each slab waveguide thickness, simulations were run for several etch depths $d_e = d_A - d_B$. The mode mismatch loss of each design was calculated as ratio of the power coupled to the fundamental mode of the thinner slab waveguide (*B*) and the input power. All simulations were performed by exciting the transverse field of the fundamental mode at a single wavelength of $\lambda = 1.54$ µm.

Using a first order effective medium theory approximation (Appendix B), an initial model of the upper cladding transition region for a triangular SWG is investigated similar to [73]. Due to the form birefringence of the triangular SWG structure, the first order effective medium theory approximation of the SWG transition will be polarization dependent. Figure 4.3 shows effective medium index change from Si (position z = 0 µm) to SiO_2 (position z = 20 µm) as a function of position for TE and TM polarization. From this estimate, it is evident that for TM polarization the effective medium index change is more gradual then for TE polarization, where there is a large initial effective medium index change from bulk Si.

Length dependence for a triangular SWG structure was assessed using 3D FDTD simulations for 5 µm, 10 µm and 20 µm long structures with $d_A = 1.0$ µm and $d_e = 0.4$ µm (40% etch). Figure 4.4 shows loss as a function of triangular SWG length, indicating reduced loss for longer structures. As predicted by the effective medium theory approximation (Fig. 4.3), TM polarization has a lower loss compared to TE polarization due to the superior TM adiabaticity. Longer triangular SWG lengths could not be assessed (though are expected to have further reduced loss) due to excessive simulation duration. In all subsequent simulations 20 µm long structures are used.

3D FDTD simulations were also used to assess a taper waveguide with a gradually changed thickness from 1.0 µm to 0.6 µm, over 20 µm. The calculated TE loss was −1.7 dB and TM loss −1.2 dB. This is a higher loss than for the optimal SWG structures, which seems counterintuitive. Here the conventional taper was discretized in the vertical direction, which effectively created several slabs (a coarse taper). The SWG structures were not discretized in the vertical direction. The discretization of the conventional taper was not at a subwavelength scale. This loss penalty appears to be a numerical artifact arising from the mesh granularity (20 nm x 20 nm x 20 nm).

Loss is expected to decrease with higher resolution mesh, but this would require computational resources beyond the current available capability. In addition, thickness tapering would require the extra fabrication complexity of greyscale lithography.

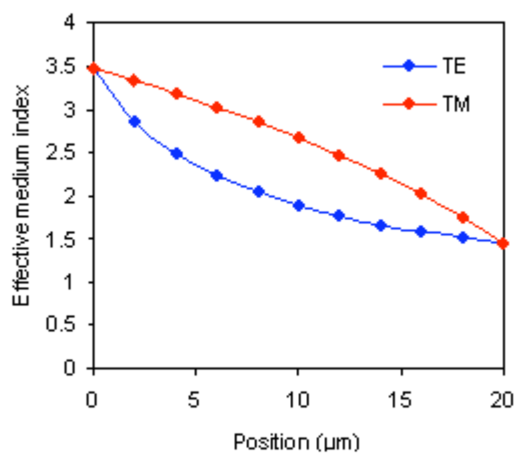

Fig. 4.3. First order effective medium theory approximation of effective index of SWG upper cladding transition region as a function of position (z in Fig. 4.1) for TE and TM polarization.

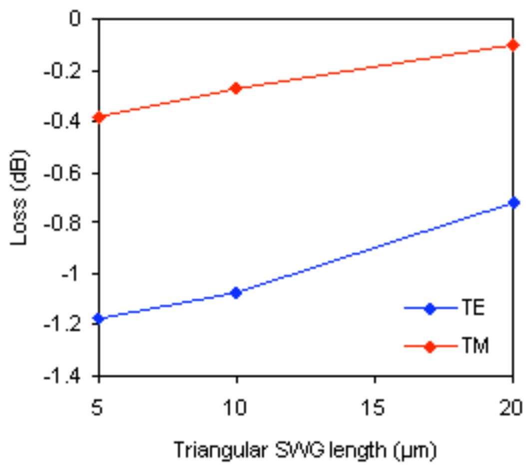

Fig. 4.4. Loss dependence for triangular SWGs of different lengths. TE and TM polarization, d_A = 1.0 μm, and d_e = 0.4 μm (40% etch). Loss is calculated as power transfer from the fundamental mode of slab waveguide *A* to the fundamental mode of slab waveguide *B* (Fig. 4.1(b)).

4.2.2 3D FDTD simulation results for TE polarization

Simulation results for TE polarized light at λ = 1.54 μm are shown in Fig. 4.5, indicating the loss incurred by the power transfer from slab waveguide *A* to the fundamental mode of slab waveguide *B* for d_A = 0.5 μm, 1.0 μm and 1.5 μm with various etch depths (in percentage of the initial slab waveguide thickness). A significant improvement in performance compared to the conventional single-step is presented. For example, at an initial slab thickness d_A = 1.5 μm (Fig. 4.5(a)) and etch depth of d_e = 0.6 μm (40% etch) the mode coupling loss for a conventional single-step is −2.6 dB. Using the triangular SWG mode transformer, mode coupling loss is reduced to −1.6 dB. The triangular-transverse grating yields a further loss reduction to −1.3 dB. For d_A = 1.0 μm (Fig. 4.5(b)), and d_e = 0.4 μm (40% etch), the mode coupling loss for a conventional single-step is −2.2 dB. By using the triangular grating, the loss is reduced to −0.7 dB, while with triangular-transverse SWG the loss is further reduced to −0.25 dB. In Fig. 4.5(b) there is a noticeable discontinuity in the calculated loss for the triangular grating etch depth range 0.4 μm to 0.5 μm, which is attributed to higher order mode excitation at $d_e = 0.5$ μm. For the 0.5 μm thick SOI slab (Fig. 4.5(c)) simulation results confirm that both the triangular and triangular-transverse SWGs have improved performance over the conventional single-step, with the triangular SWG having the smallest loss penalty. For the triangular and triangular-transverse mode transformers as d_A increases (0.5 μm, 1.0 μm, 1.5 μm), loss also increases for a given etch percentage. Since increasing d_A creates a larger vertical step (for the same etch percentage), the SWG transition from d_A to d_B is more abrupt resulting in increased loss.

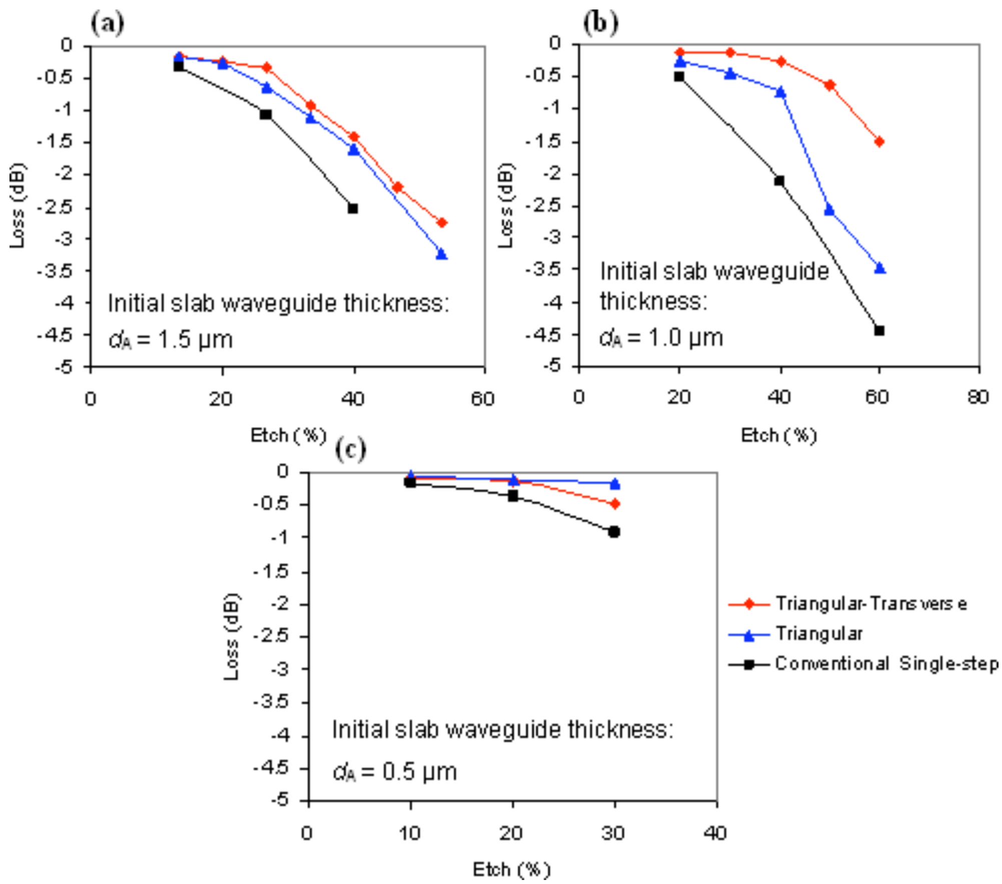

Fig. 4.5. Vertical mode transformer loss comparison for conventional single-step, triangular SWG and triangular-transverse SWG for TE polarization. a) Initial slab thickness d_A = 1.5 μm, etch depth range d_e = 0.2 μm – 0.8 μm (10% – 50% etch) ; b) d_A = 1.0 μm, d_e = 0.2 μm – 0.6 μm (20% – 60% etch); c) d_A = 0.5 μm, d_e = 0.05 μm – 0.15 μm (10% – 30% etch). Loss is calculated as power transfer from the fundamental mode of slab waveguide *A* to the fundamental mode of slab waveguide *B* (see Figs. 4.1(b) and 4.1(c)).

4.2.3 3D FDTD simulation results for TM polarization

Simulation results for TM polarized light at λ = 1.54 μm are shown in Fig. 4.6, indicating the loss incurred by the power transfer from slab waveguide *A* to the fundamental mode of slab waveguide B. Compared to TE polarization, here the trend is reversed, i.e. the triangular SWG loss is lower than triangular-transverse SWG loss, for all studied initial slab thicknesses d_A. For example, at d_A = 1.5 μm (Fig. 4.6(a)) and etch depth of d_e = 0.6 μm (40% etch) mode coupling loss for a conventional single-step is −1.2 dB. Using triangular-transverse SWG mode transformer, mode coupling loss is reduced to −0.6 dB, while for triangular SWG the loss is as low as −0.2 dB. For d_A = 1.0 μm (Fig. 4.6(b)), and d_e = 0.4 μm (40% etch) mode coupling loss for a conventional single-step is −3.2 dB. Using the triangular-transverse SWG the loss is reduced to −0.6 dB, while for triangular SWG the loss is as low as −0.1 dB. For the 0.5 μm thick SOI slab (Fig. 4.6(c)) and d_e = 0.15 μm mode the coupling loss for a conventional single-step is −1.6 dB. The loss is reduced to −0.7 dB and −0.3 dB with triangular-transverse and triangular SWG, respectively. Unlike for TE polarization, loss performance of the triangular SWG is superior to the triangular-transverse SWG. The excess loss of the triangular-transverse structure is attributed to the decreased confinement at the upper cladding boundary for TM polarization (compared to the triangular SWG) that arises from a reduced effective index due to the transverse segmentation. This results in an increased mode mismatch between the thinner slab waveguide (highly confined mode) and the transition region of the triangular-transverse SWG (reduced mode confinement). Amplitude mode profiles at the light output plane (Fig. 4.2) for d_A = 1.0 μm and d_e = 0.4 μm are shown in Fig. 4.7 indicating the overlap percentage Γ of the fundamental mode. It is observed that the SWG mode transformers have reduced higher order mode excitation compared to the conventional step.

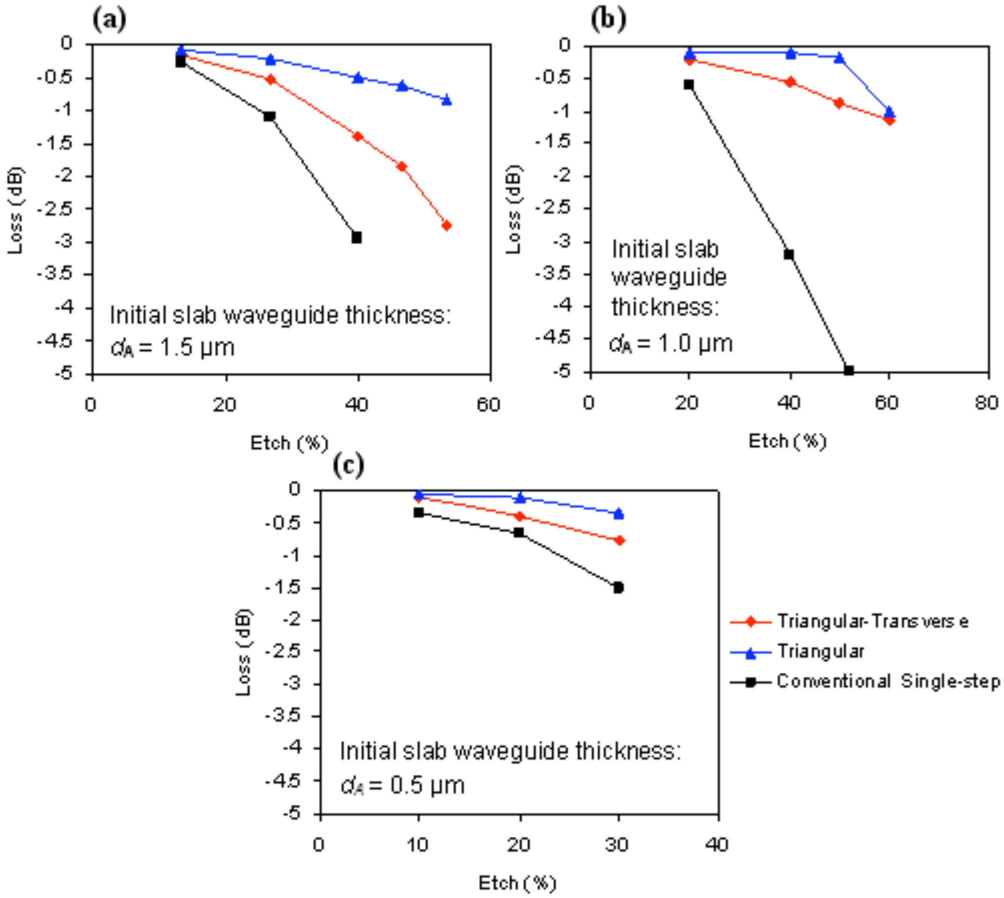

Fig. 4.6. Vertical mode transformer loss comparison for conventional single-step, triangular SWG and triangular-transverse, SWG for TM polarization. a) Initial slab thickness d_A = 1.5 µm, etch depth range d_e = 0.2 µm – 0.8 µm (10% – 50% etch); b) d_A = 1.0 µm, d_e = 0.2 µm – 0.6 µm (20% – 60% etch); c) d_A = 0.5 µm, d_e = 0.05 µm – 0.15 µm (10% – 30% etch). Loss calculated as power transfer from the fundamental mode of slab waveguide *A* to the fundamental mode of slab waveguide *B* (see Figs. 4.1(b) and 4.1(c)).

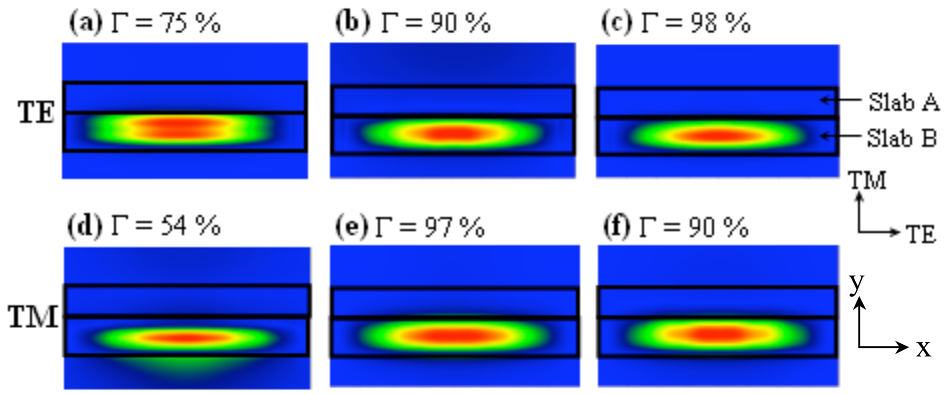

Fig. 4.7. TE (E_x field component) and TM (E_y field component) mode profiles for d_A = 1.0 µm and d_e = 0.4 µm. TE polarization: a) Conventional single-step, indicates higher order mode excitation, b) Triangular SWG showing higher mode mismatch than, c) Triangular-transverse SWG. TM polarization: d) Conventional etch indicates significant mode mismatch, e) Triangular SWG showing lower mode mismatch than, f) Triangular-transverse SWG.

4.2.4 SWG mode transformers with reduced polarization dependent loss (PDL)

The simulation results discussed in Sections 4.2.2 and 4.2.3 show that mode coupling loss, for both triangular and triangular-transverse SWGs, is polarization dependent. However, since triangular SWG loss is lower for TM polarization while triangular-transverse SWG loss is lower for TE polarization, a combination of the two types of SWG structures can be used to mitigate PDL. Here, two structures are proposed with reduced PDL (Fig. 4.8). The first structure comprises a triangular SWG followed by a triangular-transverse SWG of length L_T, as shown in Fig. 4.8(a). Figure 4.9 shows loss for TE and TM polarizations as a function of transverse SWG length L_T for d_A = 1.0 µm, d_e = 0.4 µm (40%) and triangular SWG length of 20 µm. The calculated PDL is negligible for a transverse grating length of 18 µm, where mode coupling loss for TE and

TM is ~-0.5 dB. The second approach to reduce PDL is to form a transverse SWG in the region between the triangular teeth as shown in Fig. 4.8(b). The geometrical parameters of these transverse gratings across continuous triangular structures are Λ_i = 180 nm, Λ_f = 220 nm, a_i = 130 nm and a_f = 50 nm (Fig. 4.8(b)). Using the same slab etch dimensions as in the structure of Fig. 4.8(a), simulation results show mode coupling loss for TE and TM is −0.2 dB and −0.38 dB, respectively. The advantage of this structure compared to partial transverse SWG is a decreased overall loss, but some residual PDL < 0.2 dB remains. It is believed that the latter may still be reduced by further optimization.

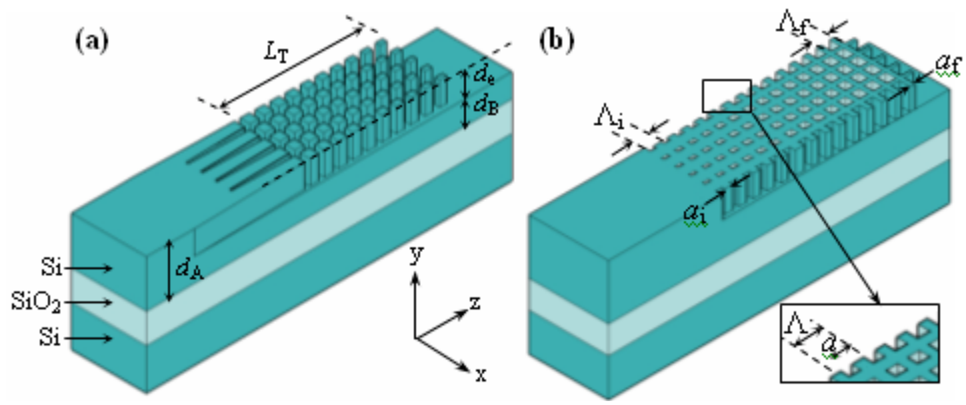

Fig. 4.8. 3D mode transformers with reduced PDL. a) Partial transverse SWG with length L_T; b) Transverse SWG in the region between the triangular teeth.

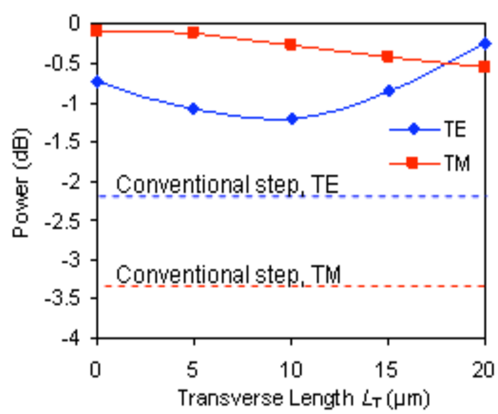

Fig. 4.9. Power coupled to the fundamental mode for a structure shown in Fig. 4.8(a). Negligible PDL is predicted for triangular-transverse length L_T ~18 μm. Dotted lines indicate the loss for a conventional step for TE and TM polarization, respectively.

4.2.5 SWG boundary between a slab waveguide and a waveguide array

To explore other potential applications of SWG mode transformers, sub-wavelength gratings are used to reduce the mode mismatch between the slab waveguide combiner and the waveguide array of an AWG. The main intrinsic source of loss in an AWG is coupling from the slab waveguide to the waveguide array. This loss is a consequence of different field distributions of the slab waveguide and the arrayed waveguides. As the continuous field in the slab waveguide propagates across the slab-array boundary, it couples to the discretized field of the array of waveguides. Here loss is particularly significant in high index contrast waveguides as the strong confinement results in increased reflection and mode mismatch. This effect can be reduced by optimizing the slab-array interface; for example, loss < 0.4 dB has been reported by employing a double-etch process [32]. Deep etched waveguides in the array are adiabatically tapered to shallow etched regions near the slab to create a gradual index transition; however, this implies increased fabrication complexity. Figure 4.10 shows an AWG schematic with a close-up of the slab-array boundary. Two structures are compared, namely a conventional taper (Fig. 4.10(a)) and a SWG taper (Fig. 4.10(b)). The latter is used to create an effective medium gradually matching the slab effective index to that of the waveguide array. Figures 4.11(a) and 4.11(b) show the layout dimensions of 2D FDTD simulations with a grid of $\Delta x \times \Delta y = 10 \times 10$ nm^2. Figures 4.11(c) and 4.11(d) show the field evolution along a conventional taper and a SWG taper. It is observed that higher order mode excitation is significantly suppressed for the SWG boundary. Figures 4.11(e) and

4.11(f) show the field amplitude profile in the array waveguides. Conventional taper loss is −1.4 dB, while using SWG structure loss is markedly reduced, to < −0.2 dB.

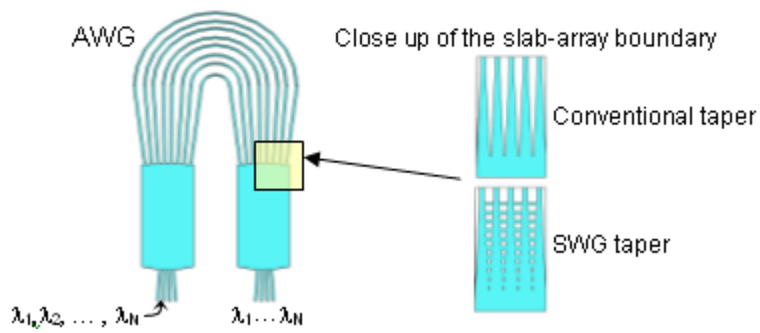

Fig. 4.10. AWG with close-up of the slab-array boundary using conventional tapers and SWG tapers to reduce loss and higher order mode excitation at the slab-array boundary.

In the SWG taper slab-array boundary, diffraction is frustrated as the grating period is less than the first order Bragg period, unlike in the mode transformer proposed for the low index contrast silica-on-silicon waveguide platform using a long period grating (LPG) [34]. Application of LPGs to a high contrast waveguide platform such as SOI is limited due to the prohibitive losses incurred at the interfaces between different LPG segments.

The minimum feature size achievable by e-beam lithography is ~50 nm; however there is a large profile ratio of minimum feature size to height in the structures proposed in Fig 4.1(a), 4.1(b) and 4.1(c). Deep etching was simulated to determine the limit of this approach, not to propose tall narrow structures as something easily fabricated. However, it is important to note that there are groups that have fabricated suspended SOI waveguides with tall narrow support columns by proton beam writing [84].

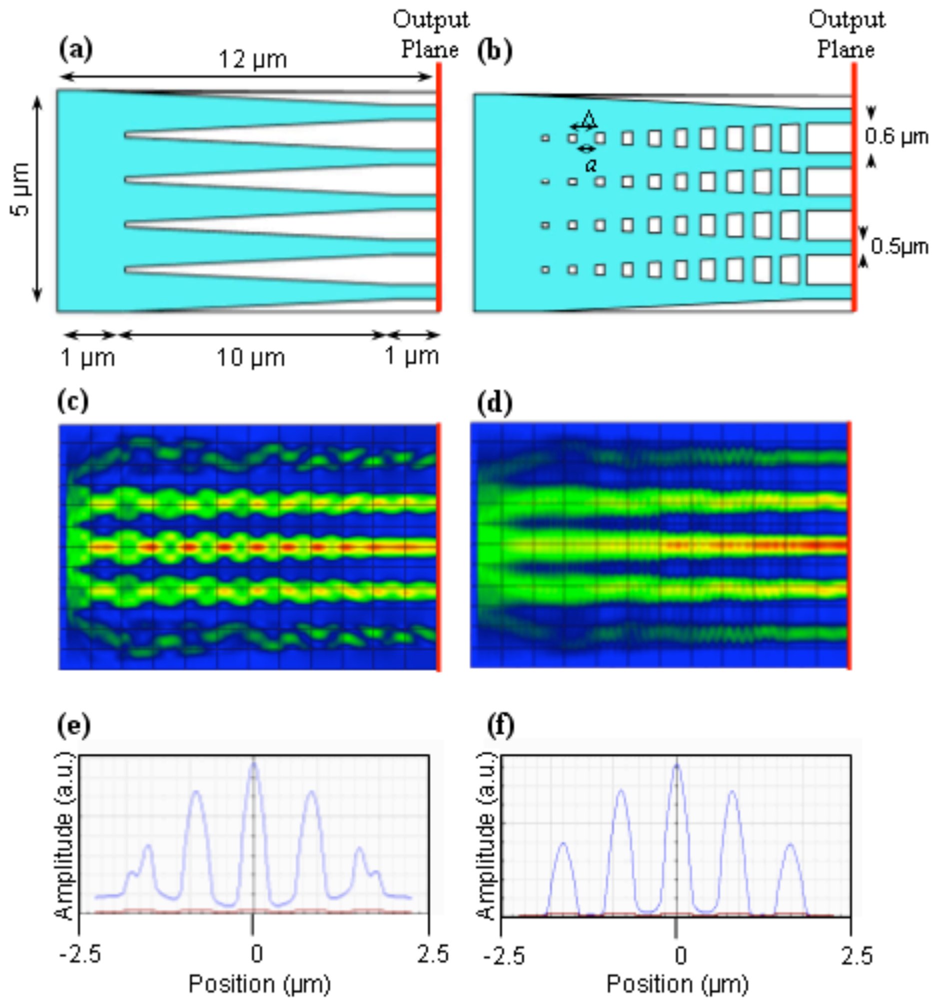

Fig. 4.11. Layout, mode evolution and field profiles for an AWG slab-array boundary. a) Conventional taper simulation layout. b) SWG taper simulation layout. c) Field evolution in conventional tapers, higher order mode excitation is noticeable. d) Field evolution in SWG taper with suppressed higher order mode excitation. e) Conventional taper field amplitude profile at the output plane of the waveguide array indicating the presence of higher order modes. f) SWG taper field amplitude profile at the output plane of the waveguide array indicating suppressed higher order mode excitation.

4.3 Summary

Achieved is a 3D FDTD simulations study of several new subwavelength grating mode transformers for mode coupling between high refractive index contrast (SOI) waveguides of different geometries, including different waveguide core thicknesses and a junction between a slab waveguide and a waveguide array. This is a solution to **Objective 3: Efficient waveguide mode converters** and is innovative because compared to conventional structures, the mode transformers significantly reduce loss, PDL and higher order mode excitation. For vertical mode transformers, the loss compared to a conventional step etch is reduced by up to 3 dB depending on the specific waveguide geometry, and PDL can be effectively mitigated. Using a SWG boundary between a slab waveguide and a waveguide array in a photonic wire AWG, a significant loss reduction from -1.4 dB to < -0.2 dB and a reduced higher order mode excitation are predicted. An important practical advantage of these subwavelength grating mode transformers is that they can be fabricated in a single etch step, yet allow for direct control of the effective index. Without the slab waveguide mode converters presented in this chapter, the demultiplexer device in the next chapter would not be possible.

5. Sidewall Spectrometer with Subwavelength Gratings

5.1 Motivation

Proposed is an original coarse wavelength division (de)multiplexer (CWDM) based on a single curved waveguide with an etched sidewall grating to solve **Objective 4: Demultiplexer design for high refractive index contrast waveguides**. Similar to the echelle grating demultiplexers, a benefit of this design is that the waveguide phased array is not required. This implies an obvious advantage of a smaller device size compared to an array waveguide grating (AWG). Furthermore, since the light propagates in a single waveguide, the effects of overall loss and phase error accumulation due to waveguide imperfections are reduced. This is in contrast to an AWG, where power is split in the phasar array and each arm experiences its own loss and phase error (ultimately leading to crosstalk) [19]. Since the efficiency of scattering from sidewall roughness is directly related to the interaction length as well as any roughness periodicity, minimizing the interaction length will reduce the detrimental effects of sidewall roughness. Unlike a typical waveguide echelle gratings demultiplexers, metallization is not needed in the device presented in this chapter. For an improved echelle grating reflectivity in thin (single-mode) SOI slab waveguides, the use of Bragg reflectors instead of metallizing have been suggested at the grating facets [20]. However, this may limit the maximum demultiplexer wavelength range, unlike in the proposed device, where broadband operation range is readily achieved (375 nm for the device reported in this chapter). Such a broad wavelength operation range is required for CWDM applications. This device can also be extended to DWDM applications by increasing the Rowland radius of the demultiplexer, thereby creating greater channel separation at the focal plane. It is also an interesting feature of the proposed device that, unlike echelle gratings, it allows a modification of both phase (for example, by pitch modification) and intensity (by grating apodization) of the diffracted field with no loss penalty, which is important for various applications, including mux/demux passband widening.

5.2 Device principle

Light comprising multiple wavelengths is coupled from the external port (typically a single mode optical fiber) into the input wire waveguide (Fig. 5.1). The light propagating in the input waveguide is diffracted in a direction normal to the waveguide axis by the sidewall grating. A second-order grating is used with the pitch $\Lambda = \lambda_0/n_{eff}$, where λ_0 is the central wavelength of the demultiplexer and n_{eff} is the effective index of the fundamental mode of the input waveguide. The grating is blazed to maximize diffraction efficiency for the -1st diffraction order that propagates towards the demultiplexer focal region. Conceptually, each grating tooth acts as a small prism partially reflecting the waveguide mode, via total internal reflection (TIR) at the grating facets, thereby increasing grating diffraction efficiency into the -1st order compared to the 1st order.

Based on the previous chapter's results, a subwavelength grating (SWG) with triangular teeth is used to reduce Fresnel reflection at the boundary between the trench lateral to the Si waveguide and the slab region. Such a triangular SWG acts as a graded-index (GRIN) medium, thereby suppressing Fresnel reflection at the silicon-silica boundary. Since diffraction effects are suppressed due to the subwavelength nature of the grating, the light passing from the trench to the slab waveguide is only affected by the effective average index of the GRIN SWG structure. Compared to single-layer AR coatings, the SWG GRIN structures can be readily produced using standard lithographic and etching techniques at the wafer level. Since the triangular SWG structure is based on the principle of an effective medium [76,77] in general and the GRIN effect in particular, it provides a larger spectral bandwidth compared to AR structures based on light interference.

The focusing property of the device is provided by curving the waveguide along an arc of radius $f = 2R$ (where f is the focal length) and centered on the demultiplexer centre wavelength focal point (F in Fig. 5.1). The receiver waveguides start at the Rowland circle [79] of radius R, tangential to the curved input waveguide.

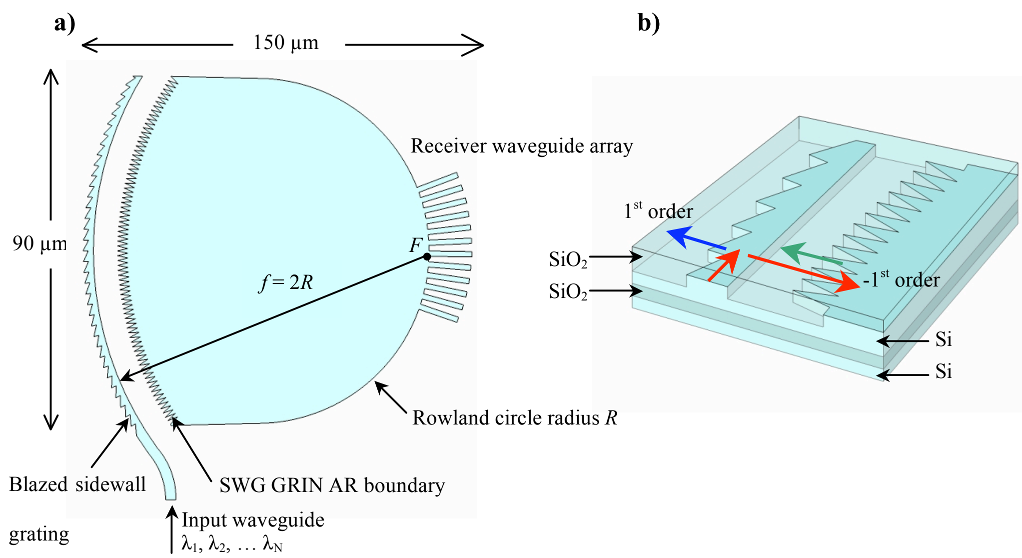

Fig. 5.1. (a) Demultiplexer schematics. The light propagating in the input waveguide is diffracted by a blazed sidewall grating and coupled to a slab waveguide via impedance matching SWG GRIN boundary. The waveguide is curved to provide focusing. Demultiplexed wavelength channels are intercepted by the receiver waveguides starting at the Rowland circle. (b) 3D cross section of the sidewall grating and SWG GRIN AR boundary.

5.3 Analytical model

The device is initially modeled using the 2D Kirchhoff-Huygens (Appendix D) diffraction integral [85]. The far-field $\Psi(x', y')$ with coordinates x' and y' along the focal curve, that is the Rowland circle of radius R, is adapted from the general case for this specific device whereby the integration path runs over the curved grating $C(x,y)$:

$$\Psi(x', y') = \int_C \frac{\psi(x,y)\exp\left[-i\left(\phi_w + \phi_s\right)\right]}{\sqrt{\lambda d}} G dC \quad . \tag{1}$$

In Eq.1, $\psi(x, y)$ is the near-field profile with coordinates x and y along the grating, φ_w is the phase accumulated in the input waveguide, φ_s is the phase accumulated in the slab region, λ is the wavelength, $d = [(x' - x)^2 + (y' - y)^2]^{1/2}$ is the distance between a grating facet and a specific position along the focal curve, and geometry (or inclination) factor is $G = (\cos\alpha + \cos\gamma)/2$, where α and γ are the angles between the normal of the grating facet and the incoming and outgoing light wavevector respectively. For this device, the discretized Kirchhoff-Huygens diffraction integral, i.e. sum of light contribution from all facets $j = 1,2, \ldots, N$ is used.

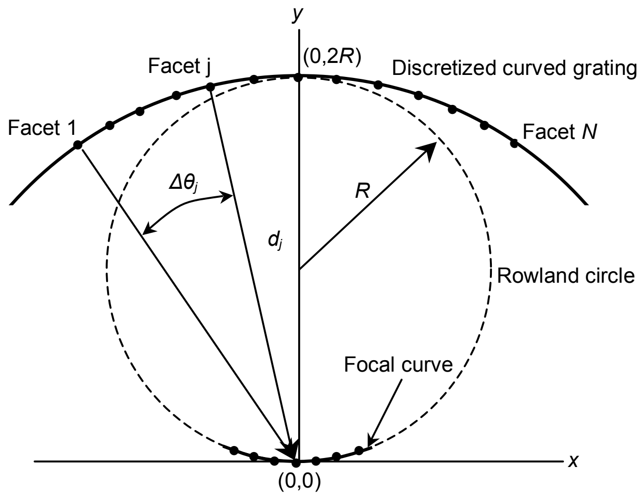

Fig. 5.2. Schematic of the analytical model. Points along the grating curve represent the facets j = 1,2,…, N. R is the Rowland radius, $\Delta\theta_j$ is the angle between the 1^{st} and j^{th} facet, and d_j is the distance from the j^{th} facet to a specific point at the focal curve (Rowland circle). For each point along the discretized focal plane, the sum of light contribution from all the facets is calculated.

The device schematic used in the analytical model is shown in Fig. 5.2. It is observed that the phase contributions are: $\varphi_w = k_w 2R\Delta\theta_j$ and $\varphi_s = k_s d_j$, where k_w is the wavenumber in the waveguide, k_s is the wavenumber in the slab, and $\Delta\theta_j$ is the angle between the j^{th} and 1^{st} facet (θj - θ_1). Since d_j does not vary significantly along the grating and for different focal locations and is considered $d_j \approx 2R$ when outside of the phase definition. Since the facet geometry is not specified in this model, the term G, which is a constant when the grating is blazed, is considered to be unity. Distance between adjacent facets is $|m\lambda_o/n_{eff}|$, where m is the grating order, n_{eff} is the effective index of the curved guide, and λ_0 is the center wavelength. Thus, field intensity along the focal curve is:

$$\left|\Psi(x',y')\right|^2 = \frac{1}{\pi} k_s R(\Delta\theta)^2 \left|\sum_{j=1}^{N} \psi(x_j,y_j)\exp\left[-i\left(k_w 2R\Delta\theta_j + k_s d_j\right)\right]\right|^2 \qquad (2)$$

5.4 Device Simulation

5.4.1 Design parameters

The input wire waveguide length is L = 100 μm and width is a = 0.6 μm. The outer waveguide sidewall comprises the second-order blazed diffraction grating with a maximum modulation depth of 0.3 μm. This grating design yields less then 1% of the residual transmitted light in the waveguide fundamental mode at the end of the grating. The blazing orientation (see Fig. 5.1) is chosen to enhance diffraction efficiency into the -1^{st} order using the TIR effect. In order to reduce the Fresnel reflection loss and FP cavity effects, the diffracted light is coupled into the slab waveguide through a triangular SWG GRIN antireflective interface. The SWG comprises 1 μm long triangular segments with a pitch of 0.3 μm [73].

The geometry of the Rowland configuration was determined as follows. The receiver waveguide width w = 1.4 μm and the waveguide pitch at the Rowland circle of 2.4 μm were chosen to ensure compact size yet avoid mode delocalization and minimize receiver-limited crosstalk. For such a waveguide, the acceptance angle is ~0.7 rad from FDTD simulations, measured at $1/e^2$ irradiance asymptotes. For a 100 μm long curved grating, using a 0.7 rad angular width corresponds to focal length of f = 140 μm, thus the Rowland circle radius of R = 70 μm. This geometry ensures that the numerical apertures of the receiver waveguides and the grating are matched. The resulting layout size is ~ 90 μm × 140 μm.

5.4.2 Analytical results

First using Eq. 2, the focal field was calculated for the following device parameters: n_{eff} = 3.253, R = 70 μm, N = 230, λ_0 = 1540 nm, m = –1, grating length $L = |Nm\lambda_0/n_{\text{eff}}|$ ~ 100 μm, full-angle of the grating arc of 0.7 rad, and assuming the grating produces an ideal Gaussian near-field profile along the grating. The effective index of the 2D slab waveguide is used. In Chapter 6, when the device is fabricated, the effective index of a 260 nm × 600 nm Si waveguide is used. Figure 5.3 shows the demultiplexer spectra for the wavelength range of λ = 1390 nm – 1665 nm. The channel spacing is 25 nm, and calculated crosstalk is <-40 dB near the center wavelength.

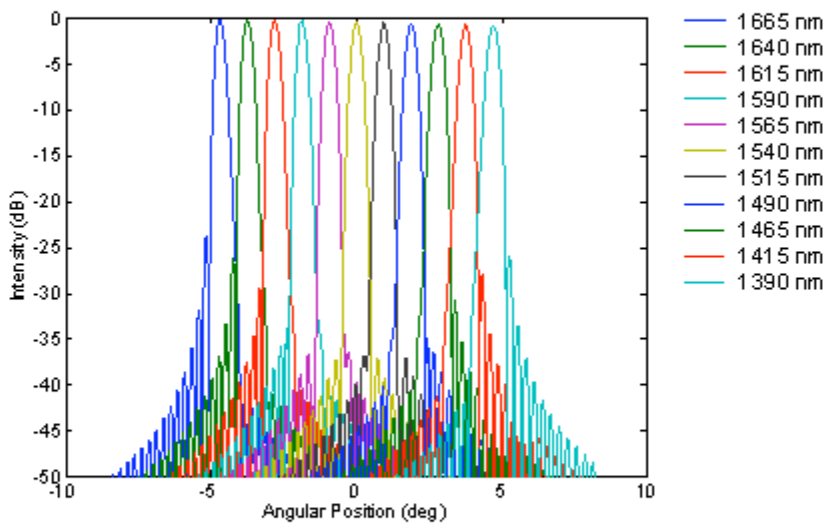

Fig. 5.3. Calculated demultiplexer spectra using a discretized Kirchhoff-Huygens diffraction integral for 11 wavelength channels from λ = 1.39 μm – 1.665 μm, with a wavelength spacing of 25 nm.

5.4.3 FDTD simulation parameters

To investigate the device further, 2D finite-difference time domain (FDTD) simulations were performed for a layout of 100 μm × 3 μm on an SOI platform with material refractive indices n_{Si} = 3.476 and n_{SiO2} = 1.444. Bulk indices are used instead of the effective index method (decomposition of the 3D structure in Chapter 6 into a 2D slab) because of the grating structure. Since the sidewall grating modulation is very deep (up to 50 % of the waveguide width, with an index contrast of $\Delta n \sim 2$), using the effective index method to decompose the 3D structure into a 2D slab would imply accounting for this variation in waveguide width (the grating teeth). This would result in an improbable volume grating representation of the waveguide sidewall grating. To use the effective index would assume separating the grating from the waveguide. The simulations were carried out for one polarization, with the electric field in the plane of the layout in Fig. 5.1. The obvious limitation of 2D simulation with respect to a real 3D device is that the vertical dimension is not accounted for; however, when the light is well confined vertically this is a reasonable approximation for the behavior of the device in the transverse plane for a proof-of-concept study. The main aspect that is gained in 3D simulations is insight into coupling efficiency to the slab region. The continuous wave (CW) Si waveguide fundamental mode was used as the input field. The mesh size used in the simulations was $\Delta x \times \Delta y = 20$ nm $\times$ 20 nm, while the time step was set according to the Courant limit of $\Delta t \leq 1/(c(1/\Delta x^2 + 1/\Delta y^2)^{½})$, where c is the speed of light in vacuum. In order to minimize the simulation layout size and render the computation more efficient, the simulation was performed for straight rather than curved waveguide geometry and the light distribution in the focal plane was calculated using the far-field integral of the field profile in the proximity of the waveguide grating, as shown in Fig. 5.4. Simulating a straight sidewall grating not only reduces the layout size, but also removes the problem of curve discretization, which at a mesh size of $\Delta x \times \Delta y = 20$ nm $\times$ 20 nm would produce simulation artifacts. The disadvantage with this approach is that in the FDTD simulations, the focusing effect of the curvature is ignored. This simplification is justified because otherwise the simulation duration would be unreasonably long.

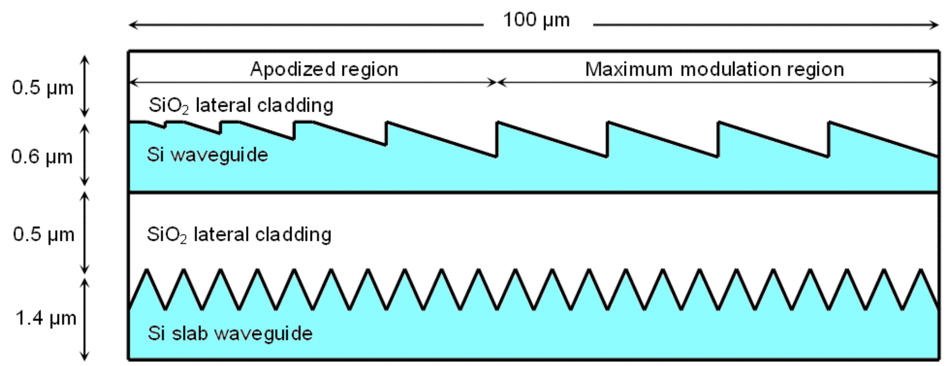

Fig. 5.4. Simulation layout of the sidewall grating demultiplexer. FDTD simulations were performed for this straight rather than curved waveguide geometry and light distribution in the focal plane was calculated using a far-field integral of the near field in the Si slab. Optimized design with apodized chirped grating is discussed in section 5.4.6.

5.4.4 Unapodized waveguide grating

Simulations were first performed on a grating with a constant modulation depth of 0.3 µm and wavelength λ = 1540 nm. Figure 5.5(a) shows the calculated phase and near-exponentially decaying field amplitude in the proximity of the grating. The calculated far-field profile is shown in Fig. 5.5(b). Four peaks are observed in the far field, at -42°, -23°, -5° and 28°, respectively. The peak with the maximum amplitude (at -5°) corresponds to the fundamental mode of the input waveguide. The satellite peaks arise from higher order excitation due to the abrupt impedance mismatch between the waveguide sections with and without the sidewall grating. In the following section it is shown that these satellite peaks can be suppressed by grating apodization.

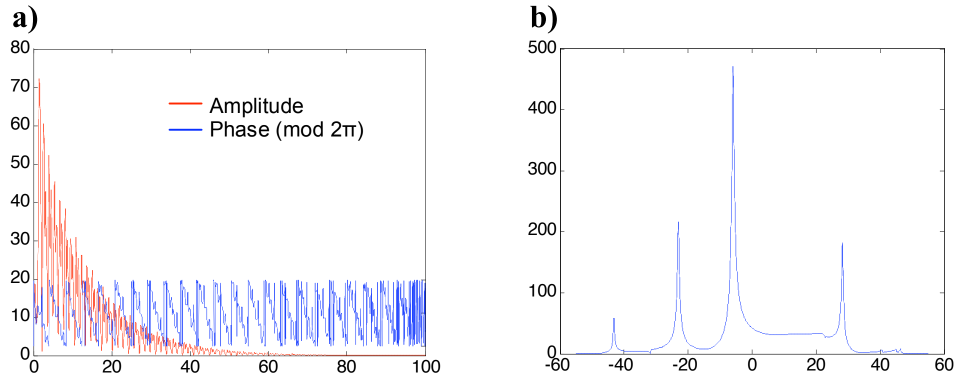

Fig. 5.5. (a) Field amplitude and phase profiles in the proximity of sidewall grating for λ = 1540 nm. The phase is shown as modulo 2π. (b) Calculated far-field profile with the principle peak at -5° and the satellite peaks at -42°, -23°, -5° and 28°.

5.4.5 Grating apodization

The grating apodization is introduced in order to assure a gradual diffraction onset and to control the near-field intensity profile. The aim is to obtain a near-field Gaussian profile, since the latter yields a far-field Gaussian distribution similar to the receiver waveguide fundamental mode. The blazed grating was apodized from an initial modulation depth of 30 nm to 300 nm maximum depth over the first 70 µm of the grating. The maximum grating depth (300 nm) was used for the remaining 30 µm of the grating length. Apodization function $y = y_0\exp(-x^2/2\sigma^2)$ was used for the first 70 µm of the grating, where y_0 is the maximum grating modulation, x is the position along the grating and σ is the variance of the Gaussian function as shown in Fig. 5.6. A variance of σ = 60 µm is used in the simulations. This apodization function shapes the exponential near-field to a Gaussian near-field; once the maximum modulation depth is reached, a constant modulation depth interacts with the diminished waveguide mode intensity to create the remaining Gaussian near-field profile.

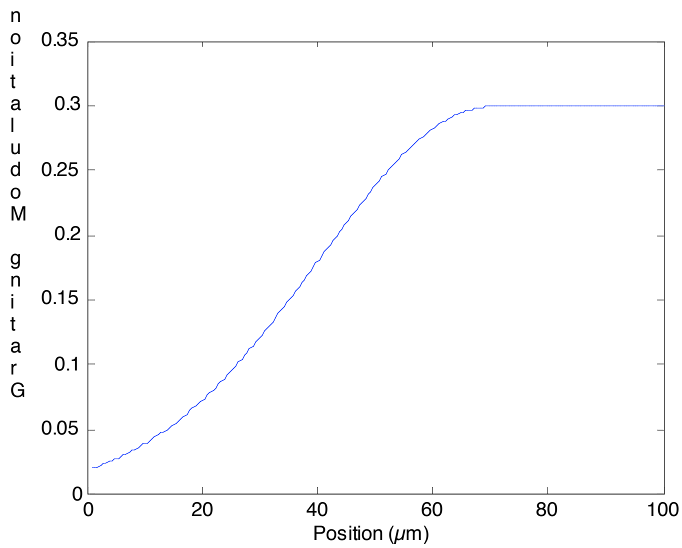

Fig. 5.6. Grating apodization profile. Gaussian apodization from a modulation depth of 0.03 μm to 0.3 μm over the first 70 μm, maximum (constant) grating modulation from 70 μm to 100 μm.

Figure 5.7(a) shows the near-field amplitude and the phase calculated for an apodized grating. It is observed that the field distribution is, to a good approximation, Gaussian. However, it is apparent that the wave vectors (k_1, k_2, and k_3) at different positions along the grating length have noticeably different directions. This varying wavevector direction results in a varying phase tilt for different positions along the grating, which causes angular broadening of the far-field profile. The latter is observed in the calculated far-field angular distribution (Fig. 5.7(b)). This phase tilt variation along the grating arises from the effective index variation caused by apodization of the grating modulation depth, since the effective index is a weighted index average that is different for each periodic grating segment.

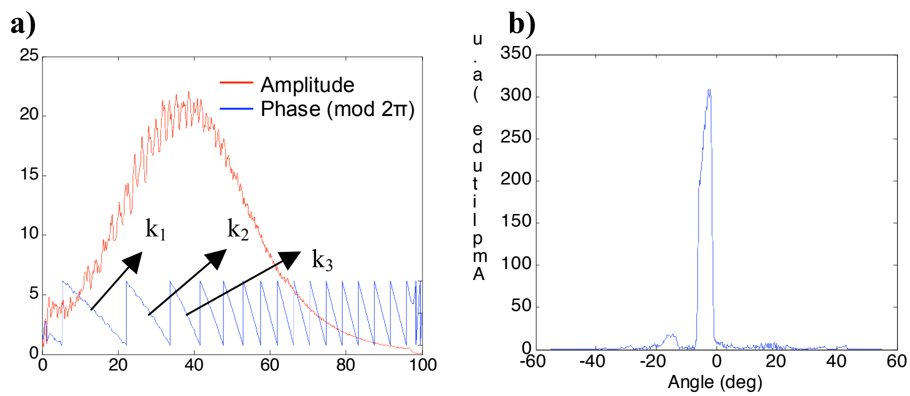

Fig. 5.7. (a) Near-Gaussian amplitude profile in the proximity of the grating for λ = 1540 nm. The corresponding phase is shown as mod 2π. The variation in the phase tilt along the waveguide and corresponding change in the direction of the wave vectors k_1, k_2, and k_3. (b) Calculated far-field profile reveals the angular broadening due to the apodization-induced effective index variation along the grating.

5.4.6 Phase correction

The angular broadening caused by phase tilt variation can be compensated by chirping the grating pitch to ensure a uniform effective index along the grating length. A similar effect may also be achieved by gradually changing the waveguide width along the grating length.

The required grating chirp is determined by calculating the grating diffraction angle for several (constant) modulation depths in the range from 50 nm to 300 nm and for several values of grating pitch in the range from 400 nm to 520 nm (Fig. 5.8(a)). The corresponding pitch and modulation is then chosen such that the diffraction angle is constant, i.e. far-field peak $\theta = 0^{\circ}$ at the centre wavelength λ = 1540 nm, along the grating with varied (apodized) modulation depth. A 2nd order polynomial fit representing this pitch-depth dependency (Fig. 5.8(b)) is used to generate a layout script for the FDTD simulation of a phase-corrected demultiplexer design.

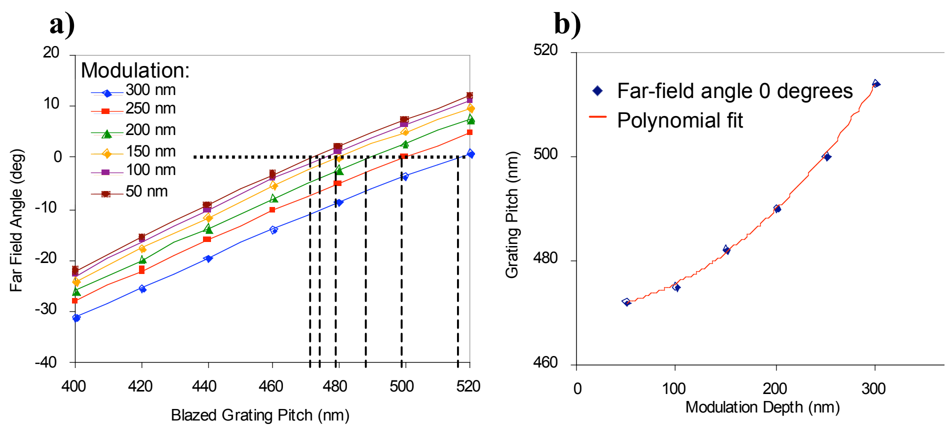

Fig. 5.8. (a) Far-field peak angles as a function of grating pitch, for various modulation depths. Dashed lines indicate the grating pitches yielding a far-field peak angle of 0° at λ = 1540 nm for different grating modulation depths. (b) 2nd order polynomial fit of pitch-depth dependency for a constant effective index (phase tilt) along the grating length, yielding far-field peak at 0°.

The pitch-depth dependency shown in Fig. 5.8 has a simple analytical expression as:

$$lan_{Si} = (l + \Delta x)an_{Si} - \frac{d^2 n_{Si}}{2} + \frac{d^2 n_{SiO2}}{2}, \tag{3}$$

which simplifies to:

$$\Delta x_g = \frac{d^2 (n_{Si} - n_{SiO2})}{2an_{Si}}. \tag{4}$$

Here Δx_g is the required change in length (for a constant refractive index along the grating), l is the segment length (local pitch), d is the modulation depth, a is the waveguide width and n_{Si}, n_{SiO2} are the refractive indices of silicon and silica. Equation 4 indicates that to ensure a constant diffraction angle, the weighted (by surface area) refractive index of a periodic grating segment must be constant. Increased modulation depth requires increased pitch to compensate for more silicon material replaced by silica. Figure 5.9 shows that 2D FDTD simulation results are in good agreement with Eq. 4.

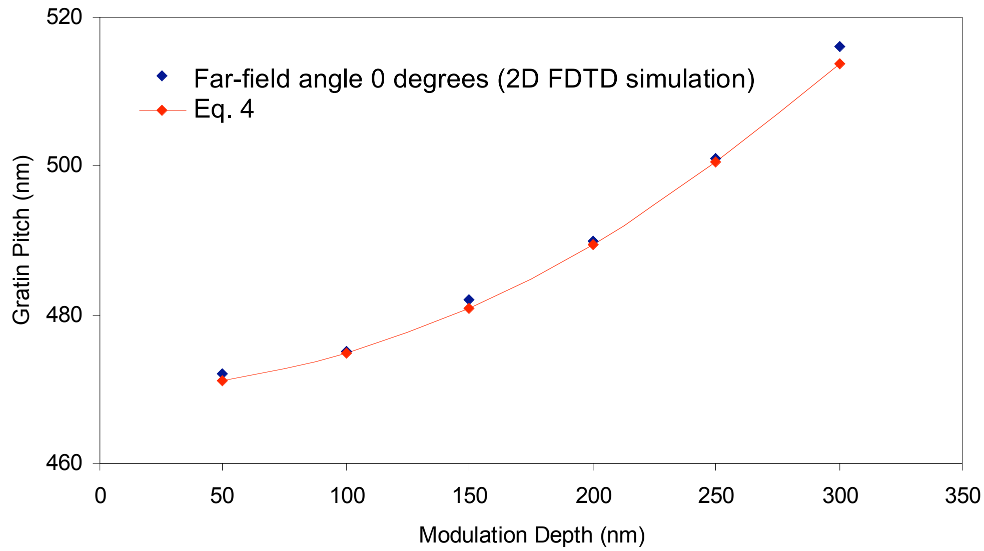

Fig. 5.9. Pitch-depth dependency calculated from 2D FDTD simulations and Eq. (4) for a constant effective index (phase tilt) along the grating length, yielding far-field peak at 0°.

Figure 5.10(a) shows the near-field at λ = 1540 nm for an apodized phase corrected grating. A substantial reduction in the phase tilt variation along the grating is observed compared to the previous design with no phase error correction (Fig. 5.7(a)). This results in a well resolved narrow far-field distribution with a full-width-at-half-maximum (FWHM) angular width of ~0.5º as shown in Fig. 5.10(b).

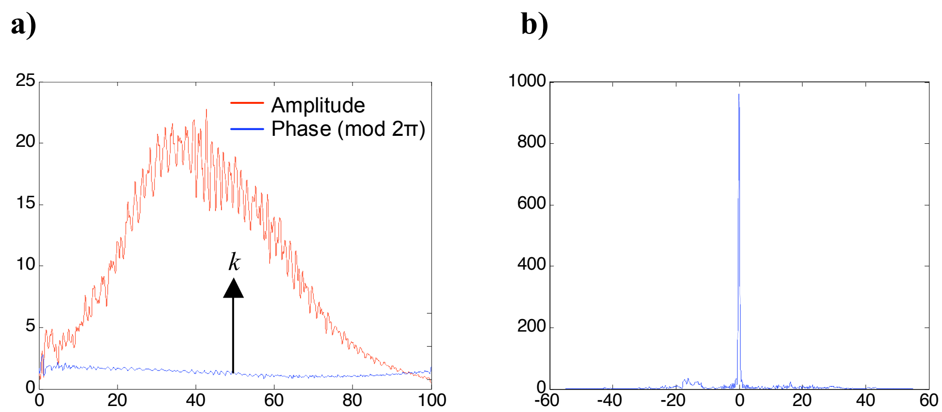

Fig. 5.10. (a) Near-field Gaussian amplitude profile for λ = 1540 nm. The phase is shown as mod 2π. Light propagating in the direction of wavevector k yielding a far-field peak at 0°. (b) Calculated far-field distribution reveals an efficient angular broadening suppression compared to the design with no phase correction (Fig 5.6(b)).

Figure 5.11 shows the calculated spectral response of a 15 channel demultiplexer in the wavelength range of λ = 1415 nm – 1765 nm, with a channel spacing of 25 nm. The passband angular width is ~0.5° at the FWHM. The calculated crosstalk is -30 dB, for a 20 nm × 20 nm simulation mesh size, but this value is still a numerical artifact of the chosen mesh size and the true theoretical limit will be smaller (<-30 dB). In fact, Eq. 2 predicts a theoretical crosstalk limit of <-40 dB near the central wavelength as shown in Fig. 5.3.

Loss associated with the focal field mismatch with the receiver waveguide fundamental mode was estimated as the overlap integral of the fundamental mode of the central receiver waveguide with the focal field for λ = 1540 nm. Loss of -1 dB was found for receiver waveguide aperture width w = 1.4 µm. This was the minimum loss for a range of widths tested and is in agreement with the initial design based on $1/e^2$ irradiance consideration (Section 5.4.1). Loss due to light diffraction into the 1st order is -1.4 dB. Thus the intrinsic device loss is -2.4 dB.

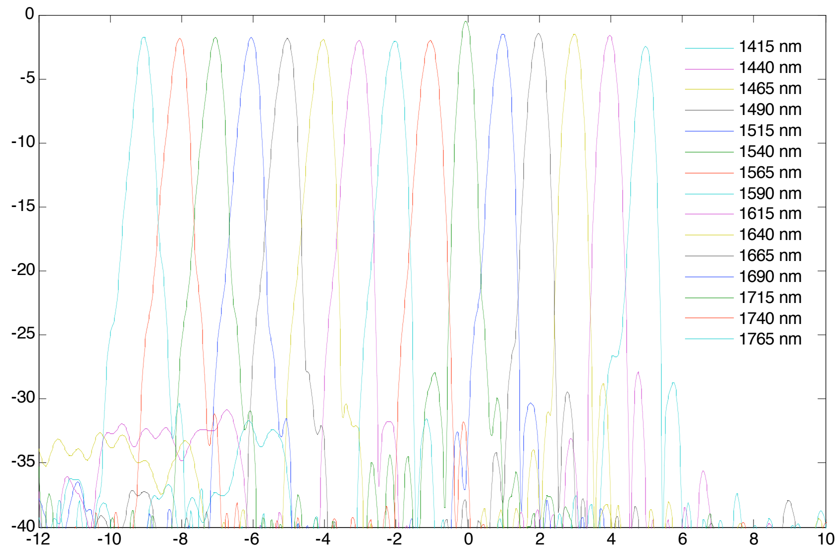

Fig. 5.11. Calculated demultiplexer spectra. 15 wavelength channels spaced at 25 nm, wavelength range λ = 1415 nm - 1765 nm.

5.5 Summary

What is achieved is an original CWDM demultiplexer design, with a compact footprint of 90 μm × 140 μm that solves **Objective 4: Demultiplexer design for high refractive index contrast waveguides**. It uses a blazed sidewall grating formed in a curved Si wire waveguide. Grating depth apodization and pitch chirping were used to obtain the optimized performance. The designed device has 15 channels with a wavelength spacing of 25 nm, thus a broadband operational bandwidth of 375 nm. This new type of waveguide demultiplexer is particularly promising for applications in optical interconnect and CWDM providing advantages such as compact size, broadband operation, and ability to tailor the passband. Since the angular dispersion depends only on the central wavelength, extension of this device to dense wavelength dispersion multiplexing is possible by up-scaling its dimensions by a factor (25 nm)/$\Delta\lambda_{DWDM}$, which is approximately 30 for 100 GHz channels. In an AWG, increasing the grating order increases the angular dispersion; however, higher grating orders are undesirable in the sidewall grating as higher diffraction orders would be excited resulting in dispersive power splitting of a wavelength channel rather than spectral filtering it. The practical implementation of the demultiplexer would not be possible without the subwavelength grating mode transformers presented in Chapter 4. The next chapter presents experimental measurements of the fabricated device.

6. Sidewall grating spectrometer fabrication

6.1 Overview

In this chapter, a sidewall grating spectrometer is experimentally demonstrated, which has been specifically designed for the silicon-on-insulator (SOI) material platform. The spectrometer's dispersive element is the sidewall grating, where the light in the input waveguide is preferentially diffracted towards the focal curve by 45º blazed grating teeth. As the light propagates along the waveguide, each tooth acts as a prism partially reflecting the light. In the previous chapter, a theoretical study modeled the grating as a 2D Kirchhoff-Huygens diffraction integral, where each prism is a wavelet source. These prisms shape the profile of the electromagnetic field near the grating, while the curvature of the waveguide focuses the field onto the focal curve. For efficient coupling to the receiver waveguide, the field profile at the focal curve must match the mode profile of the receiver waveguide. Since the mode profile of a waveguide is nearly Gaussian, a Gaussian field profile in the near-field of the grating is necessary to produce a Gaussian far-field profile at the focal curve. This is achieved by apodizing the grating teeth of the waveguide sidewall to shape an exponential diffraction profile (resulting from no apodization) into a Gaussian profile, while simultaneously minimizing Fabry-Pérot cavity effects by creating a smooth transition from waveguide to grating. The apodization function presented in the previous chapter is used. Once the maximum modulation depth is reached, a constant modulation depth interacts with the diminished waveguide mode intensity to create the remaining Gaussian near-field profile. Varying modulation depth of the grating produces a change in the effective index of each periodic grating segment, resulting in a varying phase-front tilt of the near-field, which leads to spatial broadening.

To provide a constant phase-front of the near-field from all grating modulation depths, the grating was chirped to ensure a constant effective index for the entire sidewall grating. A simple geometric relation was used to calculate the required compensatory chirp for a given modulation depth, which was confirmed by 2D FDTD simulations in the previous chapter.

This spectrometer is only possible using a subwavelength grating nanostructure between the sidewall grating and the slab waveguide. Such a nanostructure provides confinement to ensure the sidewall grating waveguide supports a mode, while simultaneously it provides a transparent waveguide boundary in the direction normal to the boundary, which results in efficient coupling to the slab waveguide. Subwavelength grating nanostructure mirrors have been applied to surface emitting lasers [86], while anti-reflective structures have been used in echelle gratings [87]. While subwavelength gratings have been used as a cladding in silicon waveguides [75], anti-reflective structures and mode converters (Chapter 4), this is the first demonstration of their twofold use as both a cladding and an anti-reflection structure. Without such a nanostructure, a shallow trench would be required between waveguide grating and slab, adding fabrication complexity.

6.2 Design parameters

The geometry of the Rowland configuration was determined from the previous chapter for the receiver waveguide width and pitch of 1.4 μm and 2.4 μm respectively. From the previous chapter, for a L = 100 μm long curved sidewall grating, 40.1° angular full width corresponds to focal length of f = 140 μm, thus the Rowland circle radius of R = 70 μm.

This geometry was slightly relaxed to R = 80, f = 160 μm to ensure that the numerical apertures of the receiver waveguides and the grating are matched. Eleven receiver waveguides were placed along the Rowland focal curve, with 20 μm long tapers to convert the 1.4 μm wide waveguide to a 0.45 μm wide single mode waveguide. These waveguides were subsequently fanned-out resulting in a 20 μm separation between adjacent waveguides.

The sidewall grating pitch is $\Lambda = |m\lambda_o/n_{eff}|$ = 0.561 μm, where m = -1 is the grating order, λ_0 = 1.54 μm is the center wavelength and n_{eff} = 2.76 is the effective index of the curved waveguide fundamental mode for TE polarization. Effective index was determined using a FDTD mode solver for a 0.6 μm × 0.26 μm silicon waveguide (n_{Si} = 3.476) on a silica substrate (n_{SiO2} = 1.444) with an SU-8 cladding ($n_{SU\text{-}8}$ = 1.58). The grating has an initial modulation depth of 0.05 μm, which increases to the maximum depth over the first 70 μm of the grating. The apodization function for the grating modulation depth is $d = d_0\exp(-x^2/2\sigma^2)$, where d_0 = 0.3 μm is the maximum modulation depth, x is the position along the grating and σ = 60 μm is the variance of the Gaussian function. Maximum grating depth (d_0 = 0.3 μm) is used for the remaining 30 μm of grating length. The grating pitch varies according to the modulation depth by $\Delta\Lambda = d^2(n_{Si} - n_{SU\text{-}8})/2an_{Si}$, where $\Delta\Lambda$ is the required change in pitch, d is the modulation depth, a = 0.6 μm is the waveguide width and n_{Si}, $n_{SU\text{-}8}$ are the refractive indices of silicon and SU-8. These parameters resulted in a curved waveguide with 183 blazed grating teeth.

6.3 Fabrication and measurement

Commercially available SOI substrates were used with 0.26 μm thick silicon and 2 μm thick buried oxide (BOX) layers. Electron beam lithography was used to define the waveguide layout in high contrast hydrogen silsesquioxane resist, which formed SiO_2 upon electron beam exposure. Inductively coupled plasma reactive ion etching (ICP-RIE) was used to transfer the waveguide layout onto the silicon layer. Samples were coated with a 2 μm thick polymer (SU-8, $n_{SU\text{-}8} \sim 1.58$ at $\lambda = 1.55$ μm), then cleaved into separate chips and facets polished. Chips were approximately 6.1 mm wide.

A polarization controller with a tunable external cavity semiconductor laser is used to measure transmission spectra ($\lambda = 1.23$ μm – 1.63 μm). To couple the light into the chip, a lensed fibre was used resulting in a Gaussian beam waist of ~2 μm and a SWG fibre-to-chip coupler [70]. Light is coupled out of the chip using another SWG coupler and subsequently focused by a microscope objective lens onto an InGaAs photodetector. To estimate the intrinsic loss of the device, spectrometers were fabricated without a waveguide sidewall grating. To measure the effect of apodization, chirp and the SWG boundary, test spectrometers were fabricated with and without those structures. Figure 6.1 shows scanning electron microscope images of the entire device (Fig. 6.1(a)), detail of the receiver waveguide array (Fig. 6.1(b)), detail of the grating with SWG interface at the opposite ends of the input waveguide (Fig. 6.1(c) and 6.1(d)) and entire waveguide grating showing the apodization of the grating teeth.

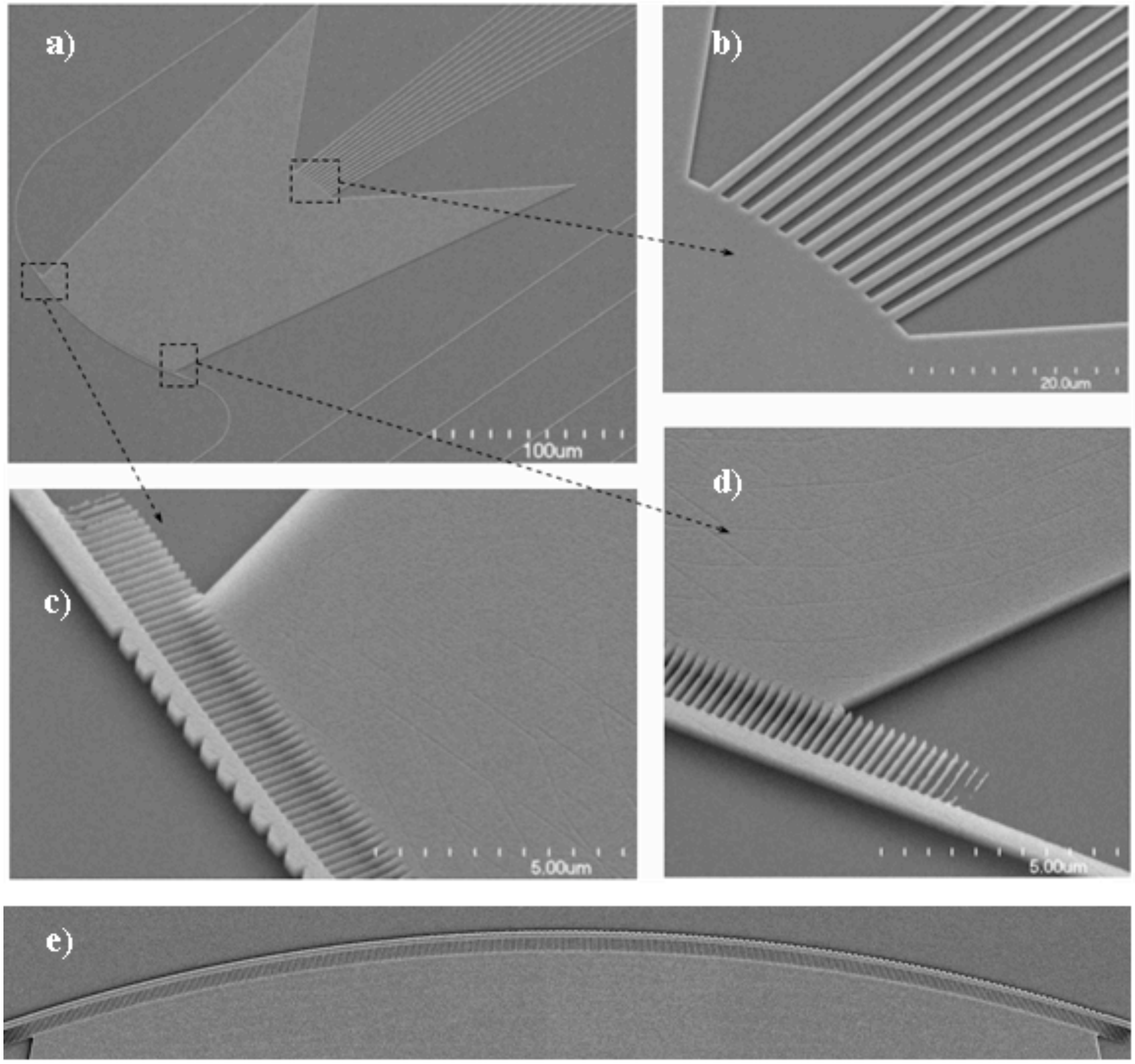

Fig. 6.1. Waveguide grating spectrometer with subwavelength grating interface. a) 3D SEM view of the spectrometer. b) Detail view of the receiver waveguides at the Rowland circle. c) and d) Detail views of the spectrometer regions with SWG interface at the opposite ends of the input waveguide. e) View of the entire sidewall grating showing the apodization of the grating teeth.

6.4 Experimental results

Four, 5 channel test spectrometers were measured including the nominal design, no apodization, no chirp and no SWG boundary. Figure 6.2(a) shows a comparison of the spectra between the nominal apodized spectrometer (grey), and a test spectrometer without apodized grating teeth (constant modulation depth of 300 nm) indicating significantly improved loss and crosstalk.

a)

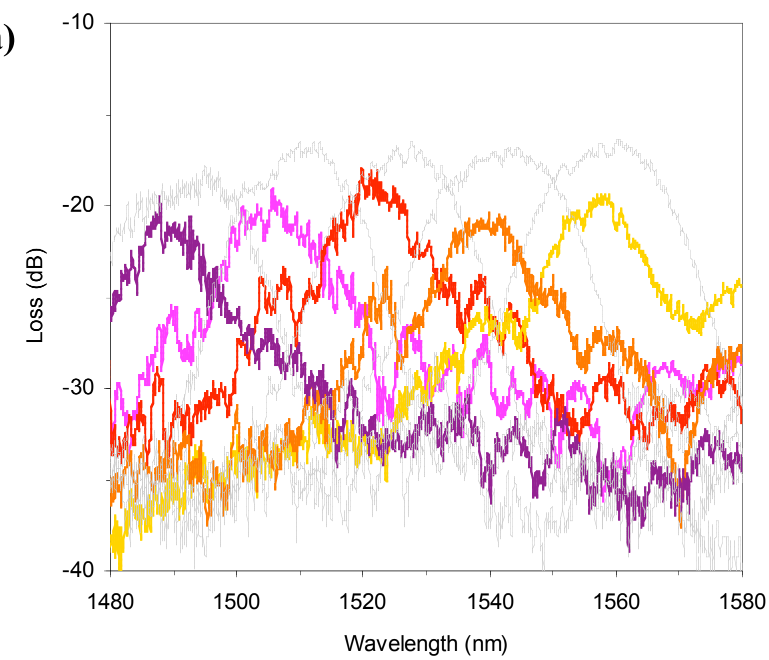

b)

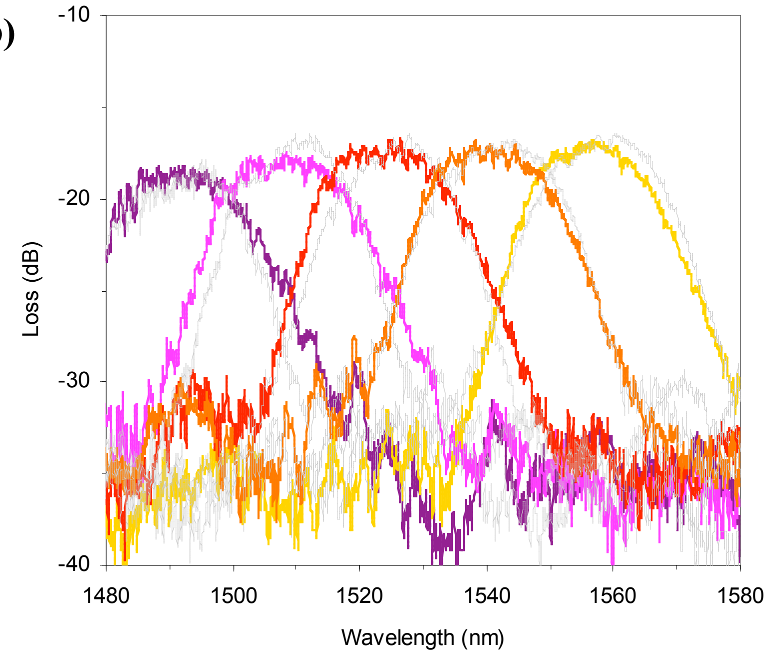

c)

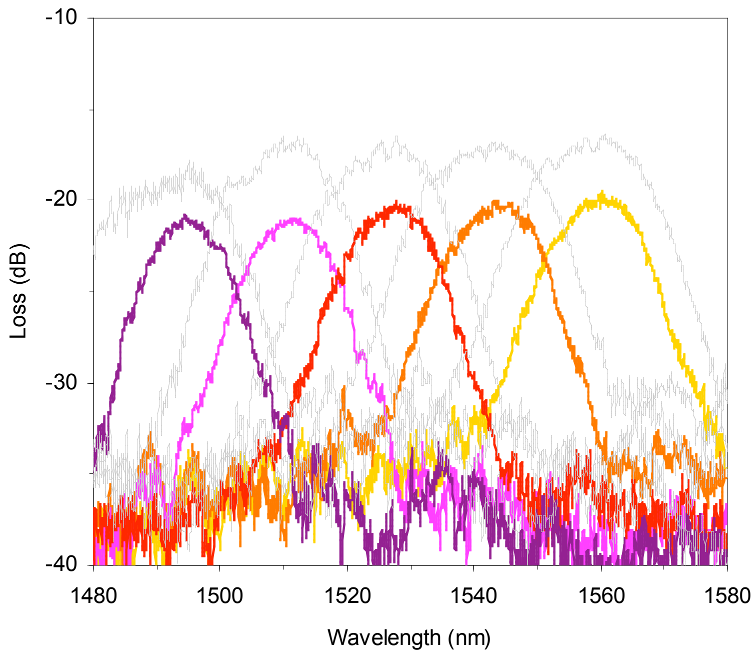

Fig. 6.2. Waveguide grating spectrometer spectra measured for five receiver waveguides spaced at 18 nm for a wavelength range λ = 1480 nm – 1580 nm, for TE polarization for the following: a) Nominal spectrometer (grey) compared to no apodization (colour). b) Nominal spectrometer (grey) compared to no chirp (colour). c) Nominal spectrometer (grey) compared to no SWG boundary (colour).

Figure 6.2(b) shows a comparison of the spectra between the nominal spectrometer, and a test spectrometer without the compensatory chirp indicating spectral broadening resulting in a top-hat response for the unchirped grating. The effect of the SWG nanostructure is shown in Figure 6.2(c) by comparing the spectral response of the nominal spectrometer to a test spectrometer with a 1 μm wide trench between the waveguide grating and the slab. By using the SWG structure there is a remarkable 4-5 dB loss reduction indicating that such a SWG structure produces efficient transitions between different waveguide geometries, even in a high refractive index contrast platform such as SOI.

Transmission spectra for a nominal eleven channel spectrometer is presented in Fig. 6.3 for TE polarization. The measured center wavelength is λ_0 = 1523 nm, which is in good agreement with the designed value (λ_0 = 1540 nm). Fabry-Pérot oscillations exist at the center wavelength pass-band and can be explained by the Bragg resonances of the sidewall grating [88]. The achieved maximum-to-minimum transmission ratio is as large as ~20 dB and the crosstalk, measured at the center of the adjacent channel, is -16 dB, which is superior to similar devices in SOI [44,45]. For this device, crosstalk can be reduced by increasing the spacing of the receiver waveguides (signal-to-noise > crosstalk), increasing the focal length or waveguide grating length (the sidewall grating is essentially a lens, where the spot resolution can be increased by increasing focal length and/or lens diameter) or adding second pass filter. Improvement in the fabrication process will also reduce crosstalk by reducing phase errors between the grating teeth.

Intrinsic loss is estimated by measuring a spectrometer without a sidewall grating, resulting in an intrinsic loss of approximately -4 dB. The 200 nm bandwidth of the device is the largest wavelength range yet reported for a miniature spectrometer chip [44,45]. It is quite remarkable that this performance is achieved for a device size of only 160 μm × 100 μm.

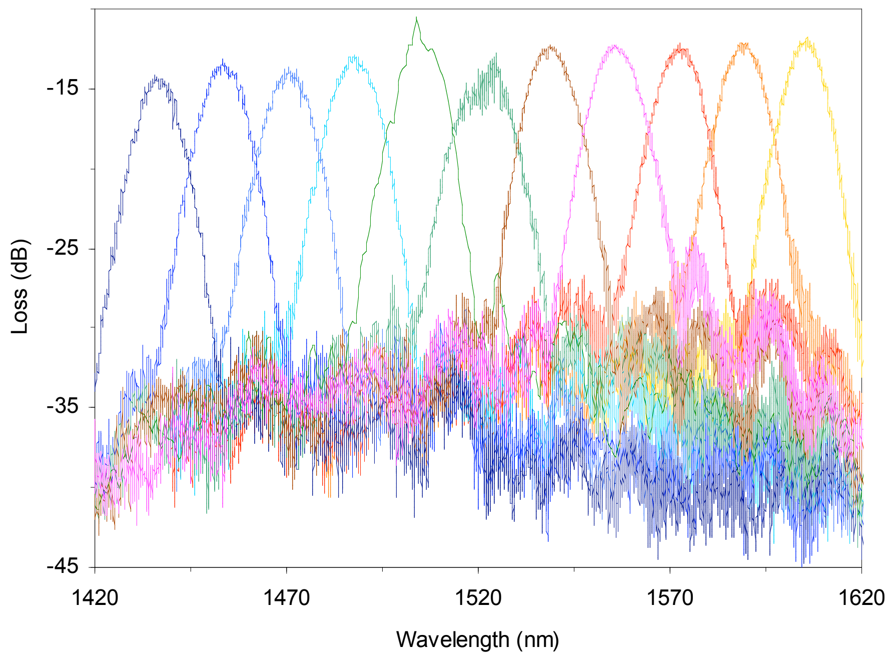

Fig. 6.3. Waveguide grating spectrometer spectra measured for eleven receiver waveguides spaced at 18 nm for a wavelength range λ = 1420 nm – 1620 nm, for TE polarization.

6.5 Summary

Achieved is the experimental demonstration of a sidewall grating spectrometer to solve **Objective 4: To create a (de)multiplexer design for high refractive index contrast waveguides**. The spectrometer has a maximum-to-minimum transmission ratio of nearly 20 dB and an operational bandwidth of 200 nm. Since it does not use a waveguide array (like an AWG), the device footprint is reduced and phase error accumulation from the waveguide sidewall imperfections is minimized. Unlike an echelle grating, the sidewall grating spectrometer has direct control of the phase and amplitude of the near-field to tailor the pass band. Also achieved is the demonstration that SWG structures can be simultaneously used as a waveguide cladding and as a transparent boundary. Without these structures, a shallow etch would be required increasing fabrication complexity.

7. Thesis Conclusion

The challenges of the high refractive index contrast SOI material platform can be addressed using subwavelength gratings. This work is relevant because of the interest in leveraging the vast silicon microelectronics fabrication infrastructure. The many advantages of SOI include, bend radii of only a few microns, high integration potential, more functions on a single chip and increased device yields. In this thesis what has been experimentally demonstrated is subwavelength grating waveguides (-2.6 dB/cm, negligible PDL), waveguide crossings (-0.023/crossing, negligible PDL) and mode converters (-0.296 dB/taper, PDL ~ -0.1 dB). Due to this low loss and minimal PDL subwavelength grating structures compare favorably to other microphotonic waveguides. Here, subwavelength gratings provide a means to implement materials with different refractive indices without changing the microelectronics fabrication process. This solution is innovative because it is based on geometric properties requiring no added fabrication complexity, process refinement or new materials. **Objectives 1, 2 and 3** are addressed in Chapters 2-4.

Presently two types of planar waveguide multiplexer technologies are used in wavelength division multiplexed networks and interconnects, namely arrayed waveguide gratings and etched (echelle) gratings. In this thesis, experimentally demonstrated is a new spectrometer/multiplexer type, never built before, that is only possible using subwavelength gratings. This solution is innovative because of the minimal device size (160×100 μm^2), low crosstalk (-20 dB) and broad operation bandwidth (200 nm). Due to this performance, the device compares favorable to conventional spectrometers. The use of apodization and chirp to control the amplitude and phase of the near-field profile allows for freedom in tailoring of the pass-band of the device. Competing technologies like echelle gratings do not have an equivalent method to tailor the field amplitude (which would require changing the reflectivity of the echelle teeth), while AWGs require either gain or attenuation in the waveguide array. This device also demonstrates that subwavelength grating can be used as an alternative to a shallow trench. **Objective 4** is addressed in Chapters 5-6. In fact, they have a two-fold use in the sidewall gratings as both an anti-reflection nanostructure normal to the waveguide grating, and a cladding material to confine the mode in the waveguide grating.

With the large interest in SOI, subwavelength grating structures can increase the material platform's flexibility by tailoring the refractive index to create an effective medium. The new spectrometer can provide a robust alternative for demultiplexing on high index contrast waveguides. The devices presented in this thesis demonstrate that subwavelength grating structure can address the challenges of the SOI material platform.

8. Future Work

A continuation of this study will involve both fundamental modeling as well as searching out applications of subwavelength gratings waveguides. A model of the effect of sidewall roughness along with the effect of delocalization based on width, periodicity and duty cycle could be investigated. From that, theoretical design rules can be developed, which could later be verified experimental by fabricating subwavelength grating waveguides with different parameters sets. Such a study could also be carried out for the subwavelength grating crossing to determine if the optimal subwavelength waveguide has the optimal crossing.

The next step for the subwavelength grating boundary transition from waveguide array to slab is to fabricate the proposed structure, along with test structures, to determine experimental what improvement subwavelength gratings offer this application. For the sidewall grating spectrometer, there are many research avenues to explore. Optimization of loss and crosstalk, application to dense demultiplexing, shaping the passband as well as adding a second pass filter are all interesting options.

From the application perspective, subwavelength grating have already been used to develop athermal waveguides [78]. The next step is to explore nonlinear applications as well as determine the information transmission characteristics of subwavelength grating waveguides including bit error rate testing. Refractive index change sensing applications could also be studied as a subwavelength grating waveguide increases the light interaction with the analyte through the periodic gaps. These gaps could then be functionalized with bio-sensitive materials to create novel sensors to recognize specific target molecules.

Appendix A: Bloch-Floquet Theory

The Bloch-Floquet theory was first proposed by Floquet in 1883 [89] and later in 1928 by Bloch [90] when he applied it to electrons placed in a periodic potential. He showed that electrons are waves in a periodic medium and propagate without scattering. Bloch's theory states that a wave traveling in a periodic structure is a plane wave, only that it is modulated by a periodic function because of the periodic lattice as indicated in Eq. A.1

$$\mathrm{H}(r) = \mathrm{e}^{\mathrm{i}\mathrm{k}r}\mathrm{u}_{\mathrm{k}}(r), \tag{A.1}$$

where $\mathrm{e}^{\mathrm{ikr}}$ is the plane wave and $\mathrm{u}_{\mathrm{k}}(r)$ is the periodic envelop. Here, the terminology from solid-state physics is that H(r) is a Bloch mode – this terminology has been adopted for the optical regime.

Applied to optical waveguides, a conventional strip or rib waveguide has continuous translational symmetry in the direction of propagation z. Here k_z, the wave vector in the direction of propagation, is continually conserved as one transitions along the waveguide's length. However, a periodic waveguide, comprised of alternating high and low refractive index segments, has discrete translational symmetry in the direction of propagation. Here, a is the lattice constant indicating the distance step where $n(\mathrm{z}) = n(\mathrm{z} + \mathrm{a})$. The subwavelength grating waveguide studied in this thesis is comprised of Si and SU-8 polymer segments. In the xy plane, the subwavelength grating waveguide confines the light by conventional index guiding as the Si segments have higher refractive index than the SiO_2 substrate or the SU-8 upper cladding. In the direction of propagation, the pitch of 300 nm is the lattice constant. Taken in isolation, it would be expected that each individual Si segment is a scattering source. As pointed out in [91], adding an infinite amount of these scattering sources, one would expect the scattering to be even stronger.

The analogy is of course with electrons (waves) propagating in a periodic potential - a lattice of atoms. Bloch's theorem states that a periodic structure need not scatter waves. The optical equivalent of an electron wave and a periodic potential is an electromagnetic wave in the optical regime and a periodic transparent material. In such a waveguide (like the one studied in this thesis), where the periodicity is the in direction of propagation z, the k_z vector is conserved. Since k_z is conserved, the light propagates without scattering and without a change in direction. The discrete transitional symmetry in z, results in a modulation of the field in z. In other words, the scattering is coherent and makes-up the periodic envelop of the Bloch mode in Eq. A.1. Provided that such a mode is below the light line, it is a guided mode and will propagate without scattering. This is non-resonant behavior, whereas wavelengths in the bandgap have no allowable Bloch mode that can propagate - the Bragg resonance in a waveguide grating. It is evident from Fig. 2.3 in Chapter 2 that the operating wavelength is far away from the band gap, where the dispersion bends and a standing wave is formed. Very recently, a closed-form expression for the scattering between adjacent subwavelength grating segments has been developed [92]. Bloch-mode orthogonality was used to derive the closed-form expression for the geometry presented in Chapter 2 and showed that the periodic mode is truly guided in the wavelength range of interest.

Appendix B: Effective medium theory

Homogenization models approximate macroscopic behavior with microscope simplification. The most well known electromagnetic homogenization model is the refractive index, which simplifies a lattice of atoms into a scalar description of a medium. Effective medium theory is a homogenization model of a composite material formed by periodically interlacing two or more different materials. It was originally proposed by Rytov in 1956 [76] and later expanded by Lalanne [77,93,98]. In terms of electromagnetic propagation, the homogenization is a power series of the ratio of effective wavelength λ_{eff} to periodicity Λ of the composite materials:

$$n_{eff} = n_0 + n_1\chi + n_2(\chi)^2 + n_3(\chi)^3 + \ \dots \quad , \tag{B.1}$$

$$\chi = \frac{\Lambda}{\lambda_{eff}} . \tag{B.2}$$

Here χ is the ratio of the two length scales, where the pitch Λ of the constituent materials is the microscopic scale and the effective wavelength λ_{eff} is the scale of the observer. There are three regimes of χ. First, the wavelength is in the order or shorter than the periodicity; this is the short wavelength limit where the laws of reflection, refraction and diffraction govern the light matter interaction. Second, the wavelength is much longer than the periodicity and as a result the light does not see the constituent materials; here diffraction is frustrated and the medium composed of periodic materials can be treated as a homogeneous medium. This is the long-wavelength limit of Eq. B.1, where $n_{\text{eff}} = n_0$. For example, the indices of the two material structure studied in this thesis (Si and SU-8) become

$$n_{\|} = [f n_{Si}^2 + (1-f) n_{SU8}^2]^{1/2} \quad , \tag{B.3}$$

$$n_{\perp} = [\frac{f}{n_{Si}^2} + \frac{(1-f)}{n_{SU8}^2}]^{-1/2} \quad , \tag{B.4}$$

where, $n_{\|}$ and $n_{\perp}$ are the refractive indices for the electric field parallel and perpendicular to the grating segments. Lastly, there exists a regime between the two extremes of the short and long wavelength limit, where the wavelength is longer than the periodicity but not long enough to be fully characterized by Eqs. B.3 and B.4. For this case, 2^{nd} and 4^{th} order closed form expressions for Eq. B.1 have been derived for one dimensional problems [77,94]. More complex problems require numerical calculation and employ the Fourier expansion method [95,96,97].

There are generally three conditions which are used to justify using the effective medium index as a substitute for a composite medium [98]. While these conditions are for a 1D structure, they provide a basis for insight into all subwavelength structures. First, only the zero order propagates through the incident (SU-8) and substrate (SiO_2) mediums. This is clearly the case in the subwavelength grating studied in this thesis as the waveguide crossings show no excitation of any higher diffraction orders. For the delocalized mode propagating through the intercepting subwavelength grating waveguide, higher diffraction orders are all evanescent. Second, only one mode propagates through the grating. This is obvious as a single effective medium index cannot represent multiple modes. The dispersion diagram Fig. 2.3 indicates that the subwavelength grating waveguide studied in this thesis only supports a single guided mode. Lastly, the depth of the grating needs to be longer than ¼ the wavelength or evanescent modes may tunnel across the grating and interfere with the fundamental mode propagation. This is ensured in the structure studied in this thesis.

Effective medium theory states that if the material periodicity is shorter than the Bragg condition, diffraction will be suppressed and the composite material can be approximated by an effective homogeneous medium with refractive index n_{eff}. Here the wavelength is outside the bandgap for the periodic structure. The light propagates through the composite medium by exciting the Bloch mode of the periodic structure as described in Appendix A. Looking at Fig. 2.3 in Chapter 2, the dispersion at the operating wavelength of 1550 nm is nearly linear. This nearly linear dispersion is far away the bandgap, and therefore is accurately modeled by the long-wavelength limit of Eqs. B.3 and B.4. If fact [99] show excellent agreement between the first order (long-wavelength) effective medium approximation and the Bloch mode solution calculated by MIT Photonic Bands Solver [82]. This justifies using effective medium theory in this thesis work as an intuitive model to design complex structures. Effective medium theory is used to describe the operation principle of devices presented in Chapters 2 to 6. Refractive index and mode size is predicted in periodic structures in Chapters 2 and 3, while the behavior of gradient refractive index structures is predicted in Chapters 4 to 6 by equations B.3. and B.4.

Appendix C: Finite-difference time-domain

Finite-difference time-domain is a modeling technique where the interaction of the electromagnetic field with a medium, at an instant in time, is numerically estimated (rather then a solution to the entire electromagnetic problem). Any input can be used; however, for simulations done in this thesis, at time t = 0 the fundamental mode of a waveguide is typically excited. The propagation of this mode is modeled by a time dependent solution to Maxwell's curl equations. In the case of 3D simulations a uniform cubic lattice, which is made up of the unit cubic Yee cell [100], is used to define the local materials. Electric field components define the edge of the Yee cell, while magnetic field components are normal to the sides of the Yee cell as shown in Fig. B.1. Time stepping is accomplished by calculating the electric and magnetic field components at half time-steps in order to estimate the field derivatives by the center difference method [101]. At a particular mesh cell, the electric field will depend on the electric field at the pervious time step and the curl of the surrounding magnetic field. The simulation duration is such that, at the mesh points of interest, the steady-state behavior of the electromagnetic field is achieved.

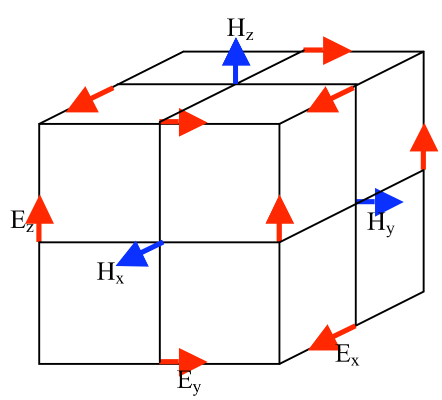

Fig. C.1. Orientation of the electric and magnetic field components on the unit Yee cell.

The motivation for implementing finite-difference time-domain models of structures presented in this thesis work is as follows. The modeling technique is elegantly intuitive, where time-domain data can provide insight into Fresnel reflections, which is particularly relevant for high-index contrast passive devices. The evaluation of the field as it approaches steady-state behavior gives insight into the modeled structure. Frequency response (assuming no nonlinear materials) can be quickly estimated by exciting a broadband pulse and normalizing the resulting output spectrum. The limitations of finite-difference time-domains arise due to the large computation domain, requiring a long simulation duration. However, structures can also be truncated such that only interesting features are present in the simulation domain as done in Chapters 2 to 4. Long simulation duration can also be mitigated by evaluating the far-field from a simulation result to effectively model larger structures as done in Chapter 5. Most simulations in this thesis were done using a mesh size of 10 nm, which is the limit of the hardware (4 duo core processors, with simulation times of 24 hours). The recommended minimum mesh size is 1/10λ (Optiwave FDTD documentation) of the shortest wavelength. Assuming 1550 nm in n_{Si} = 3.476 resulting in 44 mesh points per wavelength. Since the minimum feature size was 50 nm (for e-beam lithography), the mesh size was sufficient to sample the fine detail of the structures.

Appendix D: Huygens-Kirchhoff diffraction integral

When light passes through an aperture, it diffracts. The shape of the wavefront is governed by Huygens Principle, which states that wavelets radiate spherically outward at every point along the waterfront. The summation of all Huygens wavelets at an observation point away from the aperture is the resulting diffracted field. A scalar approximation is used to reduce the complexity of the coupled vector problem to a scalar problem, where only one field component (E_x) is used to estimate the diffracted field. Solving the scalar diffraction problem requires solving the Helmholtz equation for an aperture, which partially blocks the light. For the general 3D case the Helmholtz equation is

$$\nabla^2\psi(x,y,z) + k^2\psi(x,y,z) = 0, \tag{D.1}$$

where $k = 2\pi/\lambda$ and $\psi(x,y,z)$ is the field profile. Two possible solutions to the scalar diffraction problem are Huygens-Kirchhoff (often referred to as Fresnel-Kirchhoff) and Rayleigh-Sommerfeld. The differences between the two solutions originate from using different Green functions, resulting in different boundary conditions [102]. For both solutions the field at $z = 0$ that is transmitted through the aperture is the initial incident wave $\psi(x,y,0) = \psi_0(x,y,0)$, whereas the field being blocked is $\psi(x,y,0) = 0$. However, the Huygens-Kirchhoff solution imposes another boundary condition, namely, the derivative of the field that is transmitted through the aperture, with respect to z, is the derivative of the initial incident wave

$$\frac{\partial\psi(x,y,0)}{\partial z} = \frac{\partial\psi_0(x,y,0)}{\partial z}, \tag{D.2}$$

whereas the derivative of the field being blocked is

$$\frac{\partial \psi(x,y,0)}{\partial z} = 0. \tag{D.3}$$

The diffraction integral for the Huygens-Kirchhoff solution is

$$\Psi(x',y',z') = \iint_{x\,y} \psi_0(x,y,0) \frac{\exp(ikd)}{d\lambda} G dx dy, \tag{D.4}$$

$$G_{HK} = \frac{(\cos\alpha + \cos\gamma)}{2}. \tag{D.5}$$

The diffraction integral for the Rayleigh-Sommerfeld solution is

$$\Psi(x',y',z') = \iint_{x\,y} \psi_0(x,y,0) \frac{\exp(ikd)}{d\lambda} G dx dy, \tag{D.6}$$

$$G_{RS} = \cos\gamma, \tag{D.7}$$

where $d = [(x' - x)^2 + (y' - y)^2 + (z' - z)^2]^{1/2}$ is the distance between a point on the aperture plane and a specific point on the observation plane, λ is the wavelength, γ is the incident angle and α is the diffracted angle [102]. The difference between the two solutions is the geometry (or inclination) factors G_{HK} and G_{RS}. For many problems, including the modeling of the sidewall grating spectrometer in Chapter 5, the geometry factor is approximated as unity, which means that the Huygens-Kirchhoff and Rayleigh-Sommerfeld solutions are identical. This approximation is valid because the grating teeth for the sidewall grating spectrometer are blazed at 45º, resulting in a constant angle between the incident light and diffracted light of 90º. The Huygens-Kirchhoff solution is chosen in Chapter 5 because of the intuitively appealing model that each grating facet is a Huygens wavelet source.

The limitation of the Huygens-Kirchhoff solution is evident in problems where the observation plane is behind a light blocking region, which is not the case in Chapter 5 as the observation plane is behind the aperture and the problem is 2D. An example of a problem where the Huygens-Kirchhoff solution fails is predicting Arago's spot (or Poisson's spot). Arago's spot is the results of a summation of wavelets along the edge of a light blocking disc, which results in light intensity in the center behind the disc. For the observation plane behind the blocking disc, the Huygens-Kirchhoff solution does not converge predicting light intensity at $z = 0$ (i.e. the blocking disc becomes a source). There is no 2D equivalent of Arago's spot as a blocking line/curve would only produce two wavelet sources (at the start and end of the line/curve).

Appendix E: Mirror resonator

E.1 Introduction

Multimode interference (MMI) devices are widely used in integrated optics due to their broadband operation, polarization independent splitting ratio, and tolerance to fabrication errors. MMI couplers and splitters on the silicon-on-insulator (SOI) platform have been studied and fabricated [103,104,105]. Ring resonators have been realized in silicon waveguides [106], including racetrack designs [107], and polarization insensitive structures [108]. The use of an MMI as the coupling device in a ring resonator on SOI was reported in [109] and a polarization insensitive MMI resonator was reported in [110,111]. MMI resonators have the added advantage of not requiring extended racetrack configurations or curved input/output channels. A significant problem in high index contrast waveguides, such as silicon wires, is the impendance mismatch of the access waveguides with the MMI slab region, resulting in reflections at the end walls of the MMI. Reflection suppression for an MMI fabricated on InP/InGaAsP was reported in [112], wherein the MMI had tilted end walls, and a tapered feature at the center between the input and output channels. Mirror cavity resonators have also been fabricated with photonic crystal waveguides [113].

In this appendix an original design of a mirror cavity resonator is proposed with an MMI as the coupling element that exploits thin SOI waveguides. Presented are the equations relating loss, splitting ratio, and mirror reflectivity to the power transfer and the quality factor of the device. Since this device does not require waveguide bends, it has the added advantage of having no bending loss and a compact layout. To reduce computational load, mirrors are modeled as perfect conductors, rather than as Bragg grating which can be used in practice. Optiwave's OptiFDTD software is used to simulate the device by the finite difference time domain (FDTD) method. FDTD results are compared to analytical solutions. The FDTD simulation includes optimizing taper features for reflection suppression, namely the influence of the taper angle on the spectral response of the device. Also, the wavelength dependency of the reflection corrected MMI is compared to a conventional MMI. The resonator spectral response is studied, including the quality factor and the free spectral range.

E.2 Theoretical analysis

The two-mirror MMI resonator can be analyzed as a multiple beam interference device [114]. The following notation is used for the field amplitudes (Fig. E.1): a_1 the input field, a_2 the transmitted output field, a_3 the reflected output field and a_4 the field in the resonator cavity access waveguide. The MMI coupling coefficients are t and κ with $\gamma^2 = t^2 + \kappa^2$, mirror amplitude reflectivity is r, and the loss factor due to one round trip in the access waveguides of the cavity is α.

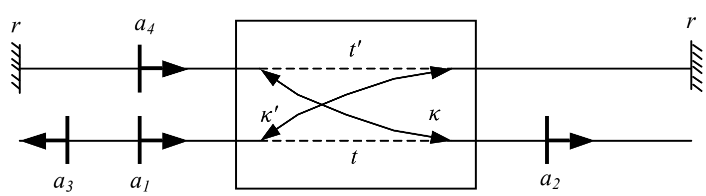

Fig. E.1. Model of the resonator: a_1 the input field, a_2 the transmitted output field, a_3 the reflected output field, a_4 the field in the resonator cavity access waveguide, t and κ the coupling coefficients, r the mirror amplitude reflectivity, γ^2 the coupler power transfer factor, and α the cavity loss factor.

The phase change of the field corresponding to one cavity round trip is φ. Then the amplitude for field a_2 is:

$$a_2 = a_1 t + a_1 \kappa' \kappa t' \alpha r^2 e^{i\phi} + a_1 \kappa' \kappa t'^3 \alpha^2 r^4 e^{i2\phi} + a_1 \kappa' \kappa t'^5 \alpha^3 r^6 e^{i3\phi} + \ldots \quad . \tag{E.1}$$

Equation (E.1) is a geometric series, which can be summed as:

$$a_2 = a_1 t + a_1 \frac{\kappa' \kappa t' \alpha r^2 e^{i\phi}}{1 - t'^2 \alpha r^2 e^{i\phi}} . \tag{E.2}$$

Similarly, the field amplitudes a_3 and a_4 can be obtained:

$$a_3 = a_1 \frac{\kappa'^2 \alpha r\, e^{i\phi/2}}{2 - 2t'^2 \alpha r^2 e^{i\phi}} , \tag{E.3}$$

$$a_4 = a_1 \frac{\alpha \kappa' t' r^2 e^{i\phi}}{1 - \alpha t'^2 r^2 e^{i\phi}} . \tag{E.4}$$

Equations (E.2)-(E.4) are analogous to equations describing a ring resonator derived in [114], with the inner circulation factor $\alpha = \alpha t'r^2$ for the two-mirror resonator. At resonance, $\varphi = 2m\pi$ (m is an integer), $a_2 \rightarrow 0$ due to the destructive interference between the transmitted field through the coupler and the cross coupled field. From Eq. (E.4) at resonance, and using the small angle approximation, the quality factor Q can be expressed as:

$$Q \approx 2m\pi \frac{\sqrt{\alpha \gamma^2 t_s^2 r^2}}{1 - \alpha \gamma^2 t_s^2 r^2} . \tag{E.5}$$

Equation (E.5) incorporates the splitting ratio t_s and the power transfer factor γ^2, where $t'^2 = \gamma^2 t_s^2$. Equations (E.2) and (E.5) are used in Section E.4.2 to verify the predictions from FDTD simulations.

E.3 Method

E.3.1 Simulation parameters

The 2D-FDTD simulation was based on a layout size of 15.7 µm × 4 µm with material refractive indices n_{Si} = 3.476 and n_{SiO2} = 1.44. Simulations were performed with the electric field in the plane of the layout shown in Fig. E.2 (TM). The input and output channels were photonic wires 0.5 µm wide. The mesh size used in the simulations was 20 nm × 20 nm, while the time step was set according to the Courant Limit. The MMI width was 3 µm, and imaging plane position was found (without tapers) through simulations at 12.7 µm from the input plane for a 50:50 splitting ratio.

E.3.2 Taper angle optimization

The input field a_1 for the MMI coupler taper angle optimization was a continuous wave (CW) fundamental mode. Simulations were executed until the input wave propagated 20 MMI lengths. The power at the output channels was calculated as an overlap integral with the fundamental mode. Wavelength dependent loss was evaluated in the wavelength range λ = 1.5 µm - 1.6 µm with a step size of 0.02 µm for both a conventional MMI and a tapered MMI. The influence of the taper angle on the device loss was evaluated for an angular range α = 30° - 80° with a step size of 5°.

E.3.3 Mirror resonator

Using the optimized MMI (lowest loss and reduced Fabry-Pérot cavity effects occur at α = 30°), a resonator device was designed with a cavity formed by two 1 µm wide mirrors terminating the upper access waveguides. Figure E.2 shows the geometry of the mirror cavity MMI-coupled resonator. A simulated femtosecond pulse with a half width of 20 fs was injected from the input channel a_1. The time domain field at the output channels a_2

and a_3 was recorded while the pulse propagated through the 20 cavity lengths (10 round trips). The spectral response of the resonator was found by the discrete Fourier transform of the time domain field. Full CW FDTD simulation was also performed for different wavelengths in the range of λ = 1.5 µm – 1.6 µm.

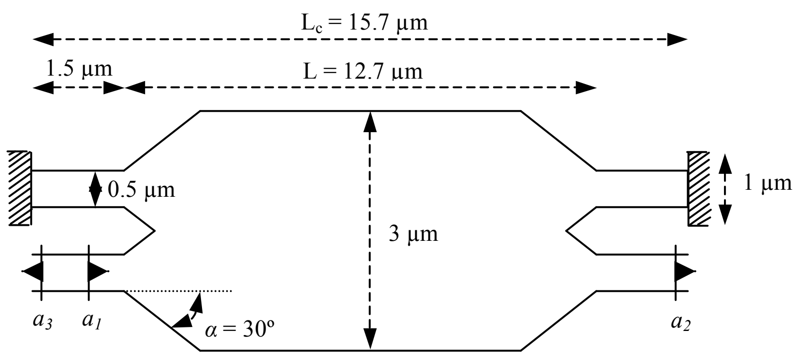

Fig. E.2. The mirror cavity MMI-coupled resonator, including MMI with reflection suppression. For the conventional MMI (no reflection suppression), the taper angle was set to α = 90°. The resonator cavity length L_c was adjusted by changing the length of the access waveguides. a_1 is the injected forward input field, a_2 is the forward output field, and a_3 is the backward output field.

E.4 Results

E.4.1 MMI reflection suppression

The MMI loss (without mirrors) is calculated as a function of the taper angle α for different wavelengths in the range of λ = 1.5 µm - 1.6 µm (Fig. E.3). It is observed that within this spectral range, for α = 30°, the MMI loss is reduced at all wavelengths, and the wavelength dependent ripple is also significantly reduced from ~1 dB down to ~0.1 dB. Due to low nearly wavelength independent loss, the optimal taper angle was set at 30° with a total MMI loss of 0.4 dB, at λ = 1.56 µm. Since the light diffracts from the photonic wire channel of a width 0.5 μm at a half angle of 21.8° (measured at $1/e^2$ far field irradiance asymptote), the taper is non-adiabatic.

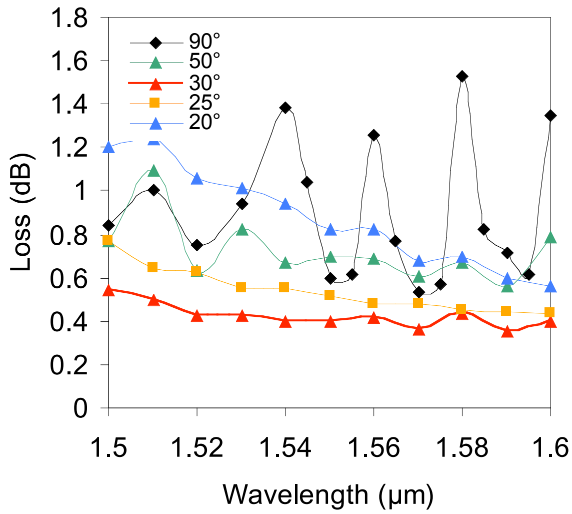

Fig. E.3. The MMI loss as a function of wavelength for different taper angles.

Figure E.4 shows the H_y field amplitude at the upper access waveguide recorded as a function of time. In the MMI without tapers (Fig. E.3, $\alpha = 90°$), the field propagates along one cavity length in 140 fs. Fluctuations in the field envelop are due to reflections at the MMI input and output boundaries. The fluctuations are separated in time by approximately 280 fs, corresponding to the arrival of the reflected field after traversing two cavity MMI lengths. For the MMI with tapers (Fig. E.3, $\alpha = 30°$), the field envelope fluctuations are substantially reduced. This type of time domain analysis is to be particularly useful to visualize and quantify the efficiency of reflection suppression when optimizing the taper angle.

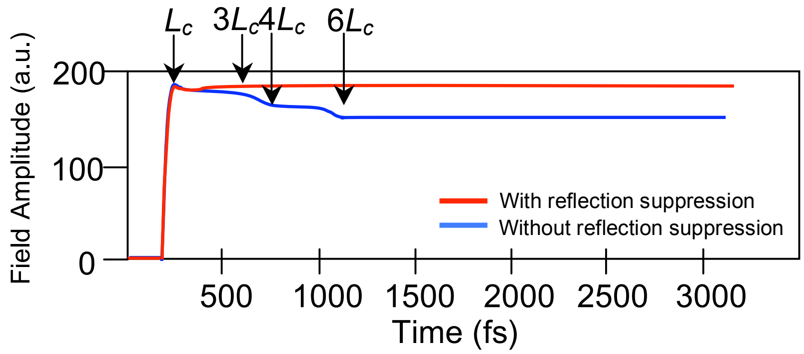

Fig. E.4. The H_y field envelop recorded at the upper output channel at $\lambda = 1.55$ µm for an MMI without tapers and with reflection suppressing tapers ($\alpha = 30°$). The arrows indicate the number of cavity lengths L_c traversed by the field.

E.4.2 Resonator simulation

The spectral response of the resonator was determined by the discrete Fourier transformation of the calculated time response (time window of 3 ps, having 1×10^6 samples). Results from the FDTD simulations were then compared to Eq. (E.2) at resonance and the quality factor was compared to Eq. (E.5). The parameters used in Eqs. (E.2)-(E.5) were obtained from the FDTD simulations: $\alpha = 1$ (lossless access waveguides), $\gamma^2 = 0.912$, and $r = 0.994$ (reflectivity of the mirror). With the cavity length of 31.4 µm, the simulated free spectral range (FSR) was 22 nm. The quality factor $Q = \lambda/\Delta\lambda_{FWHM}$ (where λ is the resonance wavelength and $\Delta\lambda_{FWHM}$ is the resonance width measured at the full-width-at-half-maximum) was calculated as 310 ($\Delta\lambda_{FWHM} = 5$ nm), whereas $Q = 300$ was predicted by Eq. (E.5). Figure E.5 shows the power in the fundamental mode in the output channels $P_2 = a_2^2$ and $P_3 = a_3^2$ as a function of wavelength.

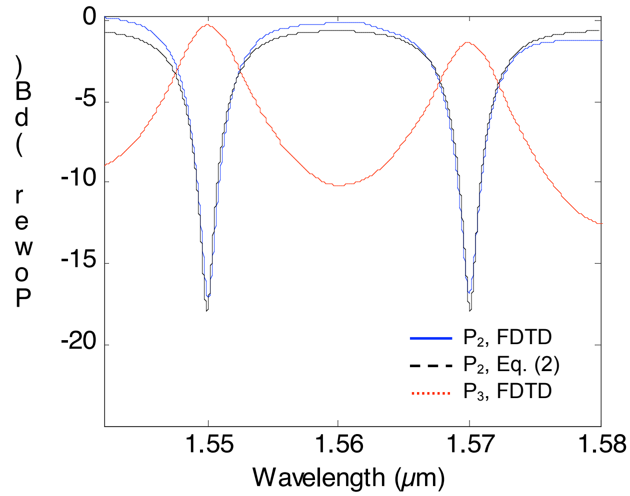

Fig. E.5. MMI resonator spectral response evaluated by FDTD simulation and Eq. (E.2) for a cavity length of 31.4 μm. FDTD simulation: FSR = 22 nm, $\Delta\lambda_{FWHM}$ = 5 nm, Q = 310. Equation (E.5) yields Q = 300.

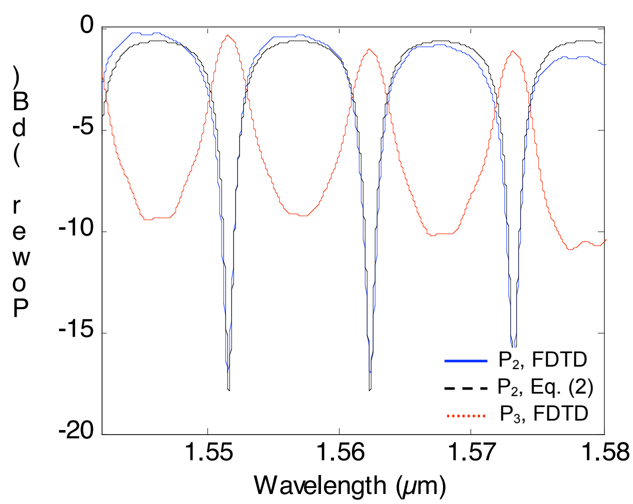

Fig. E.6. MMI resonator spectral response evaluated by FDTD simulation and Eq. (E.2) for a cavity length of 59.4 μm. FDTD simulation: FSR = 11 nm, $\Delta\lambda_{FWHM}$ = 3 nm, Q = 516. Equation (E.5) yields Q = 518.

Figure E.6 shows the spectral response of the resonator with a cavity length of 59.4 μm, which was designed by extending the access waveguides from 1.5 μm to 8.5 μm, while maintaining the same MMI width. The FSR is 11 nm and $\Delta\lambda_{FWHM}$ = 3 nm, yielding Q = 516, whereas Q = 518 was obtained from Eq. (E.5). Mirror width was also increased to 2 μm to test if 1 μm width was sufficient to fully reflect the evanescent field tail; since the 1 μm mirror reflectivity was 0.994, no significant improvement was expected. Identical values for Q were measured for both the 1 μm and 2 μm wide mirrors, indicating that 1 μm mirror width is sufficient. Bragg gratings were also simulated (2D FDTD) independently of the resonator to determine loss and spectral properties. For a 10 μm long grating on a 0.5 μm wide waveguide r > 0.96 for λ = 1.5 μm - 1.6 μm. Intuitively, a large index contrast Bragg grating will have a large spectral bandwidth.

This resonator device has similar properties to the device described in reference [115]. Since the FWHM is directly related to the resonator length [114], and the quality factor is directly related to the FWHM, the quality factor can be increased by increasing the resonator length. Also, MMI splitting ratio can be tailored by adjusting the MMI width [116], commonly referred to as MMI tapering. Splitting ratios of 85:15 have been reported in [117]. This could be used to increase the coupling coefficient to the resonator cavity, thereby decreasing the FWHM, hence further increasing the quality factor.

E.5 Conclusion

Proposed and demonstrated by FDTD simulations is a novel two-mirror resonator device with a reflection suppressed MMI coupler in the resonator cavity. An analytical model for this device is derived, which agrees with results obtained through FDTD simulation. The reflection suppression was achieved by tapering the MMI access waveguides at α = 30°. The device has a reduced loss of 0.42 dB and a negligible wavelength dependent ripple of 0.1 dB. Also, the resonator has a very small footprint of 3 μm × 30 μm, which would be difficult to achieve with a conventional racetrack design. Only straight waveguides are used in the design, which minimizes device size and eliminates the waveguide bend loss.

References

[1] F. P. Payne and J. P. R. Lacey, "A theoretical analysis of scattering loss from planar optical waveguides," Opt. and Quant. Electron. **26**, 977-986 (1994).

[2] R. Pafchek, R. Tummidi, J. Li, M. A. Webster, E. Chen and T. L. Koch, "Low-loss silicon-on-insulator shallow-ridge TE and TM waveguides formed using thermal oxidation," Appl. Opt. **48**, 958-963 (2009).

[3] F. Grillot, L. Vivien, S. Laval, D. Pascal and E. Cassan, "Size influence on the propagation loss induced by sidewall roughness in ultrasmall SOI waveguides," IEEE Photon. Technol. Lett. **16**, 1661-1663 (2004).

[4] J. H. Schmid, A. Delâge, B. Lamontagne, J. Lapointe, S. Janz, P. Cheben, A. Densmore, P. Waldron, D.-X. Xu and K.-P. Yap, "Interference effect in scattering loss of high-index-contrast planar waveguides caused by boundary reflections," Opt. Lett. **33**, 1479-1481 (2008).

[5] T. G. Nguyen, R. S. Tummidi, T. L. Koch and A. Mitchell, "Lateral leakage of TM-like mode in thin-ridge Silicon-on-Insulator bent waveguides and ring resonators," Opt. Express **18**, 7243-7252 (2010)

[6] P. Dumon, W. Bogaerts, V. Wiaux, J. Wouters, S. Beckx, J. Campenhout, D. Taillaert, B. Luyssaert, P. Bienstman, D. Thourhout and R. Baets, "Low-loss SOI photonic wires and ring resonators fabricated with deep UV lithography," IEEE Photon. Technol. Lett. **16**, 1328-1330 (2004).

[7] Y. A. Vlasov and S. J. McNab, "Losses in single-mode silicon-on-insulator strip waveguides and bends," Opt. Express **12**, 1622-1631 (2004).

[8] M. Gnan, S. Thoms, D. S. Macintyre, R. M. De La Rue and M. Sorel, "Fabrication of low-loss photonic wires in silicon-on-insulator using hydrogen silsesquioxane electron-beam resist," Electron. Lett. **44**, 115-116 (2008).

[9] F. Xia, L. Sekaric and Y. A. Vlasov, "Ultracompact optical buffers on a silicon chip," Nature Photonics **1**, 65-71 (2007).

[10] J. Cardenas, C. B. Poitras, J. T. Robinson, K. Preston, L. Chen and M. Lipson, "Low loss etchless silicon photonic waveguides," Opt. Express **17**, 4752-4757 (2009).

[11] E. Dulkeith, S. J. McNab and Y. A. Vlasov, "Mapping the optical properties of slab-type two-dimensional photonic crystal waveguides," Phys. Rev. B **72**, 1151021-1151029 (2005).

[12] L. O'Faolain, X. Yuan, D. McIntyre, S. Thoms, H. Chong, R. M. De La Rue and T.F. Krauss, “Low-loss propagation in photonic crystal waveguides,” Electron. Lett. **42**, 1454-1456 (2006).

[13] P. Cheben, “Wavelength dispersive planar waveguide devices: echelle gratings and arrayed waveguide gratings,” in *Optical waveguides: from theory to applied technologies*, M. L. Calvo and V. Lakshminarayanan, eds. (CRC Press, 2007), 173-230.

[14] C. R. Doerr and K. Okamoto, “Advances in silica planar lightwave circuits,” J. Lightwave Technol. **24**, 4763-4789 (2006).

[15] X. J. M. Leijtens, B. Kuhlow and M. K. Smit, “Arrayed waveguide gratings,” in *Wavelength filters in fiber optics*, H. Venghaus, (Springer Verlag, 2006), 125-187.

[16] A. Densmore, M. Vachon, D.-X. Xu, S. Janz, R. Ma, Y.-H. Li, G. Lopinski, A. Delâge, J. Lapointe, C. C. Luebbert, Q. Y. Liu, P. Cheben and J. H. Schmid, “Silicon photonic wire biosensor array for multiplexed real-time and label-free molecular detection,” Opt. Lett. **34**, 3598-3600 (2009).

[17] P. Cheben, J. H. Schmid, A. Delâge, A. Densmore, S. Janz, B. Lamontagne, J. Lapointe, E. Post, P. Waldron and D.-X. Xu, “A high-resolution silicon-on-insulator arrayed waveguide grating microspectrometer with sub-micrometer aperture waveguides,” Opt. Express **15**, 299-306 (2007).

[18] P. Cheben, J. H. Schmid, P. J. Bock, D.-X. Xu, S. Janz, A. Delâge, J. Lapointe, B. Lamontagne, A. Densmore and T. Hall, “Sub-wavelength nanostructures for engineering the effective index of silicon-on-insulator waveguides,” presented at the 11th International Conference on Transparent Optical Networks, Azores, Portugal, June 28 - July 2, 2009.

[19] A. Alduino and M. Paniccia, “Interconnects: wiring electronics with light,” Nature Photonics **1**, 153-155 (2007).

[20] B. Jalali, “Teaching silicon new tricks,” Nature Photonics **1**, 193-195 (2007).

[21] R. Kirchain and L. Kimerling, “A roadmap for nanophotonics,” Nature Photonics **1**, 303-305 (2007).

[22] H. Liu, H. Tam, P. K. A. Wai and E. Pun, “Low-loss waveguide crossing using a multimode interference structure,” Opt. Commun. **241**, 99-104 (2004).

[23] S. G. Johnson, C. Manolatou, S. Fan, P. R. Villeneuve, J. D. Joannopoulos and H. A. Haus, “Elimination of cross talk in waveguide intersections,” Opt. Lett. **23**, 1855-1857 (1998).

[24] Y. Jiao, S. F. Mingaleev, M. Schillinger, D. A. B. Miller, S. Fan and K. Busch, "Wannier basis design and optimization of a photonic crystal waveguide crossing," IEEE Photon. Technol. Lett. **17**, 1875-1877 (2005).

[25] Y. Watanabe, Y. Sugimoto, N. Ikeda, N. Ozaki, A. Mizutani , Y. Takata, Y. Kitagawa and K. Asakawa, "Broadband waveguide intersection with low crosstalk in two-dimensional photonic crystal circuits by using topology optimization," Opt. Express **14**, 9503-9507 (2006).

[26] W. Bogaerts, P. Dumon, D. Thourhout and R. Baets, "Low-loss, low-cross-talk crossings for silicon-on-insulator nanophotonic waveguides," Opt. Lett. **32**, 2801-2803 (2007).

[27] B. Luyssaert, P. Bienstman, P. Vandersteegen, P. Dumon and R. Baets, "Efficient nonadiabatic planar waveguide tapers," J. Lightwave Technol. **23**, 2462-2468 (2005).

[28] P. Sanchis, P. Villalba, F. Cuesta, A. Håkansson, A. Griol, J. V. Galán, A. Brimont and J. Martí, "Highly efficient crossing structure for silicon-on-insulator waveguides," Opt. Lett. **34**, 2760-2762 (2009).

[29] M. A. Popovic, E. P. Ippen and F. X. Kärtner, "Low-loss bloch waves in open structures and highly compact, efficient Si waveguide-crossing arrays," Proc. of 20th Annual Meeting of the IEEE Lasers and Electro-Optics Society, 56-57 (2007).

[30] J.-J. He, E. S. Koteles, B. Lamontagne, L. Erickson, A. Delâge and M. Davies, "Integrated polarization compensator for WDM waveguide demultiplexers," IEEE Photon. Technol. Lett. **11**, 224-226 (1999).

[31] P. Cheben, D.-X. Xu, S. Janz, A. Delâge and D. Dalacu, "Birefringence compensation in silicon-on-insulator planar waveguide demultiplexers using a buried oxide layer," Proc. SPIE **4997**, 181-189 (2003).

[32] S. Y. Chou, P. R. Krauss and P. J. Renstrom, "Imprint lithography with 25-nanometer resolution," Science **272**, 85-87 (1996).

[33] K. Maru, T. Chiba, M. Okawa, H. Ishikawa, K. Ohira, S. Sato and H. Uetsuka, "Low-loss arrayed-waveguide grating with high index regions at slab-to-array interface," Electron. Lett. **21**, 1287-1289 (2001).

[34] Y. P. Li, "Optical device having low insertion loss," Patent 5745618 (1998).

[35] F. Xia, L. Sekaric and Y. Vlasov, "Ultracompact optical buffers on a silicon chip," Nature Photonics **1**, 65-71 (2006).

[36] L. Liu, R. Kumar, K. Huybrechts, T. Spuesens, G. Roelkens, E.-J. Geluk, T. Vries, P. Regreny, D. Thourhout, R. Baets and G. Morthier, "An ultra-small, low-power, all-optical flip-flop memory on a silicon chip," Nature Photonics **4**, 182-187 (2010).

[37] J. S. Levy, A. Gondarenko, M. A. Foster, A. C. Turner-Foster, A. L. Gaeta and M. Lipson, "CMOS-compatible multiple-wavelength oscillator for on-chip optical interconnects," Nature Photonics **4**, 37-40 (2009).

[38] M. R. Pearson, P. E. Jessop, A. Bezinger, A. Delage, J. W. Fraser, S. Janz and D.-X. Xu., "Arrayed waveguide grating demultiplexers in silicon-on-insulator," Proc. SPIE **3953**, 11-18 (2000).

[39] P. Cheben, A. Delâge, L. Erickson, S. Janz and D.-X. Xu, "Polarization compensation in silicon-on-insulator arrayed waveguide grating devices," Proc. SPIE **4293**, 15-22 (2001).

[40] P. Cheben, D.-X. Xu, S. Janz and A. Delâge, "Scaling down photonic waveguide devices on the SOI platform," Proc. SPIE **5117**, 147-156 (2003).

[41] D.-X. Xu, P. Cheben, D. Dalacu, A. Delâge, S. Janz, B. Lamontagne, M.-J. Picard, and W.N. Ye, "Eliminating the birefringence in silicon-on-insulator ridge waveguides by use of cladding stress," Opt. Lett. **29**, 2384-2386 (2004).

[42] T. Fukazawa, F. Ohno and T. Baba, "Very compact arrayed-waveguide-grating demultiplexer using Si photonic wire waveguides," Jpn. J. Appl. Phy. **43**, L673-L675 (2004).

[43] K. Sasaki, F. Ohno, A. Motegi and T. Baba, "Arrayed waveguide grating of 70 × 60 μm^2 size based on Si photonic wire waveguides," Electron. Lett. **41**, 801-802 (2005).

[44] P. Dumon, W. Bogaerts, D. Van Thourhout, D. Taillaert and R. Baets, "Compact wavelength router based on a Silicon-on-insulator arrayed waveguide grating pigtailed to a fiber array," Opt. Express **14**, 664-669 (2006).

[45] X. Liu, I. Hsieh, X. C. Takekoshi, M. Dadap, J. I. Panoiu, N.C. Osgood, R. M. Green, W. M. Fengnian Xia and Y. Vlasov, "Design and fabrication of an ultra-compact silicon on insulator demultiplexer based on arrayed waveguide gratings," CLEO 2008, paper CTuNN1.

[46] S. Janz, A. Balakrishnan, S. Charbonneau, P. Cheben, M. Cloutier, A. Delâge, K. Dossou, L. Erickson, M. Gao, P. A. Krug, B. Lamontagne, M. Packirisamy, M. Pearson and D.-X. Xu, "Planar waveguide echelle gratings in silica-on-silicon," IEEE Photon. Technol. Lett. **16**, 503-505 (2004).

[47] A. Delâge and K. Dossou, "Polarisation dependent loss calculation in echelle gratings using finite element method and Rayleigh expansion," Opt. and Quant. Elect. **36**, 223–238 (2004).

[48] S. Bidnyk, D. Feng, A. Balakrishnan, M. Pearson, M. Gao, H. Liang, W. Qian, C.-C. Kung, J. Fong, J. Yin and M. Asghari, "Silicon-on-insulator-based planar circuit for passive optical network applications," IEEE Photon. Technol. Lett. **18**, 2392-2394 (2006).

[49] J. Brouckaert, W. Bogaerts, P. Dumon, D. V. Thourhout and R. Baets, "Planar concave grating demultiplexer fabricated on a nanophotonic silicon-on-insulator platform," J. Lightwave Technol. **25**, 1269-1275 (2007).

[50] F. Horst, W. M. J. Green, B. J. Offrein and Y. Vlasov, "Echelle grating WDM (de-)multiplexer in SOI technology, based on a design with two stigmatic points," Proc. of SPIE **6996**, 69960R-1-69960R-8 (2008).

[51] F. Xia, M. Rooks, L. Sekaric and Y. Vlasov, "Ultra-compact high order ring resonator filters using submicron silicon photonic wires for on- chip optical interconnects," Opt. Express **15**, 11934-11941(2007).

[52] K. Yamada, T. Shoji, T. Tsuchizawa, T. Watanabe, J. Takahashi and S. Itabashi, "Silicon-wire-based ultrasmall lattice filters with wide free spectral ranges," Opt. Lett. **28**, 1663-1664 (2003).

[53] C. K. Madsen, J. Wagener, T. A. Strasser, D. Muehlner, M. A. Milbrodt, E. J. Laskowski and J. DeMarco, "Planar waveguide optical spectrum analyzer using a UV-induced grating," IEEE J. Sel. Top. Quant. Electron. **4**, 925-929 (1998).

[54] Y. Hao, Y. Wu, J. Yang, X. Jiang and M. Wang, "Novel dispersive and focusing device configuration based on curved waveguide grating (CWG)," Opt. Express **14**, 8630-8637 (2006).

[55] I. E. Tamm and V. L. Ginzburg, "Theory of electromagnetic processes in a layered core," Izv. Akad. Nauk SSSR Ser. Fiz. **7**, 30-51 (1943).

[56] J. N. Mait and W. W. Prather, Eds., "Selected papers on subwavelength diffractive optics," SPIE Milestone Series **166,** (2001).

[57] H. Kikuta, H. Toyota and W. Yu, "Optical elements with subwavelength structured surfaces," Opt. Review **10**, 63-73 (2003).

[58] W. L. Barnes, A. Dereux and T. W. Ebbesen, "Surface plasmon subwavelength optics," Nature **242**, 824-830 (2003).

[59] J. B. Pendry, L. Martin-Moreno and F. J. Garcia-Vidal, "Mimicking surface plasmons with structured surfaces," Science **305**, 847-848 (2004).

[60] E. Ozbay, "Plasmonics: merging photonics and electronics at nanoscale dimensions," Science **311**, 189-193 (2006).

[61] S. I. Bozhevolnyi, V. S. Volkov, E. Devaux, J.-Y. Laluet and T. W. Ebbesen, "Channel plasmon subwavelength waveguide components including interferometers and ring resonators," Nature **440**, 508-511 (2006).

[62] S. Fan, J. N. Winn, A. Devenyi, J. C. Chen, R. D. Meade and J. D. Joannopoulos, "Guided and defect modes in periodic dielectric waveguides," J. Opt. Soc. Am. B **12**, 1267-1272 (1995).

[63] H. Taniyama, M. Notomi and Y. Yoshikuni, "Propagation characteristic of one-dimensional photonic crystal slab waveguides and radiation loss," PRB **71**, 1531031-1531034 (2005).

[64] A. A. Govyadinov and V. A. Podolskiy "Metamaterial photonic funnels for subdiffraction light compression and propogation," PRB **73**, 155108 (2006).

[65] Z. Weissman and A. Hardy, "2-D mode tapering via tapered channel waveguide segmentation," Electron. Lett. **28**, 1514-1516 (1992)

[66] P.-G. Luan and K.-D. Chnag, "Transmission characteristics of finite periodic dielectric waveguides," Opt. Express **14**, 3263-3272 (2006).

[67] M. M. Spühler, B. J. Offrein, G-L. Bona, R. Germann, I. Massarek and D. Erni, "A very short planar silica spot-size converter using a nonperiodic segmented waveguide," J. Lightwave Technol. **16**, 1680-1686 (1998).

[68] N. H. Chou, M.A. Arbore and M.M. Fejer, "Adiabatically tapered periodic segmentation of channel waveguides for mode-size transformation and fundamental mode excitation," Opt. Lett. **21**, 794-796 (1996).

[69] C.F.R. Mateus, M.C.Y. Huang, L. Chen, C.J. Chang-Hasnain and Y. Suzuki, "Broad-band mirror (1.12–1.62 μm) using a subwavelength grating," IEEE Photon. Technol. Lett. **16**, 1676-1678 (2004).

[70] P. Cheben, D.-X. Xu, S. Janz and A. Densmore, "Subwavelength waveguide grating for mode conversion and light coupling in integrated optics," Opt. Express **14**, 4695-4702 (2006).

[71] P. Cheben, S. Janz, D.-X. Xu, B. Lamontagne, A. Delage and S. Tanev, "A broad-band waveguide grating coupler with a sub-wavelength grating mirror," Photon. Technol. Lett. **18**, 13-15 (2006).

[72] R. Halir, P. Cheben, S. Janz, D.-X. Xu, I. Molina-Fernández and J. G. Wangüemert-Pérez, "Waveguide grating coupler with sub-wavelength microstructures," Opt. Lett. **34**, 1408-1410 (2009).

[73] J. H. Schmid, P. Cheben, S. Janz, J. Lapointe, E. Post and D.-X. Xu, "Gradient-index antireflective subwavelength structures for planar waveguide facets," Opt. Lett. **32**, 1794-1796 (2007).

[74] J. H. Schmid, P. Cheben, S. Janz, J. Lapointe, E. Post, A. Delâge, A. Densmore, B. Lamontagne, P. Waldron and D.-X. Xu, "Subwavelength grating structures in silicon-on-insulator waveguides," Advances in Optical Technologies: Special Issue on Silicon Photonics, 2008, Article ID 685489, doi:10.1155/2008/685489.

[75] M. Hochberg, T. Baehr-Jones, C. Walker and J. Witzens, "Segmented waveguides in thin silicon-on-insulator," J. Opt. Soc. Am. B **22**, 1493-1497 (2005).

[76] S. M. Rytov, "Electromagnetic properties of a finely stratified medium," Sov. Phys. JETP **2**, 466-475 (1956).

[77] P. Lalanne and J.-P. Hugonin, "High-order effective-medium theory of subwavelength gratings in classical mounting: application to volume holograms," J. Opt. Soc. Am. A. **15**, 1843-1851 (1998).

[78] J. H. Schmid, M. Ibrahim, P. Cheben, J. Lapointe, S. Janz, P. J. Bock, A. Densmore, B. Lamontagne, R. Ma, W. N. Ye and D.-X. Xu, "Temperature-independent silicon subwavelength grating waveguides," Opt. Lett. **36**, 2110-2112 (2011).

[79] H. Rowland, "Preliminary notice of results accomplished on the manufacture and theory of gratings for optical purposes," Phil. Mag. Suppl., **13,** 469-474 (1882).

[80] M. Kuznetsov and H. A. Haus, "Radiation loss in dielectric waveguide structures by the volume current method," IEEE J. Quantum Electron **19**, 1505–1514 (1983).

[81] D. Ortega, J. M. Aldariz, J. M. Arnold, J. S. Aitchison, "Analysis of quasi-modes in periodic segmented waveguides," J. Lightwave Technol. **17**, 369-375 (1999).

[82] http://ab-initio.mit.edu/wiki/index.php/MIT_Photonic_Bands.

[83] Y. A. Vlasov, M. O'Boyle, H. F. Hamann and S. J. McNab, "Active control of slow light on a chip with photonic crystal waveguides," Nature **438**, 65-69 (2005).

[84] P. Y. Yang, G. Z. Mashanovich, I. Gomez-Morilla, W. R. Headley, G. T. Reed, E. J. Teo, D. J. Blackwood, M. B. H. Breese, A. A. Bettiol, "Freestanding waveguides in silicon fabricated using proton beam writing (PBW)," App. Phy. Lett. **90**, 2411091-2411093 (2007).

[85] D. Marcuse, Light transmission optics (Van Nostrand Reinhold, 1982).

[86] M. C. Huang, Y. Zhou and C. Chang-hasnain, "A surface-emitting laser incorporating a high-index-contrast subwavelength grating," Nature Photonics **1**, 119-122 (2007).

[87] Horst, F., Green, W. M. J., Offrein B. J. & Vlasov Y., Echelle grating WDM (de-)multiplexer in SOI technology, based on a design with two stigmatic points. *Proc. of SPIE* **6996**, 69960R-1-69960R-8 (2008).

[88] G. Roelkens, "Bridging the Gap Between Nanophotonic Waveguide Circuits and Single Mode Optical Fibers Using Diffractive Grating Structures," J. Nanosci. Nanotechnol. **10**, 1551-1562(2010).

[89] G. Floquet, "Sur les équations diff´erentielles linéaires à coefficients périodiques," Ann. Ecole Norm. Sup. **12**, 47–88 (1883).

[90] F. Bloch, "Über die quantenmechanik der electronen in kristallgittern," Z. Physik **52**,
555–600 (1928).

[91] J. D. Joannopoulos, S. G. Johnson, J. N. Winn and R. D. Meade, "Photonic crystals molding the flow of light," Princeton University Press, 2008.

[92] W. Śmigaj, P. Lalanne, J. Yang, T. Paul, C. Rockstuh and F. Lederer, "Closed-form expression for the scattering coefficients at an interface between two periodic media," App. Phy. Lett. **98**, 1111071-1111073 (2011).

[93] P. Lalanne and D. Lemercier-Lalanne, "Depth dependence of the effective properties of subwavelength gratings," J. Opt. Soc. Am. A **14**, 450-458 (1997).

[94] J. M. Bell, G. H. Derrick and R. C. McPhedran, "Diffraction gratings in the quasi-static limit," Optica Acta **29**, 1475-1489 (1982).

[95] D. J. Bergman and K.-J. Dunn, "Bulk effective dielectric constant of a composite with a periodic microgeometry," Phys. Rev. **B45**, 13262-13271 (1992).

[96] S. Datta, C. T. Chan, K. M. Ho and C. M. Soukoulis, "Effective dialectic constant of periodic composite structures," Phys. Rev. B48, 14936-14943 (1993).

[97] P. Lalanne, "Effective properties and band structures of lamellar subwavelength crystals: plane-wave method revisited," Phys. Rev B58, 9801-9807 (1998).

[98] P. Lalanne and M. Hutley, "The optical properties of artificial media structured at a subwavelength scale," Encyclopedia of Optical Engineering, 2003, doi:10.1081/E-EOE-120009537.

[99] P. Cheben, P. J. Bock, J. H. Schmid, J. Lapointe, S. Janz, D.-X. Xu, A. Densmore, A. Delâge, B. Lamontagne and T. J. Hall, "Refractive index engineering with subwavelength gratings for efficient microphotonic couplers and planar waveguide multiplexers," Opt. Lett. **35**, 2526-2528 (2010).

[100] K. S. Yee, "Numerical solution of initial boundary value problems solving Maxwell's equations in isotropic media," IEEE Trans. Antenna Propagat. **14**, 302-307 (1966).

[101] A. Taflove, "Application of the finite-difference time-domain method to sinusoidal steady-state electromagnetic-penetration problems," IEEE Trans. on Electromagn. Compat. **22**, 191-202 (1980).

[102] M. Born and W. Wolf, "Principles of Optics," Cambridge University Press, 1999.

[103] P. Trinh, S. Yegnanarayanan, F. Coppinger and B. Jalali, "Compact multimode interference couplers in silicon-on-insulator technology," Proc. CLEO'97, 441 (1997).

[104] T. Zinke, U. Fischer, B. Schuppert and K. Petermann, "Theoretical and experimental investigation of optical couplers in SOI," Proc. SPIE **3007**, 30-39 (1997).

[105] Y. Tang, W. Wang, Y. Wu, J. Yang and Y. Wang, "Design and fabrication of multimode interference coupler with strong confinement structure on silicon-on-insulator," Opt. Eng. **43**, 2495-2496 (2004).

[106] B. E. Little, J. S. Foresi, G. Steinmeyer, E. R. Theon, S. T. Chu, H. A. Haus, E. P. Ippen, L. C. Kimerling and W. Greene, "Ultra-compact Si-SiO ring resonator optical channel dropping filters," IEEE Photon. Technol. Lett. **10**, 549-551 (1998).

[107] I. Kiyat, A. Aydinli and N. Dagli, "High-Q silicon-on-insulator optical rib waveguide racetrack resonators," Opt. Express **13**, 1900-1905 (2005).

[108] W. R. Headley, G. T. Reed, S. Howe, A. Liu and M. Paniccia, "Polarization independent optical racetrack resonators using rib waveguides on silicon-on-insulator," Appl. Phys. Lett. **85**, 5523-5526 (2004).

[109] D.-X. Xu, A. Densmore, P. Waldron, J. Lapointe, E. Post, A. Delâge, S. Janz, P. Cheben, J.H. Schmid and B. Lamontagne, "High bandwidth SOI photonic wire ring resonators using MMI couplers," Opt. Express **15**, 3149-3155 (2007).

[110] D.-X. Xu, S. Janz and P. Cheben, "Design of polarization-insensitive ring resonators in SOI using cladding stress engineering and MMI Couplers," IEEE Photon. Technol. Lett. **18**, 343-345 (2006).

[111] D.-X, Xu, P. Cheben, A. Delâge, S. Janz, B. Lamontagne, E. Post and W. N. Ye, "Polarization insensitive MMI-coupled ring resonators in silicon-on-insulator using cladding stress engineering," Proc. SPIE **6477**, 6477D1-6477D10 (2007).

[112] R. Hanfoug, L.M. Augustin, Y. Barbarin, J.J.G.M. van der Tol, E.A.J.M. Bente, F. Karouta, D. Rogers, S. Cole, Y.S. Oei, X.J.M. Leijtens and M.K. Smit, "Reduced reflections from multimode interference couplers," Electron. Lett. **42**, 13-15 (2006).

[113] P. E. Barclay, K. Srinivasan and O. Painter, "Nonlinear response of silicon photonic crystal microresonators excited via an integrated waveguide and fiber taper," Opt. Express **13**, 108-120 (2005).

[114] A. Yariv, "Universal relations for coupling of optical power between microresonators and dielectric waveguides," Electron. Lett. **36**, 321-322 (2000).

[115] S. Kim, J. Cai, J. Jiang and G. P. Nordin, "New ring resonator configuration using hybrid photonic crystal and conventional waveguide structures," Opt. Express **12**, 2356-2364 (2004).

[116] L.B. Soldano and E.C.M. Pennings, "Optical multi-mode interference devices based on self-imaging: principles and applications," J. Lightwave Technol. **13**, 615-627 (1995).

[117] M.-K. Chin, C.-L. Xu and W.-P. Huang, "Theoretical approach to a polarization-insensitive single-mode microring resonator," Opt. Express **12**, 3245-3250 (2004).